國立臺灣大學電機工程所
博士論文
Department of Electrical Engineering
College of Electrical Engineering and Computer Science
National Taiwan University
Doctoral dissertation

以逆向式光聲影像進行光吸收係數重建及血流量測

Optical absorption reconstruction and blood flow measurements using backward mode photoacoustic imaging

廖超康
Chao-Kang Liao

指導教授：李百祺 教授
Pai-Chi Li（Ph.D）

中華民國 九十六 年 七 月
July 2007

國立台灣大學電機工程學研究所

博士學位論文

以逆向式光聲影像進行光吸收係數重建及血流量測

研究生 ： 廖超康

指導教授 ： 李百祺 教授

經考試合格特此證明

博士學位論文考試委員 ：

指導教授 ：

研究所所長 ：

中華民國九十六年七月

Optical absorption reconstruction and blood flow measurements using backward mode photoacoustic imaging

By

Chao-Kang Liao

Dissertation

Submitted in Partial Fulfillment of the Requirement for the Degree of Doctor of Philosophy in Department of Electronic Engineering National Taiwan University, Taipei, Taiwan

July 2007

Approved by :

Advised by :

Approved by Chairman :

致謝

我要特別感謝指導教授李百祺老師，他讓我知道越有能力的人背負著越大的責任且越需要以身作則。老師教導我的不僅是學術成就，更是自我觀察的能力，以及讓我學習到如何面對人生挑戰的方法。

博士班研究的路是不好走的，同學們彼此的扶持與輔助就顯得格外重要。這裡我要感謝振瑋，我的老戰友，能夠無怨無悔的協助光聲的成長，他讓我知道待人處事的態度是如此重要，也了解惟有保持謙遜的心才能被給予的最多。葉秩光、李夢麟、沈哲州、葉文俊、黃聖文、鄭耿璽、吳東格、劉時泰學長們的指導與提攜讓我能在減少錯誤重複的情況下順利取得學位。另外也要特別感謝張儀中學長，他所教授的硬體知識以及實務經驗遠大於我先前所學，使我能真正成為電機人，能與他共事是來台大最幸運的事情之一。感謝建宏、愛禾、維寧、寬裕、承翰、俊延、珣力、珵涵、慈吟、智威、立言、雲謙、曄琳、勝勇、依明、欣嘉、文道、雅健、博文、健銘、昱欣、嘉翎、士育等學弟妹們，不管實質上的幫助或是共患難的精神都是在我研究歷程中不可抹滅的。

最重要的，我要特別感謝我的父母與姐姐，我所有成就都歸功於家人默默的幫助，讓我能夠揮霍他們無限的支持與關懷戴上台灣最高學府的光環並且眺望世界。陪了我七年研究生涯的沁樺，也是我最大的支柱，總能陪我度過研究低潮以及困難，我對她並不是感謝二字可以詮釋的。

五年的研究時期，我經歷了實驗室多個轉折，我以能參與其中並且與之成長而感到欣慰。這期間內我所得到來自師長、學長姐、學弟妹以及家人的幫助不是一張致謝所能表達的，在這裡我給予我最誠摯的感謝及祝福，帶著自信且不畏艱難的心往下個人生的旅程邁進。

中文摘要

光聲影像的構成結合了雷射能量的發射以及超音波的接收，因此光聲可以在優於其他純光學系統的探測深度條件下提供光學參數(即光吸收係數)。目前研究中的光聲成像依照掃描架構的不同分成三個形式，包含斷層模式、逆向模式以及正向模式。其中，逆向式光聲成像法是將超音波探頭與雷射照射配置於同側來進行光聲訊號的偵測。在這樣的架構下，逆向式光聲成像相較於其他形式的成像方式具有更簡單的機構配置以及更彈性的掃描範圍。不過，在現有的逆向式光聲成像方法中，只能侷限於觀測光吸收係數的梯度分佈的重建。光吸收物體內的吸收係數分佈卻無法真實的呈現。在這篇論文中，我們提出三個連續的重建演算法來取得光吸收係數的分佈，其中包含聚焦的可適性權重法、光能量吸收分佈重建法以及遞迴式吸收係數重建法。首先，由於光聲無方向性傳遞的特性以及探頭較大的偵測區間會造成影像的橫向解析度較差，而聚焦的可適性權重法則是用來提升橫向的影像解析度。較好聚焦品質的影像可以讓我們進一步藉由光能量吸收分佈重建法得到物體所吸收的光能量分佈。此重建法是以光聲的線性波動方程式中推導所得。最後，我們使用遞迴式吸收係數重建法，使用上個步驟所得到的光吸收能量分佈進而計算出光吸收係數的分佈。研究中，我們以模擬以及實驗的方式驗證這些演算法在逆向式光聲影像的重建效果。實驗結果證實了此重建方法的可行性以及影像的改善程度。組織內的光學參數(包含光吸收係數及光能量累積分佈)都可以經由我們提出的方法測量出。模擬結果與理論值影像的相似度經過計算後有相當大的一致性。除了結構性影像的重建，我們另外驗證了以高速光聲影像配合金奈米桿進行流速測量的可能性。研究中，我們使用單能量與雙能量灌入流速測量法進行測量。由於灌入流速測量法需要連續並且快速的追蹤光聲訊號，因此我們建立一套高速的光聲成像系統。此系統包含 Nd:YAG 雷射、自製光聲線形陣列探頭、及超音波前端擷取系統。超音波擷取系統具有同時接收 64 通道光聲訊號的能力，使得高速光聲成像系統的幀數僅侷限於現有之雷射系統的脈衝產生率。實驗使用雞胸組織作為仿體，並且以人體血液加入金奈米粒子作為流體溶液。實驗所擷取的影像可以同時呈現逆向式的光聲影像以及提供流體的流速資訊，所計算出的流速與理論值有極佳的線性相關度。

關鍵字: 光聲影像、逆向式、光吸收能量分佈、光吸收係數、金奈米粒子、非侵入式、流速估算

Abstract

Photoacoustic imaging combines laser irradiation and ultrasound detection and offers the advantage of visualizing optical properties (e.g., the optical absorption) with a better penetration depth as compared with all-optical imaging techniques. Three major scanning modes, including the tomographic, the backward, and the forward modes, have been used. In the backward mode, photoacoustic signals are measured by using an ultrasound transducer placed at the same side as the laser irradiation. Such a setup makes the backward mode more flexible and easier to be integrated. However, performance of image reconstruction in backward mode has suffered from the small angular extent during the data acquisition. In most situations, only gradients of the optical absorption can be visualized. In this thesis, sequential steps of a new reconstruction algorithm including the adaptive weighting method, reconstruction of energy deposition (RED), and the iterative recovery of absorption (IRA) are introduced for reconstruction of the absorption coefficient. First of all, the adaptive weighting was utilized to improve the lateral resolution that was degraded due to the nondirective photoacoustic wave and the broad radiation pattern of photoacoustic detector. Secondly, the RED was used to obtain the deposited energy based on the photoacoustic wave equation. Finally, the resultant energy deposition was used to reconstruct the absorption coefficient by applying the IRA. Simulations and experiments were performed to evaluate the efficacy of the proposed reconstruction algorithm. Optical parameters, including the deposited energy and the absorption coefficient, were accurately obtained. The results also agree well to the theory.

In addition to the reconstruction algorithm, we also performed flow estimation by using a high-speed backward mode photoacoustic imaging system with gold nanorods as the contrast agent. Two wash-in flow estimation methods were developed by measuring intensities from a sequence of photoacoustic images. A system consisted of a Q-switch Nd:YAG laser, a photoacoustic transducer array, and an ultrasound front-end subsystem that allows photoacoustic signals to be acquired simultaneously from 64 transducer elements. Currently, the frame rate of this system is only limited by the pulse repetition rate of the laser. Experimental results from a chicken breast tissue show that both the structural image and the flow velocities can be measured simultaneously. The measured flow rates are in linear proportion to the theoretical values.

Keywords: Photoacoustic imaging, backward mode, optical energy deposition, optical absorption coefficient, gold nanorods, noninvasive, flow estimation

Glossary of symbols

$\mu_a(r)$	optical absorption coefficient
$\mu_s(r)$	optical scattering coefficient
$g(r)$	optical anisotropy factor
Φ	laser fluence
D	optical diffusion coefficient
μ'_s	transport scattering coefficient
ρ	density
C_p	specific heat
E	deposited energy
τ_l	laser pulse duration
τ_{th}	heat diffusion time
z_{eff}	optical penetration depth
μ_{eff}	effective optical attenuation coefficient
κ	thermal diffusivity
φ	scalar potential of velocity field
β	thermal expansibility
p	pressure wave
τ_{st}	time of ultrasound propagated out from the heated region
$s(i,t)$	received photoacoustic signal at the i-th position, τ_i is the time delay
M	total number of adjacent scan lines in SAFT
s_{weighted}	CF-weighted signal
s_{focused}	SAFT signal
CF_{noise}	noise-disturbed CF value,
n	thermal-noise
η	temporal profile of laser irradiation
ξ	position on the boundary
Ω	simulated domain
SAD	sum of absolute difference
SRD	sum of relative difference
IC	image correlation
CNR	contrast-to-noise ratio
$err^{(n)}$	iteration error
$n(y;t)$	concentration of gold nanorods

PRI	pulse repetition interval
$\delta(y)$	Dirac delta function
λ	model parameter
I	photoacoustic intensity
RED	reconstruction energy deposition
SAFT	synthetic aperture focusing technique
CF	coherence factor
$\mathrm{CF}_{\mathrm{noise}}$	noise-disturbed CF
CF_{d}	CF value from differentiated pressure wave
CFW	coherence factor weighting
LIOB	Laser induced optical breakdown
IRA	iterative recovery of absorption coefficient
SNR	signal-to-noise ratio
E_{s}	signal energy
E_{n}	noise energy
$\mathrm{p(t)}\vert_{\mathrm{x}}$	focused pressure wave
$\mathrm{E(z)}\vert_{\mathrm{x}}$	energy deposition along *z*-axis
$\hat{p}(t)\vert_{\mathrm{x}}$	integrated pressure wave
$deconv\{\}$	deconvolution
D	diffusion coefficient
$u(y)$	beam profile of the ultrasound transducer (*y*-axis)
TIC	time intensity curve
ITIC	integrated time intensity curve
STD	standard deviation

Table of Contents

List of Figures

List of Tables

Chapter 1 Introduction

Photoacoustic effect was discovered by Alexander Graham Bell in 1880 [1]. He proposed a “photophone” which transmits the sound by a beam of sunlight that was rapidly interrupted by the emitted sound, as shown in Fig. 1.1. In 1963, pioneer studies of using laser beam as a source for photoacoustic generation were proposed by White [2, 3]. Because the laser is a high power and monochromatic light, measuring the absorption spectrum by using photoacoustic technique has became more accurate. In 1993, the spectral characteristics and mathematical expressions of laser induced photoacoustic generation in both liquid and solid were summarized and detailed by Gusev and Karabutov [4]. Based on their explicit description, the photoacoustic phenomena and the interaction between the laser energy and acoustic generation can be easily discussed with mathematical models. To date, this technique has been widely used in measuring the gas spectrum (photoacoustic spectroscopy [5, 6]), the temperature (photoacoustic thermometer [7-9]), the speed of sound [10, 11], and the defect of semiconductors [12, 13] and biomedical tissues [14-16](photoacoustic imaging).

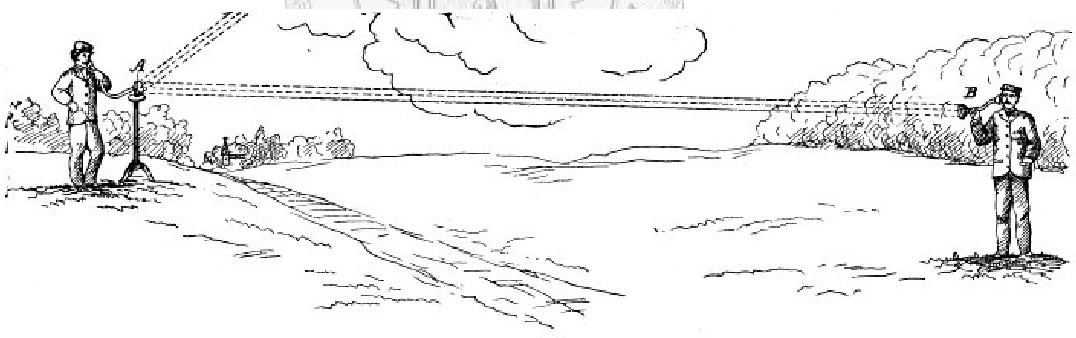

Fig. 1.1 The photophone (proposed by Bell in 1881 [1]). The emitted sound rapidly interrupts the reflecting sunlight at point A and the modulated sunlight then induces photoacoustic waves at point B. The generated photoacoustic waves can be heard at point B and the transmission of voice may be achieved.

In biomedical applications, photoacoustic imaging offers advantages of both a higher optical contrast than conventional ultrasound imaging and a better penetration depth as compared with all-optical imaging techniques, such as microabsorption spectrometry and dark-field microscopy. Generally, when a tissue is irradiated by an incident laser pulse, absorption of the laser energy leads to a rapid temperature rise, thermal expansion, and the concomitant generation of broadband ultrasound waves [4]. These waves can be used to estimate optical properties (e.g., the optical absorption) of the tissue (assuming temporal stress confinement) [17, 18]. These measured optical properties, such as absorption and scattering, can be used to characterize biological tissues [19, 20].

In recent years, the capability of photoacoustic imaging has been demonstrated in the literature, including functional imaging of rat brain [15], breast tumor detection [21], and molecular imaging [22]. Since the photoacoustic detection is achieved by both the laser irradiation and the ultrasound detection, most of applications exhibit the ability of photoacoustics to image with an excellent penetration depth as compared with all-optical techniques. Therefore, photoacoustic imaging is a more effective way to identify various problems that are optical sensitive and may have been overlooked in other optical tests. Table 1.1 lists the comparison among the photoacoustics, the conventional ultrasound, and the optical coherent tomography [23].

Table 1.1: A comparison among various imaging modalities including the ultrasound, the optical coherent tomography, and the photoacoustics [23].

Properties	**Ultrasound**	**OCT**	**Photoacoustics**
Optical contrast	Poor	Excellent	Excellent
Resolution	Good	Excellent (~10μm)	Good (=US)
Imaging depth	~3 cm	<1 mm	Excellent (=US)
Speckle artifacts	Strong	Strong	None

1.1 Photoacoustic generation

There are mainly two phenomena involving the process of photoacoustic generation. They are the optical-thermal and the thermoelastic responses. The former phenomenon describes the transformation of incident laser energy to heat [24], and the latter characterizes the energy conversion to elastic pressure wave from the heat [4, 18, 19]. Fig. 1.2 presents the block diagram of the photoacoustic generation [24]. All these effects start with the incident laser irradiation, which strikes the surface of tissue and penetrates with a depth depending on the laser energy. The incident light energy propagates based on the optical properties of tissue, including the scattering coefficient $\mu_s(r)$, the anisotropy factor $g(r)$, and the absorption coefficient $\mu_a(r)$ [24]. After the laser propagation, the laser energy (i.e., the fluence) is absorbed inside the tissue with the corresponding absorption coefficient and then results in rapid temperature rise. The induced heat directly converts to an initial pressure simultaneously with the heat diffusion based on the heat conductivity of the tissue [19]. Finally, the initial pressure propagates outward with a broad bandwidth based on the wave equation. These pressure waves propagate through the tissue and can be detected by using ultrasound transducer. In the following sections, the entire generation processes of photoacoustic signals are introduced respectively into two steps including the light transport model and the generation and the propagation of the photoacoustic waves.

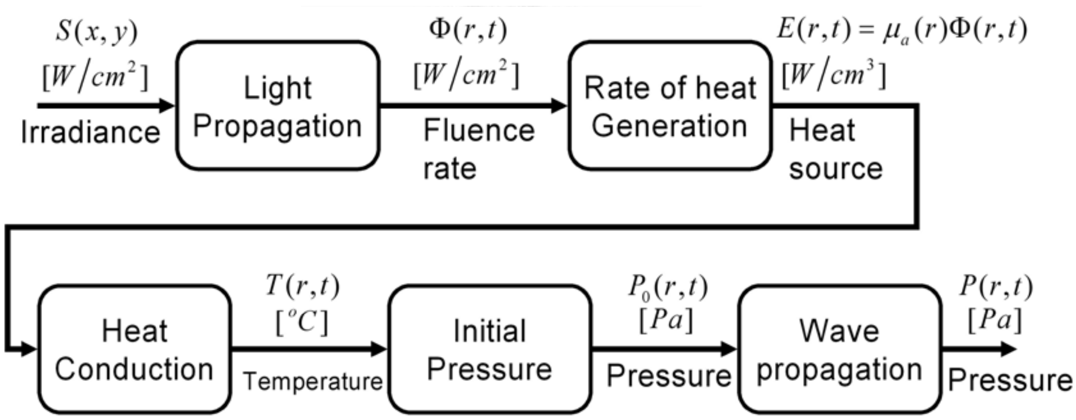

Fig. 1.2 Block diagram of photoacoustic generation [24].

1.1.1 Light transport in tissue

Transport of laser energy in tissue is characterized by the optical properties, including the absorption, the scattering, and the mean cosine single-scattering phase function (i.e., the anisotropy factor). The first parameter refers to the probability of the absorbed energy, and the latter two parameters determine the propagation direction of the photon. A diffusion model that diffuses the laser energy by taking these three parameters into account has been widely considered to solve the laser fluence inside tissue and can be expressed as [24]:

$$\frac{1}{c}\frac{\partial\Phi(r,t)}{\partial t}=D(r)\nabla^2\Phi(r,t)-\mu_a(r)\Phi(r,t)+S_0(r,t) \tag{1.1}$$

where Φ denotes the fluence and S_0 is the source term. D is the diffusion coefficient, which is defined as:

$$D=\frac{1}{3[\mu_a+\mu_s']} \tag{1.2}$$

where the μ'_s is the transport scattering coefficient, $\mu'_s=\mu_s(1\text{-}g)$. Equation (1.1) has been extensively used to calculate the laser fluence inside a turbid tissue with complex geometrics and optical heterogeneity. An assumption of neglecting all the light polarization and interference in the modeling region is applied since they are usually lost in strong scattering media.

Besides the diffusion model, the Monte Carlo simulation and the adding-doubling method have been also used to characterize the influence of absorption and scattering to the laser fluence [24, 25]. The Monte Carlo method simulates a photon moving in the tissue base on a set of rules that govern the direction and the decay of this photon. In order to yield an acceptable result, a large amount of photons is required, meaning that a significant computation time is necessary. On the other hand, the adding-doubling method has been proposed to solve the light transport equation in slab geometry [24], and it benefits to obtain the physical interpretations at each step. However, it is restricted to layered geometries and cannot be applied to complex tissues. Different from these two methods, the diffusion approximation provides more flexibility in the simulation geometrics and is much faster than the Monte Carlo method in most situations. Therefore, the diffusion approximation was chosen to be the light transport model throughout this thesis.

1.1.2 Photoacoustic propagation

After the light propagation, the deposited energy density [J/cm^3] is determined by both the resultant laser fluence and the absorption coefficient of the tissue. It can be expressed as [19]:

$$E(r,t)=\mu_a(r)\Phi(r,t)\,. \tag{1.3}$$

Assuming that all the deposited energy convert to the heat without the generation of fluoresces, the temperature rise can be calculated by using the density ρ, the specific heat C_p, and the deposited energy E.

$$\Delta T(r,t) = E(r,t) / \rho \cdot C_p \ . \tag{1.4}$$

Assuming that the laser is much shorter than the thermal relaxation time of the heated media and there is no significant heat loss, the heat diffusion during the process of the photoacoustic generation can be neglected. If this assumption holds, the "thermal confinement" is satisfied. The thermal confinement stands for the time of laser duration is shorter than that of the heat diffusion and can be described as:

$$\tau_l < \tau_{th} = \frac{z_{eff}^2}{4\kappa} . \tag{1.5}$$

τ_l is the laser pulse duration, τ_{th} is the heat diffusion time, $z_{eff}=1/\mu_{eff}$ is the optical penetration depth (in which μ_{eff} is the effective optical attenuation coefficient), and κ is the thermal diffusivity.

After the temperature rise, the wave equation of velocity potential field can be calculated by:

$$\frac{\partial^2 \varphi}{\partial t^2} - c^2 \nabla^2 \varphi = c^2 \beta \Delta T = \frac{c^2 \beta}{\rho C_p} E(r,t) \tag{1.6}$$

where φ is the scalar potential of velocity field, and β is the thermal expansibility. This equation can be rewritten since $p(r,t) = -\rho \frac{\partial \varphi(r,t)}{\partial t}$, and we can obtain:

$$\nabla^2 p - \frac{1}{c^2} \frac{\partial^2 p}{\partial t^2} = -\frac{\beta}{C_p} \frac{\partial E(r,t)}{\partial t} . \tag{1.7}$$

This is the linear wave equation for the pulsed photoacoustic signal with a source term depending on space and time. It describes the dispersing pressure field propagating from the heat source generated by the deposited laser energy. The general solution of

Eq. (1.7) is derived by using the time-retarded solution to the wave equation [26], and can be expressed in term of the deposited laser energy *E*.

$$p(r,t) = \frac{\beta}{C_p}\int\int \frac{\partial E(r_0,t_0)}{\partial t}\cdot\frac{\delta(t-t_0-\frac{r-r_0}{v})}{4\pi\left(r-r_0\right)}dr_0dt_0 \tag{1.8}$$

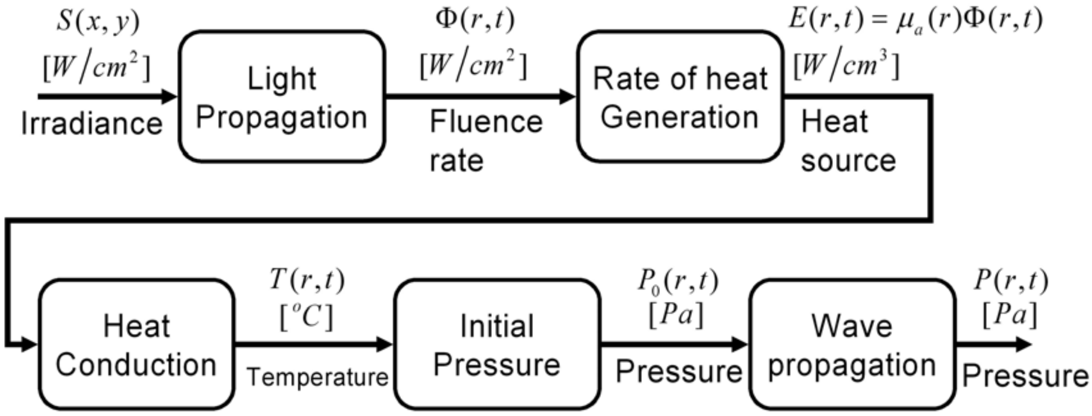

where δ denotes the Dirac-delta function. r and r_0 represent the location of propagating pressure and that of the deposited energy, respectively. Let $\eta(t)$ be the laser temporal profile. The laser fluence and the corresponding deposited energy become $\Phi(r,t)=\Phi(r)\cdot\eta(t)$ and $E(r,t)=E(r)\cdot\eta(t)$, respectively. Substituting this relation to Eq. (1.8), we can have:

$$p(r,t) = \frac{\beta}{4\pi C_p}\int\frac{E(r_0)}{\left|r-r_0\right|}\int\frac{\partial\eta(t_0)}{\partial t_0}\cdot\delta(t-t_0-\frac{r-r_0}{v})dt_0dr_0 \tag{1.9}$$

and then

$$p(r,t) = \frac{\beta}{4\pi C_p}\int\frac{E(r_0)}{\left|r-r_0\right|}\cdot\left.\frac{\partial\eta(t_0)}{\partial t_0}\right|_{t_0=t-\frac{|r-r_0|}{v}}dr_0 \tag{1.10}$$

where the 3D volume integral is carried out over the entire laser radiation region. This is the solution of the photoacoustic wave equation used to characterize the pressure wave that is generated by the deposited laser energy. It describes how the measured pressure wave at r conveys the spatial information about the optical absorption properties of the tissue and shows that to determine the optical properties from the measured photoacoustic waves is possible in the regime of the "stress confinement". The stress confinement indicates that the time of laser pulse should be shorter than that of the ultrasound traversing the heated region [27, 28].

$$\tau_l < \tau_{st} = \frac{z_{eff}}{v} \tag{1.11}$$

where τ_{st} denotes the time of ultrasound propagated out from the heated region. Once both the thermal and stress confinements are fulfilled in practice, using Eq. (1.10) becomes an effective way to describe the measured photoacoustic waves, and the relation between these waves and the distribution of optical absorption is clarified.

1.2 Objectives

1.2.1 Visualizing absorption distribution in backward mode photoacoustic imaging

To date, there are mainly three scanning modes in photoacoustic imaging, including the tomographic, the forward, and the backward modes. The schematic of these scanning modes are shown in Fig. 1.3. In the tomographic mode, the ultrasound transducer detects the photoacoustic waves by surrounding the sample on a scanning track which is perpendicular to the laser irradiation direction [29, 30]. In the forward mode, the transducer scans at the opposite side of the laser irradiation and the sample is placed between the laser source and the ultrasound transducer. In the backward mode, on the other hand, the transducer scans at the same side as the laser beam [31]. Therefore, the backward mode is easier to implement and offers a wide scanning range, and it is a potentially useful mode for biological investigations in addition to the other modes.

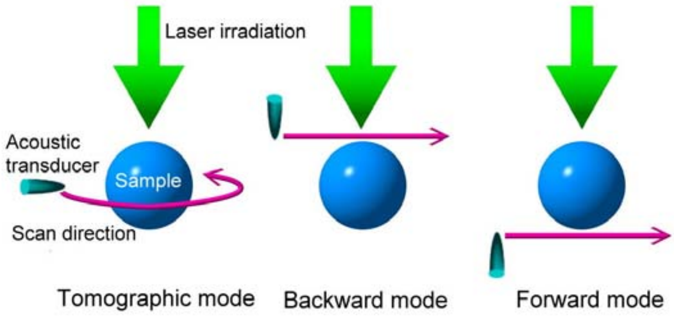

Fig. 1.3 Schematic of photoacoustic imaging, including the tomographic (left), the backward (middle), and the forward modes (right).

Several reconstruction algorithms have been proposed in the tomographic mode for various applications including the breast cancer detection [32] and the functional imaging of the rat brain [33]. On the contrary, the backward mode photoacoustic imaging is usually formed by using conventional focusing techniques. However, performance of these focusing techniques in backward mode has suffered from the small angular extent during data acquisition and is limited in visualizing only the gradient of optical absorption. In this thesis, three sequential steps of a new reconstruction algorithm are introduced to obtain the optical absorption for backward mode photoacoustic imaging. The concept of the reconstruction algorithm is shown in Fig. 1.4. First, we introduce an adaptive weighting method with the focusing technique to provide a quality-improved image. This method is based on measuring the coherence of the focusing data and has been applied to the conventional ultrasound imaging [34, 35]. Secondly, a focusing-based reconstruction method for the deposited energy is presented. This method was derived from the solution of the photoacoustic wave equation (i.e., Eq. (1.10)). Thirdly, we further extend the reconstruction algorithm to obtain the optical absorption by incorporating an iterative recovery method.

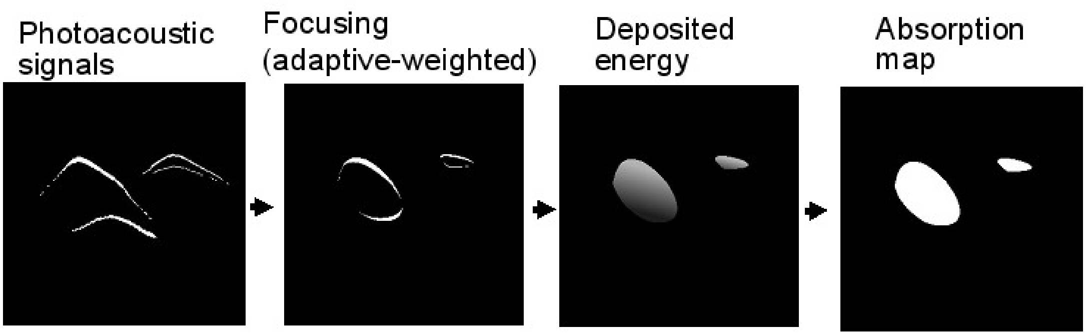

Fig. 1.4 Flowchart of the sequential steps of the proposed reconstruction algorithm.

1.2.2 Flow measurements by using photoacoustic images

In additional to the structural information from the reconstruction algorithm, the feasibility of photoacoustic imaging in assessing blood flow is also of interest since the blood flow in an organ or tissue is another important physiological index for diagnosis [36-39]. According to the principle of photoacoustic generation as introduced in Section 1.1.2, the photoacoustic signal is determined by the distribution of the deposited laser energy and hence the central frequency of the signal is dependent on the tissue structure. Unlike the conventional ultrasound, which measures the acoustic waves with a center frequency similar to the transmitted signal, the photoacoustic method detects the signal with uncertain center frequency and bandwidth. This leads the photoacoustics to be phase insensitive. Therefore, it is difficult to perform Doppler method in the photoacoustic technique.

In our previous reports, contrast-specific photoacoustic flow estimation methods have been developed [40-43]. In this method, gold nanorods have been used as the contrast agent. Although these methods have been shown to be effective, they are designed for measuring flows in large vessels with a one-dimension (1D) photoacoustic acquisition. In this study, we extend this contrast-specific method to vessels smaller than the photoacoustic sample volume using a high-frame-rate photoacoustic imaging system. One major advantage of such a 2D photoacoustic flow measurement system is that it provides both anatomical and flow information.

1.3 Organization of the dissertation

This thesis is organized as follows. Chapter 2 presents the focusing technique and the proposed adaptive-weighted method for improving the lateral resolution that is degraded because of the nondirective propagation of photoacoustic signals. A thread phantom that was made of human hairs with a strong optical absorption was produced to be the scanning object. Improvement of these focusing methods was evaluated. In Chapter 3, the second step of the proposed reconstruction algorithm for the deposited energy is introduced. Simulations and experiments were performed by using an optical absorbing phantom. The similarity and the agreement between the results with the theoretical profiles were evaluated. In Chapter 4, the reconstruction method for absorption coefficient is presented. In this step, the resultant energy deposition from the previous step was used to iteratively approach the absorption distribution. The efficacy was also evaluated in the simulation. A more realistic absorbing phantom was made to test the feasibility of this algorithm. Chapter 5 presents the implementation of flow estimation methods with a built high-frame-rate photoacoustic imaging system. Principles of the two wash-in flow velocity estimation methods (including the single-energy and dual-energy modes) are presented. Flow phantoms made by using agar and chicken breast tissue were adopted to test the efficacy of the flow velocity estimation methods. Gold nanorods that were treated to be the contrast agent in photoacoustic techniques were used to be the indicator in the flow. The experimental results were compared with the theoretical values. The influences of the laser beam size and the feasibility in *in vivo* studies are discussed. Chapter 6 discusses the efficacy of the reconstruction method in a complex sample and the feasibility of using reconstructed results to estimate the concentration of gold nanorods for flow velocity measurements. This thesis concludes in Chapter 7 with a description of future works.

Chapter 2 Coherence based backward photoacoustic imaging

In backward mode photoacoustic imaging, a cross-sectional image is formed by laterally scanning the photoacoustic signals at the same side as the laser irradiation. According to the photoacoustic wave equation (Eq. (1.10)), the photoacoustic signal detected by a transducer with a tiny active area can be regarded as a result contributed from the entire photoacoustic radiation pattern, which is determined by the product of the laser radiation pattern and the transducer directivity pattern. Therefore, using a laser beam with a particularly smaller size or a focused acoustic directivity pattern helps to achieve a quality-improved image. Although the former condition can be achieved by using a commercially available laser with a narrow beam width, strong optical scattering in tissue broadens the laser radiation pattern and thus degrades the lateral resolution, especially in a large depth. To solve this problem, we applied a combination of a synthetic aperture focusing technique with an adaptive weighting method to narrow the acoustic directivity pattern. The former technique synthesizes a large aperture by summing properly delayed signals received at different scanning positions. In the latter technique, the focusing quality is further improved by using the signal coherence as an image quality index.

2.1 Synthetic aperture focusing technique (SAFT)

The synthetic aperture focusing technique (SAFT) has been employed to improve the degraded lateral resolution in previous literature [13, 44, 45]. Fig. 2.1 illustrates the concept of the SAFT. In this figure, the transducer with a tiny active area (such as a needle hydrophone, which has a cone-shaped directivity pattern) is set to laterally scan the photoacoustic signals. The measured photoacoustic signals can be formed with a time delay depending on a distance between the photoacoustic source and the position of the transducer based on Eq. (1.10). Because of the broad photoacoustic radiation pattern, the captured photoacoustic image has a wide lateral extend. In this figure, for example, a point source in the center of the scanning direction (i.e., x-axis) can be detected in an extent of the transducer position, and the measured signals can be shown as a parabolic curve due to the time-delay. In general, the degraded lateral resolution can be improved by synthesizing a large aperture by associating a group of data captured inside the synthesized aperture and fixing the time-delay according to the relative distances [35, 44, 46, 47].

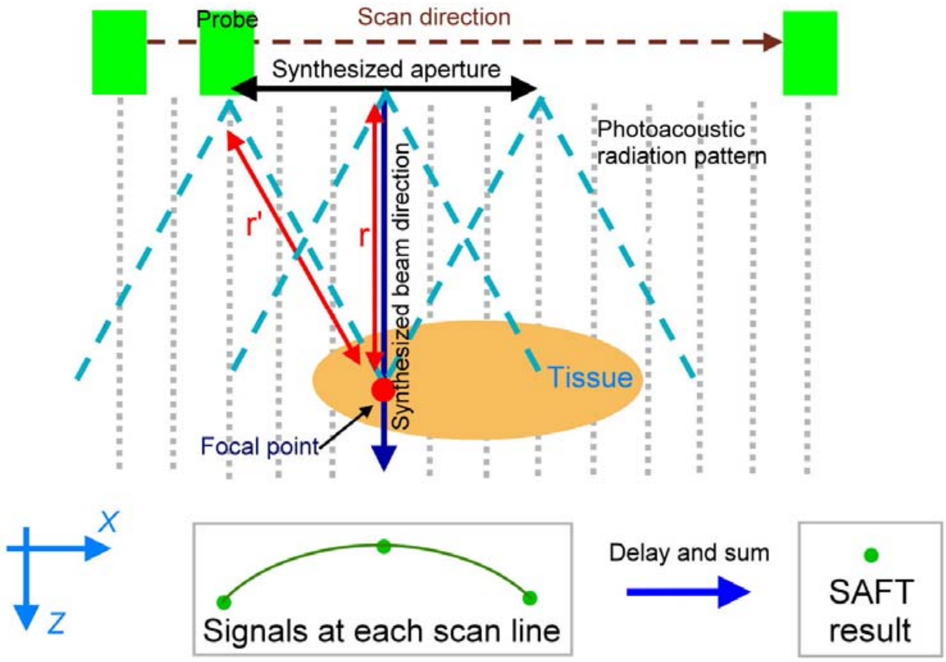

Fig. 2.1 Graphical illustration of the SAFT technique. Photoacoustic signals are measured by using a photoacoustic probe that laterally scans the tissue. The directivity pattern is indicated by the dashed triangle below the photoacoustic probe. In the SAFT, virtual beams are synthesized by associating a group of data captured inside the synthesized aperture.

By properly delaying and summing the signals received at adjacent scan lines, the SAFT provides an image with an improved resolution and can be expressed as:

$$s_{\text{focused}}(t) = \sum_{i=0}^{M-1} s(i, t - \tau_i) \tag{2.1}$$

where $s(i,t)$ is the received photoacoustic signal with time at the i-th position, τ_i is the time delay applied to the signal of scan line i, and M denotes the total number of adjacent scan lines comprised in the SAFT summation (i.e., in the synthesized aperture). τ_i corresponds to the acoustic propagation time from the synthetic focal point to the photoacoustic probe at the i-th position (where $\tau_i=(r_i'-r)/v$, and r is the depth of focus). M is determined by the angular extent of the photoacoustic radiation pattern, which is the product of the laser radiation pattern and the hydrophone's directivity pattern. A larger extent (i.e., larger M) indicates that a bigger photoacoustic aperture can be synthesized. In addition to improving the lateral resolution, the SAFT can also increase the signal-to-noise ratio (SNR). Assuming uncorrelated, additive noise (e.g., random noise), the SNR improvement is equal to 10 $\log_{10}M$.

In addition to the SAFT, the focusing quality along the depth can be coordinated by using the dynamic focusing [48]. The dynamic focusing refers to a focusing technique providing a consistent imaging quality along the depth by applying different kinds of focusing conditions corresponding to the depth of focus and can be expressed as:

$$s_{\text{focused}}(t) = \sum_{i=0}^{M-1} s(i, t - \tau_i(t)) \tag{2.2}$$

where $\tau_i(t)=[r_i'(t)-r(t)]/v$. According to Eq. (2.2), the dynamic focusing performs individual focusing delays $\tau_i(t)$ at each sampling step, meaning that each step has its corresponding delay profile and the resultant image is not only focused at a depth (meaning that a large depth of field can be performed). Fig. 2.2 presents the concept of the dynamic focusing in which a fixed f-number of all the depth was performed. The f-number denotes the ratio of the depth of focus to the aperture size and is directly related to the focusing quality [44]. Either increasing aperture size or decreasing the depth of focus improves the imaging quality. Therefore, an equivalent imaging quality along the depth can be achieved by using a constant f-number throughout the depth.

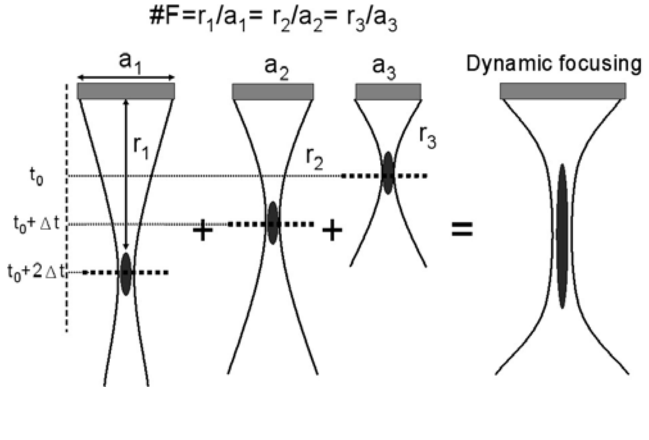

Fig. 2.2 Concept of the dynamic focusing with a constant f-number. Each depth of focus has its

corresponding delay profile and aperture size.

Numerical results of using a depth of focus at 8 mm and that of using the dynamic focusing are presented in Fig. 2.3. With a fixed delay profile, the single focusing result shows an improved lateral resolution at only the depth of 8 mm. The resolution away from the focus has a wide lateral extend. In the result using dynamic focusing, the focusing quality of all the point sources are improved, and a better imaging quality can be achieved.

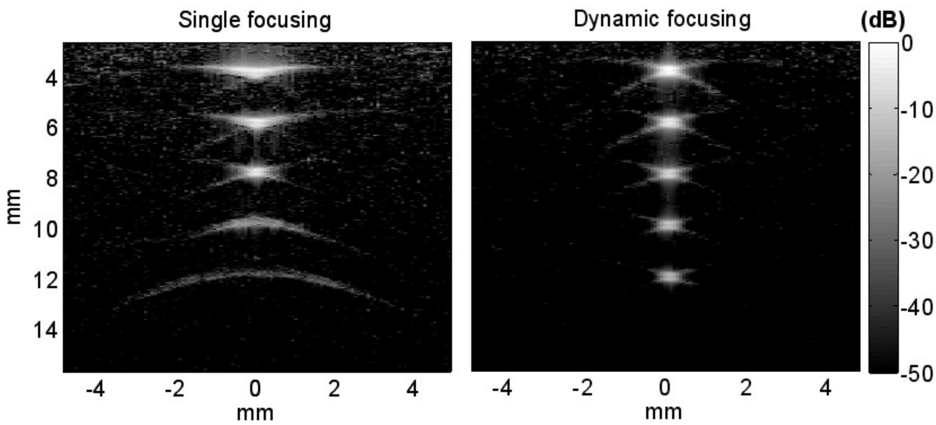

Fig. 2.3 Focusing results using a depth of focus at 8 mm (left), and the results using dynamic focusing (i.e., a longer depth of field) (right). Note that these images are shown over a 50-dB dynamic range.

2.2 Coherence factor (CF)

Besides the SAFT with the dynamic focusing, the focusing quality is further improved by utilizing the signal coherence. The coherence of the delayed signals included in the SAFT sum is estimated by the coherence factor (CF) [34, 35, 46], which is defined as

$$CF(t) = \frac{\left|\sum_{i=0}^{M-1} s(i, t-\tau_i)\right|^2}{M \cdot \sum_{i=0}^{M-1} \left|s(i, t-\tau_i)\right|^2}. \tag{2.3}$$

The numerator in Eq. (2.3) represents the energy of the coherent SAFT sum, and the denominator denotes the total incoherent energy of the delayed signals included in the SAFT sum. According to the definition, the CF is a real quantity ranging from 0 to 1. The CF is maximal when the delayed signals are identical across the synthesized aperture (i.e., perfectly coherent), as illustrated in Fig. 2.4(a). Fig. 2.4(a) shows the delayed scan lines corresponding to the case where the point photoacoustic source is in the direction of the synthesized beam. In the figure, the vertical axis is the depth and the horizontal axis is the synthesized aperture direction (i.e., the scan direction). In other words, the CF of an on-axis point source without focusing errors equals 1. Fig. 2.4(b) shows the case where the point source is not on the synthesized beam axis, which corresponds to a steering error in the SAFT. The CF is low in this case since a destructive summation occurs in the numerator of Eq. (2.3). As illustrated in the above two examples, the CF can be used as a focusing-quality index for the SAFT. A high CF indicates that the image intensity should be maintained because the photoacoustic sources are in the direction of the synthesized beam. Otherwise, a low CF should be used to reduce the image intensity because of the presence of significant focusing errors. Based on this property, a coherence-factor weighting (CFW) technique can be developed to further improve the focusing quality of the SAFT. The CF-weighted signal, $s_{\text{weighted}}(t)$, of the SAFT signal $s_{\text{focused}}(t)$ can be expressed as

$$s_{weighted}(t) = s_{focused}(t) \cdot CF(t) . \tag{2.4}$$

Note that the CFW has to be performed at each imaging point. Because measurement noise is generally incoherent, the CFW technique also improves the SNR.

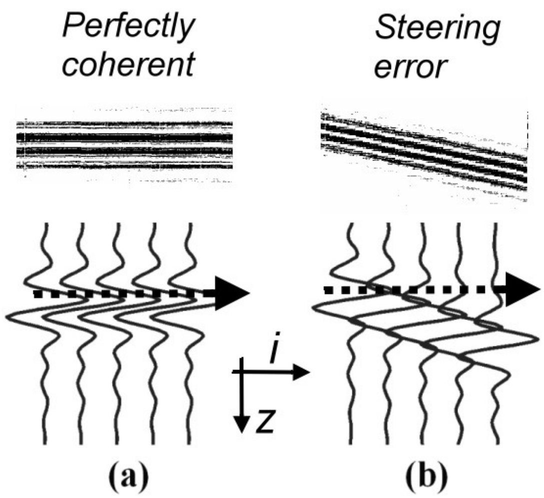

Fig. 2.4 Delayed scan lines. (a) Case where the point photoacoustic source is in the direction of the synthesized beam without focusing errors. (b) Case where the point photoacoustic source is not in the

direction of the synthesized beam, corresponding to a steering error. The vertical axis is the depth and the horizontal axis is the synthesized aperture direction.

2.2.1 Numerical simulations

Numerical simulations were applied to demonstrate the efficacy of CF. The solution of photoacoustic wave equation was used to produce the received signals at all the scanning positions. A phantom (i.e., the scanning object) comprising 5 points was used. Each point with a diameter of 200 μm was separated by 2 mm axially and 1mm laterally. The laser temporal profile was set to be a Gaussian pulse with a duration of 25 ns. The Grüneisen coefficient inside the phantom was a constant. The sound velocity was set to be 1500 m/s. The pressure waves were acquired at a depth 4 mm above the top point target. The scanning step size and the data sampling frequency were 20 μm and 75-MHz, respectively.

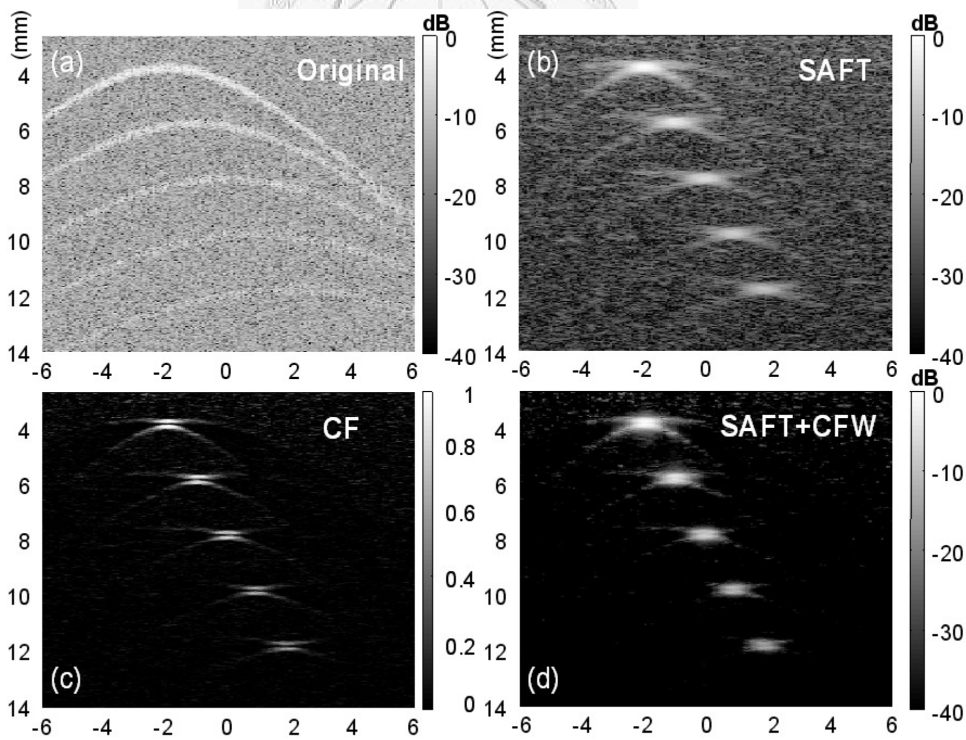

Fig. 2.5 Simulation images of the photoacoustic phantom with 5 point targets, including the original image (a), the SAFT image (b), the CF map (c), and the SAFT-plus-CFW image (d). Note that (a),(b), and (c) are shown over a 40-dB dynamic range, and the vertical axis is the depth and the horizontal axis is the lateral position.

Fig. 2.5 shows the simulation results. These images are displayed over a 40-dB dynamic range. Thermal noise (uniformly distributed random noise) was added to the received pressure waves to result in a SNR of 6 dB. The vertical axis is the depth and the horizontal axis is the lateral position (both in millimeters). Because of the broadened photoacoustic radiation pattern, the original image of these points cannot be correctly recognized (Fig. 2.5(a)). After using the SAFT with the dynamic focusing, a focused image can be obtained, as shown in Fig. 2.5(b). A uniform lateral resolution along the depth was achieved. In this image, sidelobes resulted due to the focusing with a finite aperture size (i.e., a small angular extent) are also clearly seen [35, 46]. The final image after the CFW was shown in the Fig. 2.5(d). Apparently, both the sidelobes and the background noise were noticeably reduced.

2.2.2 Phantom experiments

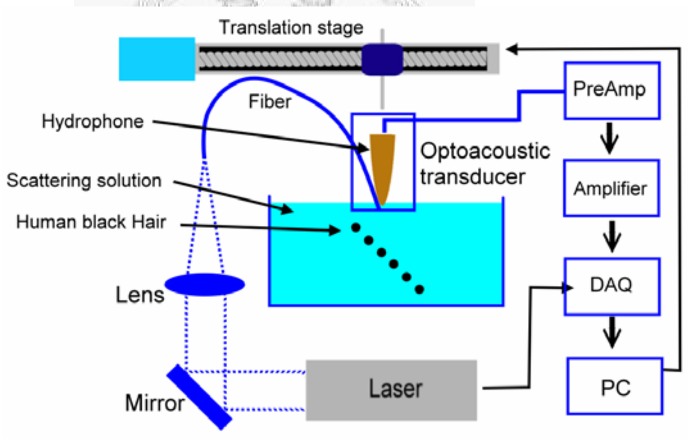

Fig. 2.6 Schematic diagram of the photoacoustic imaging system. A Nd:YAG laser operating at 532nm was used to irradiate the phantom through a 1,000μm fiber with an energy of 25mJ. A photoacoustic probe consisted of the fiber and a hydrophone was fixed on the translation stage to scan the phantom. The photoacoustic phantom comprised six human black hairs 90 μm in diameter, a ~150 cm^{-1} absorption was immersed in the milk solution and separated by 2 mm both axially and laterally. The photoacoustic signals were digitalized and stored by the DAQ card inside the personal computer.

To further demonstrate the efficacy of the CFW, a photoacoustic scanning system has been built. This system consisted of a precision translation stage (CSR200, CSIM), a laser system, and an acoustic-wave receiving system as shown in Fig. 2.6. A frequency-doubled Nd:YAG laser (LS-2132U, LOTIS TII) operating at 532 nm with a pulse duration of 8 ns was used for optical irradiation. The laser beam was split and focused by lenses onto a 1,000-μm fiber (FT-1.0-UMT, Thorlabs) with an optical energy of 1.67 mJ and a 15-Hz pulse repetition rate. An ultrasonic needle hydrophone (GL-200, ONDA) with a flat frequency response from 0.2 to 20 MHz was employed to detect the photoacoustic waves. The active area of the hydrophone had a diameter of 200 μm. We constructed the photoacoustic probe by combining the fiber and the needle hydrophone on a single holder. This probe was mounted on the translation stage, and mechanically scanned with a 100 μm step size. The acoustic waveforms were amplified by an acoustic amplifier (5072PR, Panametrics) and then recorded by a data acquisition card (CompuScope 12100, Gage) at a 100-MHz sampling rate. The acquired data were stored in a personal computer for subsequent data analysis.

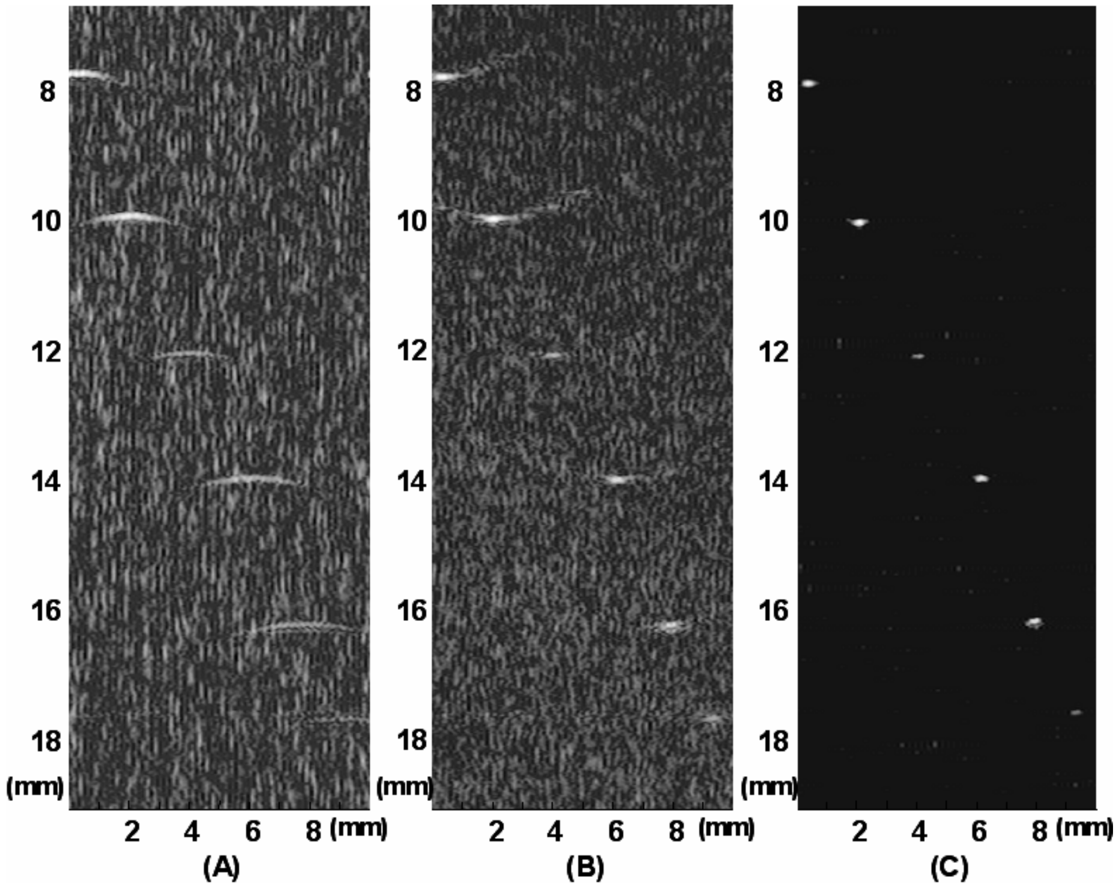

Fig. 2.7 Images of the photoacoustic phantom containing six hair threads. (a) Original image. (b) SAFT image. (c) SAFT+CFW image. The dynamic range is 30 dB. The vertical axis is the depth and the horizontal axis is the lateral position, both in mm.

The point spread function of the imaging system was evaluated by considering a cross-sectional view of a photoacoustic hair-thread phantom. The photoacoustic phantom comprised six human black hairs 90 μm in diameter, a ~150 cm^{-1} absorption coefficient [49], and a solution of 1% milk in water as the scattering medium with a scattering coefficient of 3.69 cm^{-1}, which was measured by a double integrating sphere system. The hair threads were immersed in the solution and separated by 2 mm both axially and laterally, and they were the only absorbers in the phantom. The tip of the hydrophone was 3 mm below the surface of the solution and 5 mm above the first thread.

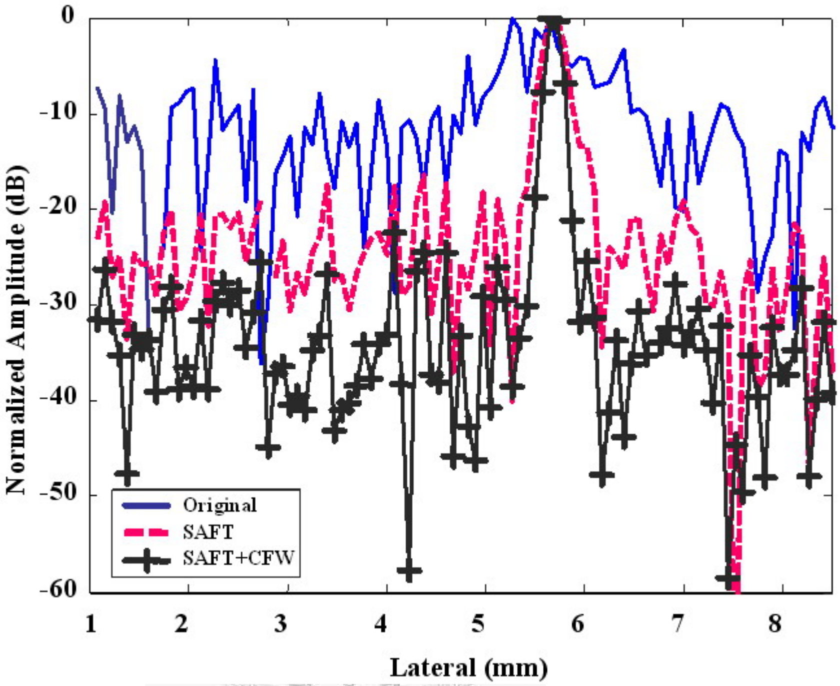

Fig. 2.8 The lateral signals of the third target. A poor result of original photoacoustic signal was showed (solid line). The SAFT improved both the SNR and lateral resolution here (dashed line). More effectively improved by applying CF weighting (cross line).

Fig. 2.7 shows the images of the photoacoustic phantom. Fig. 2.7 (a), (b), and (c) are the original photoacoustic image, the SAFT image, and the SAFT-plus-CFW image, respectively. These images are displayed over a 30-dB dynamic range. The vertical axis is the depth and the horizontal axis is the lateral position, both in millimeters. Due to the broadened photoacoustic radiation pattern, the six hair threads shown in Fig. 2.7(a) have a wide lateral extent, indicating poor lateral resolution. The SAFT image in Fig. 2.7(b) exhibits improved lateral resolution and SNR: the former is due to the synthesis of a larger effective aperture, and the latter is a direct consequence of the delay and sum operations. The data from each synthesized aperture were also used to estimate the CF map. The final image produced by weighting (i.e., multiplication) of the SAFT image by the CF map on a pixel-by-pixel basis is presented in Fig. 2.7(c). Compared with the SAFT image shown in Fig. 2.7(b), the signals around the point source are noticeably suppressed. Moreover, the image background noise is reduced after the CFW. The results of the fourth hair target from the top along the lateral direction were shown in Fig. 2.8. Note that the results were obtained from the images on a decibel scale. From the SAFT results, we can identify the target position at 5.7 mm easier and the SNR increased from 8dB to 20dB. Applying the CF weighting in SAFT image provided further improvement on the lateral resolution (from 400μm to 250μm) and increased the SNR to 25dB.

Table 2.1: Lateral width (-6dB) and the SNR values

Target Depth (mm)	**Original (μm/dB)**	**SAFT (μm/dB)**	**SAFT + CFW (μm/dB)**
8	1200/25	425/31	**250/41**
10	1300/23	550/32	**225/41**
12	2700/13	450/18	**280/26**
14	1800/15	400/27	**250/38**
16	2000/16	420/21	**260/33**
18	>2500/12	450/15	**280/19**

The SNR and lateral resolution results for all targets are listed in Table 2.1, in which the SNR is defined as the difference between the maximal intensity at the hair thread position and the average noise intensity. The wide photoacoustic radiation pattern led to broad widths of the images of the hair threads and the low SNR in the original photoacoustic image. The SAFT formed a narrow photoacoustic beam, which reduced the –6dB width of the hair threads to 400–550 μm at all depths. The lateral resolution was further improved using CFW to 225–280 μm. Moreover, the SAFT improved the SNR by 3–12 dB, and when combined with CFW provided an additional SNR improvement of 4–12 dB. The improved lateral resolution and SNR in the final image result in a reliable representation of this phantom.

2.3 Discussion

2.3.1 Cylindrical object

For further demonstration, images of a contrast phantom containing a poly(vinyl alcohol) [50] cylinder with a diameter of 3.5 mm are shown in Fig. 2.9. The cylinder was submerged at a depth of 5 mm in the milk solution (with the same scattering properties as the one shown in Fig. 2.7). In this figure, panel (a) shows the original image, panel (b) is the SAFT image, and panel (c) is the SAFT+CFW image. Note that the upper edge of the cylinder was more visible than the lower edge. Such a characteristic is similar to that shown in reference [51]. Both the edge definition and the SNR were markedly improved.

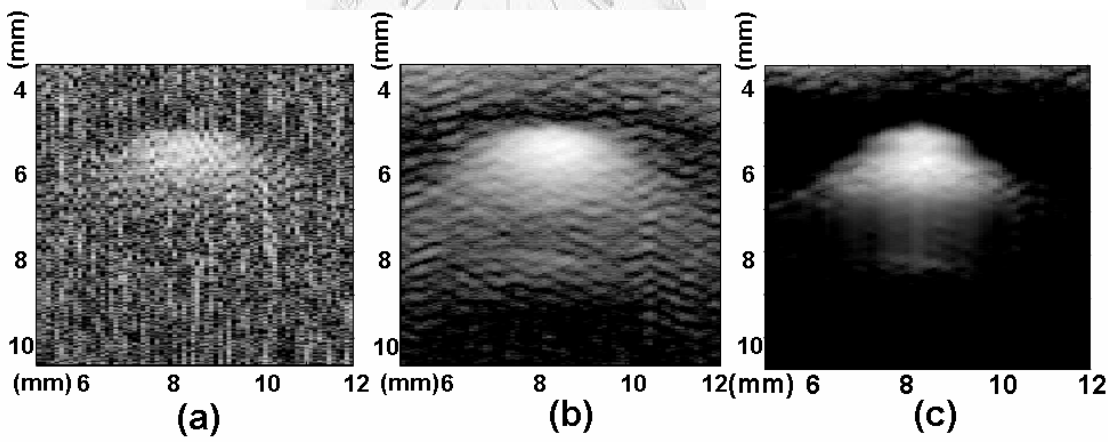

Fig. 2.9 Images of a cylindrical object. (a) Original image. (b) SAFT image. (c) SAFT+CFW image. The phantom consisted of poly(vinyl alcohol)10 gel and was located at a depth of 5 mm. The diameter was 3.5 mm and had an absorption coefficient of 4.42 cm^{-1}. The milk solution had a scattering coefficient of 3.69 cm^{-1}.

The above experiment results show that even if the size of the scanning object is greatly larger than that of a hair thread, the results present a high quality image. Both the SNR and the resolution are improved. It also demonstrates that the CF weighting helps to increase the focusing performance not only in a small target but also in objects with a large size such as an optically homogeneous tissue.

2.3.2 Influence of the SNR

In Section 2.2, the CF was defined without taking noise into consideration (i.e., an infinite SNR was assumed). However, in realistic practice, thermal noise affects the accuracy of the measured photoacoustic signals. With the thermal-noise interferences, the CF equation (Eq. (2.3)) can be rewritten as:

$$CF_{noise}(t) = \frac{\left|\sum_{i=0}^{M-1}\left[s(i,t-\tau_i)+n_i\right]\right|^2}{M \cdot \sum_{i=0}^{M-1}\left|s(i,t-\tau_i)+n_i\right|^2} \tag{2.5}$$

where CF_{noise} is the noise-disturbed CF value, and n denotes the thermal-noise in which the mean value of n approaches to zero (i.e., $\bar{n} = \frac{1}{m}\sum_{k=0}^{m} n_i \simeq 0$), meaning that

$$CF_{noise}(t) = \frac{\left|\sum_{i=0}^{M-1} s(i,t-\tau_i) + \sum_{i=0}^{M-1} n_i\right|^2}{M\sum_{i=0}^{M-1}\left|s(i,t-\tau_i)+n_i\right|^2} = \frac{\left|\sum_{i=0}^{M-1} s(i,t-\tau_i)\right|^2}{M\sum_{i=0}^{M-1}\left|s(i,t-\tau_i)+n_i\right|^2}. \tag{2.6}$$

If the delayed data, s, in the synthesized aperture are coherent, the spectrum of the delayed data is mainly distributed around the DC [35]. On the contrary, the thermal-noise is typically in a flat power spectrum density. Therefore, the overlap of these two spectra can be neglected, and $\left|S(e^{jw})+N(e^{jw})\right|^2 \approx \left|S(e^{jw})\right|^2 + \left|N(e^{jw})\right|^2$. Under this condition, the denominator in Eq. (2.6) can be derived to be the sum of both the signal energy and the noise energy based on Parseval’s relation.

$$\begin{aligned} \sum_{i=0}^{M-1}\left|s(i)+n(i)\right|^2 &= \frac{1}{2\pi}\int_{-\pi}^{\pi}\left|S(e^{jw})+N(e^{jw})\right|^2 dw \\ &\approx \frac{1}{2\pi}\int_{-\pi}^{\pi}\left[\left|S(e^{jw})\right|^2+\left|N(e^{jw})\right|^2\right]dw = E_s + E_n \end{aligned} \tag{2.7}$$

where $E_s = \sum_{i=0}^{M-1} |s(i,t)|^2$ and $E_n = \sum_{i=0}^{M-1} |n(i)|^2$ represent the spectral energy of the signal and the noise, respectively. Substituting Eq. (2.7) into Eq. (2.6), we can have

$$CF_{noise}(t) \cong \frac{\left|\sum_{i=0}^{M-1} s(i,t)\right|^2}{\frac{M}{2\pi}\int_{-\pi}^{\pi}\left[\left|S(e^{jw})\right|^2 + \left|N(e^{jw})\right|^2\right]dw} = \frac{\left|\sum_{i=0}^{M-1} s(i,t)\right|^2}{M(E_s + E_n)}, \tag{2.8}$$

and

$$CF_{noise}(t) \cong \frac{\left|\sum_{i=0}^{M-1} s(i,t)\right|^2}{M \cdot E_s \cdot (\frac{E_n}{E_s} + 1)} = \frac{\left|\sum_{i=0}^{M-1} s(i,t)\right|^2}{M \cdot E_s} \cdot \frac{SNR}{SNR+1} = CF(t) \cdot \frac{SNR}{SNR+1} \tag{2.9}$$

where the $SNR = E_s/E_n$. According to Eq. (2.9), the noise-disturbed CF value is determined by the SNR. If the SNR is infinite (i.e., E_n equals to zero), the CF_{noise} equals to the CF. Otherwise, when the SNR decreases, the measured CF_{noise} value becomes lower than the theoretical CF value.

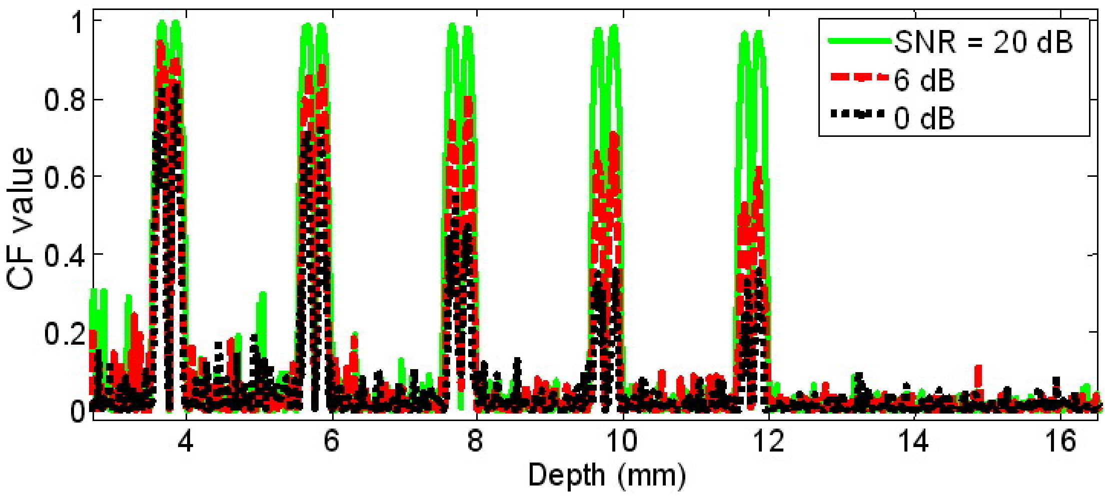

Fig. 2.10 CF values long the depth (i.e., the vertical projections of the CF maps) calculated from random-noise added photoacoustic signals with a SNR of 0 dB (dotted), 6 dB (dashed), and 20 dB (solid). It is obvious that the signals with a high SNR have a CF value approximated to unity, and the CF value decreases with the SNR.

Fig. 2.10 presents the CF values calculated from the simulated photoacoustic signals with a SNR of 0, 6, and 20 dB. It is obvious that the resulting CF value is dependant on the SNR. The noise-disturbed CF value directly affects the intensity of the focusing results. In the backward mode photoacoustic imaging, laser energy decays with the depth, and the SNR and the following CF value also decrease with the penetration depth. Fig. 2.11 shows the image after the CFW with a SNR of 40 dB and 6 dB. The result with a SNR of 6 dB shows image intensity lower than that of 40 dB, especially in a large depth. Therefore, using the CFW in low-SNR regions becomes a tradeoff between the lateral resolution and the signal intensity.

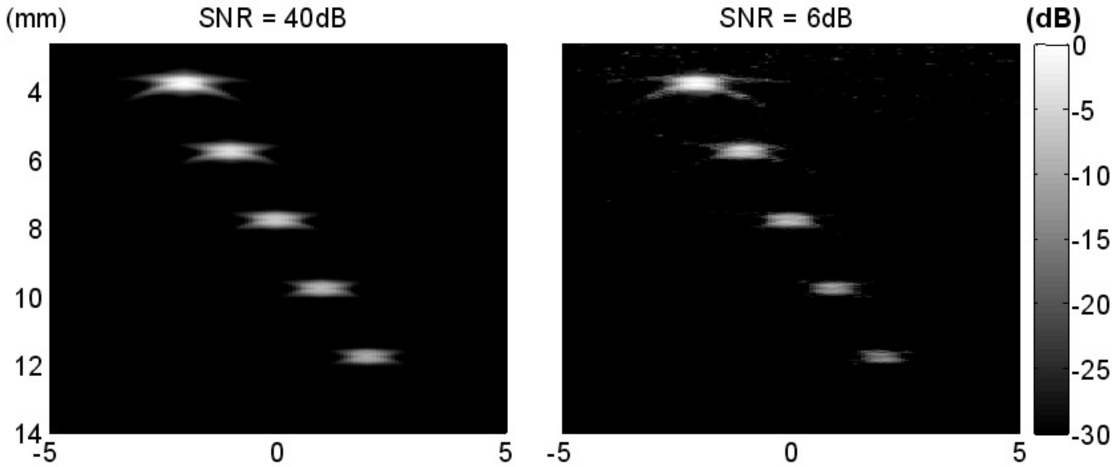

Fig. 2.11 SAFT+CFW results with a SNR of 40 dB (left), and 6 dB (right). The calculated CF map is sensitive to the noise. The result with a SNR of 6 dB shows image intensity lower than that of 40 dB, especially in a large depth.

2.4 Concluding remarks

In this chapter, we demonstrated the efficacy of the SAFT-plus-CFW method in both the numerical simulations and the experiments. The results show that the SAFT-plus-CFW improved lateral resolution by 2 times and the SNR by 4–12 dB over the conventional techniques. We also discussed the influence of the noise to the CF value. The relation between the CF value and the SNR was clarified. According to Eq. (2.9), a theoretical CF value can be obtained only if the noise approaches to zero. However, it is difficult to achieve since numerous kinds of noise couple with the received signals in practice.

Chapter 3 Reconstruction of energy deposition (RED)

Typical reconstruction methods in the backward mode photoacoustic imaging include the beam-forming method (e.g., the SAFT) [12, 44, 45, 52-55], the Fourier transform method [13], and the back-projection method [56]. However, success of these methods has been primarily demonstrated with layered structures and the ability of the backward mode photoacoustic imaging in measuring optical energy disposition for heterogeneous tissue structures has been limited. In this chapter, an effective reconstruction algorithm derived from the solution of the photoacoustic wave equations is introduced. The solution of the photoacoustic wave equations for pressure in 3D shows that the photoacoustic wave is determined by the geometric distribution of the optical absorber inside the photoacoustic radiation pattern [30, 54]. The concept of the proposed algorithm is to reduce the reconstruction problem to 1D by line focusing via the SAFT-plus-CFW [46], and the reconstruction can be performed. Note that it is the previous step to approach the optical absorption in the proposed reconstruction algorithm.

3.1 Reconstruction algorithm

The RED was derived from the solution of the photoacoustic wave equation (as expressed in Eq. (1.10)). This equation shows that the measured photoacoustic wave is determined by the spatial distribution of the optical energy deposition inside the photoacoustic radiation pattern [30, 54]. The photoacoustic radiation pattern is defined as the overlap of the laser radiation pattern with the ultrasound directivity pattern. It also determines the lateral resolution of the photoacoustic imaging. In Chapter 2, we introduced the SAFT-plus-CFW to improve the imaging quality by synthesizing a virtual aperture and reforming the photoacoustic radiation pattern. Following this concept, the RED for obtaining the energy deposition is to reduce the reconstruction problem from 3D to 1D by line focusing via the SAFT-plus-CFW.

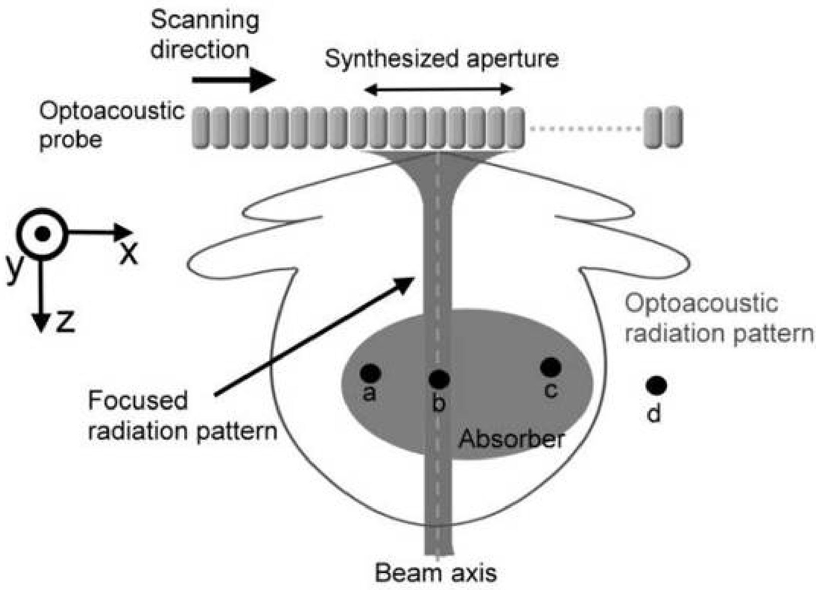

Fig. 3.1 Focused radiation pattern in the backward mode photoacoustic imaging. Note that the hydrophone has a small active area with a corresponding broad directivity pattern which covers the point absorbers “a-c”. By associating a group of signals measured from adjacent scanning positions, a new virtual aperture is synthesized with a focused radiation pattern. Under this condition, the virtual aperture detects only the photoacoustic sources on the focused radiation pattern (i.e., the point source “c”).

Fig. 3.1 shows the schematic diagram of a typical backward photoacoustic imaging system with a hydrophone. Consider four photoacoustic point sources denoted as “a”, “b”, “c” (points located inside the photoacoustic radiation pattern) and “d” (located outside the radiation pattern). The signals from the points “a”, “b”, and “c” can be detected with the original photoacoustic radiation pattern. Assuming that a perfect focusing (i.e., an infinite aperture size) is achieved, the photoacoustic radiation pattern can be reformed to a 1D line, and each scanning position receives only the photoacoustic waves propagated from the sources inside the line as shown in Fig. 3.1. After focusing, only the signals from the point “b” are detected. Under this condition, the pressure waves measured at each scanning position x (i.e. each channel) can be rewritten as:

$$p(t)\big|_x = \frac{\beta}{4\pi C_p}\int \frac{E(z)\big|_x}{z}\cdot\left.\frac{d\eta(t_0)}{dt_0}\right|_{t_0=t-\frac{z}{v}} dz \qquad (3.1)$$

where the $p(t)|_x$ is the result of the focusing technique at the scan position x. $E(z)|_x$ denotes the 1D profile of the deposited energy along the depth at the scan position x. It is the product of the spatial distribution of laser energy $\Phi(z)|_x$ and optical absorption coefficients $\mu_a(z)|_x$. η denotes the temporal profile of laser irradiation. Note that the distance from the source to the detector is simplified to be the depth (i.e., $z = r - r_0$). The focused pressure waves at each scan position are then integrated with respect to t_0 from $-\infty$ to t, which gives

$$\hat{p}(t)\Big|_x = \int_{-\infty}^{t} p(\tau)\Big|_x d\tau = \frac{\beta}{4\pi C_p}\int \frac{E(z)\big|_x}{z}\cdot\int_{-\infty}^{t}\frac{d\eta(t_0)}{dt_0}\Bigg|_{t_0=\tau-\frac{z}{v}} d\tau\cdot dz \tag{3.2}$$

where $d\tau = dt_0$, and

$$\hat{p}(t)\Big|_x = \frac{\beta}{4\pi C_p}\int \frac{E(z)\big|_x}{z}\cdot\eta(t-\frac{z}{v})dz\,. \tag{3.3}$$

The above equation can be rewritten as a convolution sum of the 1D profile of the deposited energy with the temporal profile of laser irradiation.

$$\hat{p}(t)\Big|_x = \frac{\beta}{4\pi C_p}\cdot\left[\frac{E(z)\big|_x}{z}\otimes\eta(t\cdot v)\right]. \tag{3.4}$$

Therefore, the optical energy deposition along the depth can be calculated as:

$$E(z)\Big|_x = \frac{4\pi\cdot z\cdot C_p}{\beta}\cdot deconv\left\{\hat{p}(t)\Big|_x, \eta(t\cdot v)\right\}. \tag{3.5}$$

As mentioned previously, the temporal profile of the laser irradiation is a short pulse since it is in the regime of thermal confinement. Therefore, it can be regarded as a Dirac delta function and $\eta(t\cdot v_s)=\delta(t\cdot v_s)$. Subsequently, Eq. (3.5) can be rewritten as

$$E(z)\Big|_x = \frac{4\pi\cdot z\cdot C_p}{\beta}\cdot \hat{p}(t)\Big|_x\,. \tag{3.6}$$

Finally, the image of optical energy deposition can be reconstructed by applying this algorithm with all the scan lines.

The RED mainly approaches to the deposited laser energy from the far field photoacoustic signals which are disturbed due to the acoustic diffractions. The relation between the far field photoacoustic signals and the optical energy deposition profile has been reported in investigating layered structures without considering the broad photoacoustic radiation pattern [57]. In this method, the detected photoacoustic signals are integrated to obtain the profile of the optical energy deposition in a layer structure. Nevertheless, the strong optical scattering has to be considered in the biological tissue since the broadened photoacoustic radiation pattern affects the accuracy of this reconstruction.

According to the Eq. (3.2)-(3.6), the energy deposition is treated as a function of the measured pressure wave after focusing and the RED can be achieved as follows:

(1) measure the photoacoustic wave, $p(t)$;

(2) apply the SAFT-plus-CFW_d to result in a quality-improved image, $p(t)|_x$;

(3) integrate these focused signals along the depth to obtain $\hat{p}(t)|_x$;

(4) comprise these results according to their corresponding lateral position to result in an image.

Note that, a new CF_d is adopted instead of CF in the second step. The CF_d is produced from the differential photoacoustic signals and can be expressed as:

$$CF_d(t) = \frac{\left|\sum_{i=0}^{M-1} s'(i, t-\tau_i)\right|^2}{M \cdot \sum_{i=0}^{M-1} \left|s'(i, t-\tau_i)\right|^2} \tag{3.7}$$

where s' is the differentiation of the photoacoustic signals with respect to the depth. Because the differentiation can be treated as a high-pass filter, the CF_d is formed to provide a better lateral resolution.

3.2 Numerical simulations

To demonstrate the validity of the RED in the backward mode photoacoustic imaging, numerical simulations were performed to obtain photoacoustic waves. These simulations were achieved by using MATLAB based on the scanning setup of the backward mode as shown in Fig. 3.1. The ultrasound transducer and the laser irradiation were placed above the scanning object. Two steps have to be considered to perform this simulation. First of all, two optical properties, including the absorption μ_a and the scattering coefficients μ_s, in tissue were determined based on the optical properties of the tissue under investigation. These parameters were given with 2D distributions. In this study, a anisotropy factor, g, was set to be 0.9 as an averaged constant value that has been utilized in previous literature since the scattering in biological tissue is strong forward-directed [19, 24]. With these optical parameters, the next step was to compute the laser fluence inside the tissue based on the diffusion approximation as described in Chapter 1. In Chapter 1, we briefly introduced the time-resolved diffusion process as a tool that characterizes the interaction between the incident laser source and the optical properties inside a turbid media, as expressed by Eq. (1.1). Nevertheless, since we have determined that the laser duration is in a sufficiently short time period and satisfies both the thermal and the stress confinements in all the practices in this thesis, the propagation of the induced photoacoustic wave can be treated as a following process after the heating is finished. Under this assumption, the diffusion of the laser source can be regarded as a stationary problem, meaning that $\partial\Phi(r,t)/\partial t$ equals to zero, and the time parameter, t, is dropped in Eq. (1.1).Therefore, we can have [25, 58-60]

$$-D(r)\nabla^2\Phi(r) + \mu_a(r)\Phi(r) = S_0(r) \tag{3.8}$$

where $D(r)$ is the diffusion coefficient. S_0 is the laser source. We used the partial differential equation toolbox (MATLAB, The Mathworks, MA, USA) to solve this elliptic equation with boundary conditions. In general, two boundary conditions including the Dirichlet and the Robin conditions have been considered in literature [60]. The Dirichlet boundary condition determines the light fluence on the boundary of the simulation domain to zero.

$$\Phi(\xi) = 0\,, \quad \forall \xi \in \partial\Omega \tag{3.9}$$

where ξ presents the position on the boundary. Equation (3.9) indicates that a perfect optical absorber surrounds the simulated domain Ω and thus the light energy goes out through the boundaries will be absorbed. The Robin condition models a nonscattering media surrounding the domain and can be expressed as:

$$\Phi(\xi) - 2\hat{n}D \cdot \nabla\Phi(\xi) = 0\,,\quad \forall \xi \in \partial\Omega\,. \tag{3.10}$$

$\hat{n}$ is the normal to $\partial\Omega$. This condition represents that no reflection occurs on the boundary and is commonly used as a more realistic approach. Here, we adopt Robin boundary condition in all the simulations in this thesis.

After the calculation of the fluence, the results were then used to produce the deposited energy by multiplying the absorption coefficient as described in Eq. (1.3). Note that the parameter t was dropped since the thermal-confinement was satisfied. The next step of this simulation is to obtain the acoustic waves propagated from the deposited energy. The deposited energy calculated from the prior step was treated as the source term in the photoacoustic wave equation (Eq. (1.7)), and the resulting photoacoustic waves measured at a predetermined transducer position can be acquired by the solution of this wave equation (Eq. (1.10)). Note that both the acoustic nonlinearity and attenuation were neglected and the speed of sound was set to be a constant value of water (v=1500 m/s) throughout the simulation region.

Fig. 3.2 presents a basic case of the simulation, in which the vertical and the horizontal axes are the depth and the lateral position (both in millimeters), respectively. The simulation region, Ω, is a square with a base 10 mm long. Laser energy was set to homogeneously irradiate from the top of the simulation region (at the depth of 0 mm). The laser temporal profile was set to be a Gaussian pulse with a duration of 25 ns. A rectangular optical absorber with a size of 2 mm in width and 1.5 mm in thickness was located at a depth of 2 mm below the laser irradiation. The absorber with an absorption coefficient of 8 cm^{-1} was placed at a depth of 4 mm, as shown in Fig. 3.2(a). The scattering coefficient was 50 cm^{-1} throughout the simulation region. After the light diffusion, the resultant laser fluence and the following energy deposition are shown in Fig. 3.2(b) and Fig. 3.2(c), respectively. It is clear that after the light transport the laser energy decayed along the depth due to the absorption of the rectangular sample and the strong scattering of the entire simulation region. The deposited energy, therefore, exhibits a concave distribution (the center of the rectangle absorbs the energy lower than the edges).

After the first step, the deposited energy was then used to obtain the photoacoustic wave based on the solution of photoacoustic wave equation. A transducer was placed on the top of the simulation region and scanned with a step size of 20 μm and a sampling frequency of 75 MHz. Thermal noise was added to the received signals to result in a SNR of 20 dB, as shown in Fig. 3.2(d). The radiation pattern of the transducer was set to be a sector shape with a wide beam divergence of 65-degree. Because of the broad radiation pattern, the detector received the photoacoustic waves propagated from almost entire region of the absorber and thus the lateral resolution was degraded.

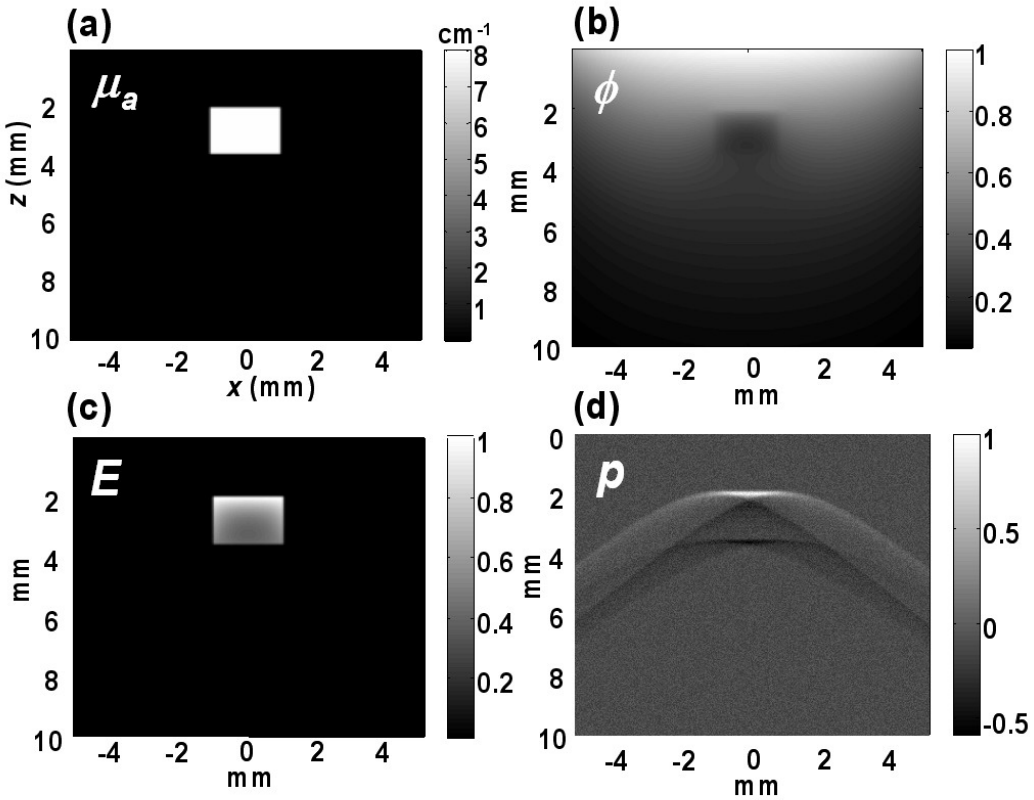

Fig. 3.2 Images of the optical absorption coefficient (a), the corresponding laser fluence (b), the energy deposited (c), and the photoacoustic signals received at z=0 (d). Note that thermal noise was added in the measured photoacoustic signals to result in a SNR of 20 dB.

Numerical generation of the photoacoustic waves was now completed and these photoacoustic signals were ready to be used to test the proposed algorithms. According to the algorithm of the RED as mentioned in the previous section, the photoacoustic signals were first focused by using the SAFT-plus-CFW_d. Fig. 3.3(a) and (b) shows the focused image of the absorber using the SAFT and the SAFT-plus-CFW_d, respectively, in which the f-number was set to be unity. It is obvious that both of these images reveal mainly the top and bottom edges of the absorber and the deposited energy inside the absorber are missing. Therefore, it is difficult to distinguish the shape of the target from these two images.

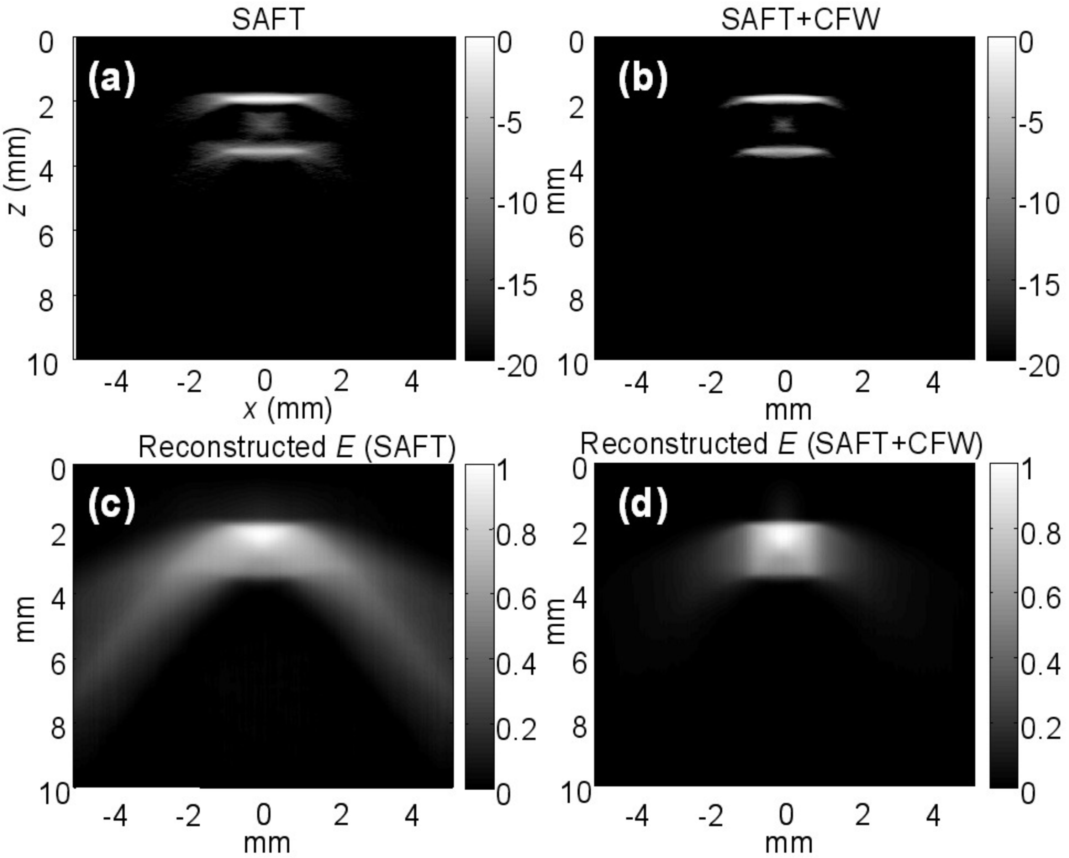

Fig. 3.3 Quality-improved images by using the SAFT (a) and the SAFT+CFW$_d$ (b), and the reconstructed energy deposition, *E*, from the SAFT (c) and the SAFT+CFW$_d$ results (d). Note that the focused images are displayed over a 20-dB dynamic range.

By applying the proposed algorithm, the images of the energy deposition are shown in Fig. 3.3(c) and (d). These two images were reconstructed by using the focused images after the SAFT and the SAFT-plus-CFW$_d$ (corresponding to Fig. 3.3(a) and (b), respectively). The reconstructed image shows a rectangle with mostly a same position and shape as the theoretical value shown in Fig. 3.2(c). However, the reconstructed image from the SAFT results (Fig. 3.3(c)) reveals greatly elevated sidelobes, meaning that the lateral resolution is poor. This is due to the insufficient focusing of the low frequency since the RED applies integration along the depth and greatly increases the signal intensity around the DC. Fortunately, reconstruction results using the SAFT-plus-CFW$_d$ presents a better lateral resolution and the shape is much similar to the predetermined energy deposition. The ability of CFW$_d$ to reduce the sidelobes and to improve the imaging quality is again demonstrated.

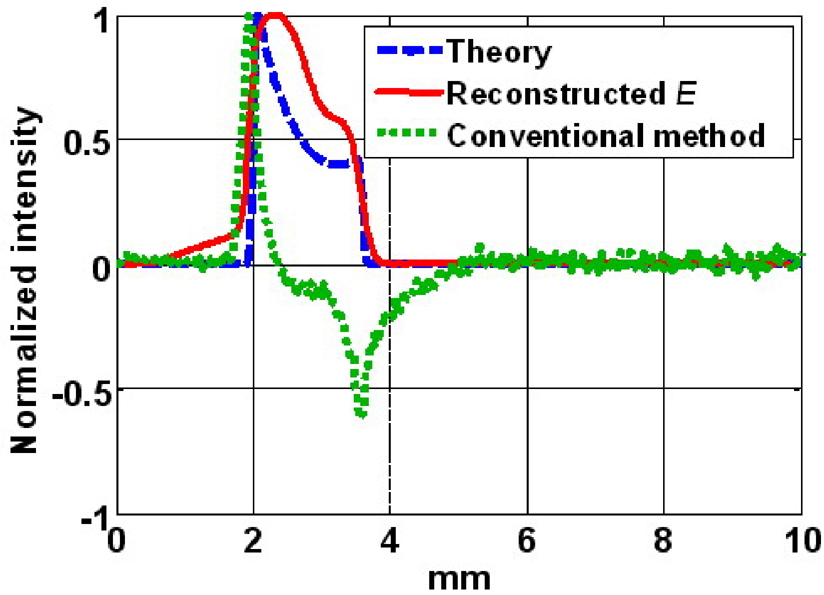

Fig. 3.4 Simulation results represented in A-lines at 10-mm scanning position, including the theoretical value (dashed), the reconstructed energy deposition (solid), and the focusing result (dotted).

Fig. 3.4 shows 1D signals at the scanning position of 10 mm. The dashed line is the predefined optical energy deposition (i.e., the theoretical profile), the dotted line and the solid line represent the reconstructed results of the conventional method and the propose algorithm, respectively. According to the diffusion approximation, the theoretical profile shows a decay that is similar to an exponential function from top (2 mm) to bottom (3.5 mm) of the sample. Using the conventional method, strong signals only exhibit at the top and bottom edges of the sample. It means that only the absorption gradient can be revealed. Details inside the sample are missing, which agree with the relation between the far field photoacoustic signal and the optical energy deposition profile [57]. By applying the proposed algorithm, the 1D result shows good agreement with the theoretical profile. It presents not only the boundaries but also the internal optical absorbing process. The resultant energy deposition can also be regarded as an evident that the phantom was irradiated from the top and decayed through the depth inside the sample.

3.3 Experimental methods

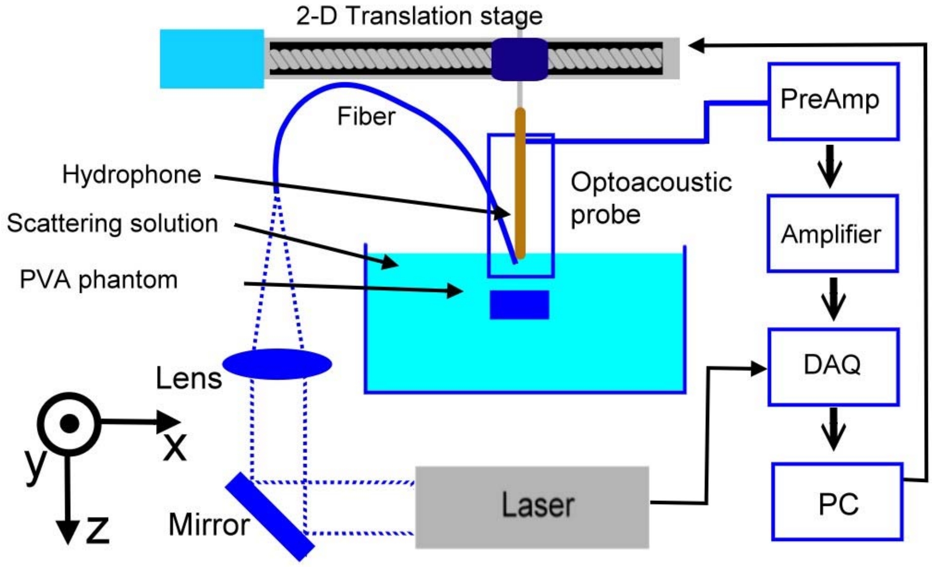

Fig. 3.5 Graphical figure of the 3D photoacoustic imaging system.

In order to further demonstrate the performance of the proposed algorithm, a 3D backward mode photoacoustic scanning system was built. Fig. 3.5 shows the graphical figure of the scanning system which mainly consists of a Q-switch Nd:YAG laser, a wideband acoustic receiving system, and a 2D precision translation stage. The Q-switch Nd:YAG laser (LS-2132U, LOTIS TII) operating at 1064 nm infrared light with a pulse duration of 8 ns was employed for optical illumination. The laser energy was focused by lenses onto a 1000-μm fiber (FT-1.0-UMT, Thorlabs) with an optical energy of 21 mJ and a 15-Hz pulse repetition rate. An ultrasonic needle hydrophone (MHA9-150, Force) PVDF hydrophone with a frequency response from 0.1 to 80 MHz was used to detect the generated photoacoustic signals. The active area of the hydrophone had a diameter of 150 μm. We incorporated the fiber and the needle hydrophone on a single holder as a photoacoustic probe. This probe was affixed on the 2D translation stage (CSR200, Control System in Motion) and mechanically scanned with a 100 μm step size. The scan range was 10 mm in both the *x* and *y* directions. A rectangular sample, which was made from a dyed polyvinyl alcohol (PVA), with a size of 2.5, 2.5, and 3.5 mm respectively in the width (*y*-direction), thickness (*z*-direction), and length (*x*-direction) was immersed in 0.1% milk aqueous solution contained in a water tank to be the target under investigation. The phantom optical absorption coefficient was 4.1 cm^{-1} and the milk solution had a scattering coefficient of 3.69 cm^{-1}, which was measured by a double integrating sphere system. This top edge of the rectangle phantom was 3 mm below the hydrophone tip. The detected photoacoustic signals were amplified by an acoustic amplifier (5800PR, Panametrics). These waveforms were digitized and stored in a personal computer with a data acquisition card (CompuScope 12100, Gage) at a 100-MHz sampling rate.

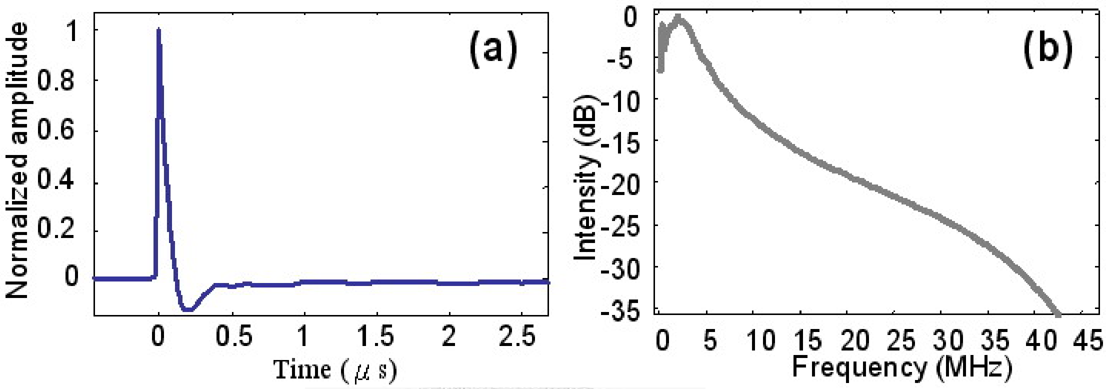

Fig. 3.6 The LIOB signal detected by the hydrophone (a), and its spectrum (b).

Although the hydrophone provides high performance in detecting wide-band photoacoustic signals, the proposed algorithm required higher sensitivities in the low frequency range in order to reduce the artifacts. Laser-induced optical breakdown (LIOB) is a useful technique to calibrate the hydrophone sensitivities especially those components near DC [61]. It instantaneously creates a single microbubble in de-ionized water by irradiating high power laser energy inside the water with a tiny focused spot. This microbubble quickly expands into the surrounding material (i.e., the water) with a velocity exceeding the speed of sound. The acoustic transient is a short and positive pressure wave. Thus, it has a wide bandwidth from DC to 10 MHz or higher frequencies (depends on the bubble size). An LIOB experiment was conducted to obtain the acoustic transient by using focused laser energy with a duration of 5 ns. The acoustic transient was detected by using the same system as the one used in photoacoustic experiments, as shown in Fig. 3.6(a). The spectrum of this acoustic transient has been shown in Fig. 3.6(b). The frequency response was calibrated by using the results of the LIOB.

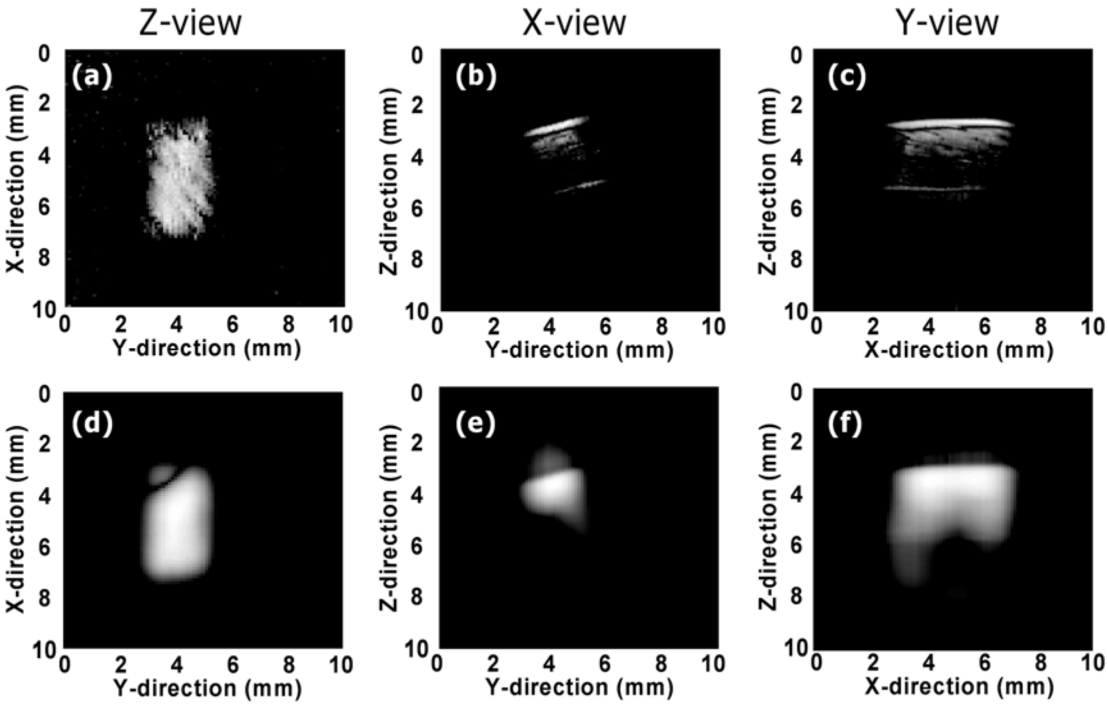

Fig. 3.7 2D cross-sectional images of the reconstruction results including *z*-view, *x*-view, and *y*-view images from left to right, respectively. (a)-(c) show the results of conventional reconstruction method and (d)-(f) show the results of the RED. The dynamic range is 30 dB. The vertical axis is the depth, and the horizontal axis is the lateral direction.

Fig. 3.7 shows the experimental results. These images are the cross-sectional images of the reconstructed object including the *z*-direction, *x*-direction, and *y*-direction views. Fig. 3.7(a)-(c) are the 2D images using the conventional method. The *z*-view image shows the top of the phantom with a rectangular shape since only the top and bottom edges can be exhibited by using conventional method (i.e., the focusing technique). Fig. 3.7(b) and (c) present the images with only two straight lines on the boundaries of the phantom and some contents between the lines that are similar to the simulation results. The results show inadequate information of optical energy deposition. The results of the RED are shown in the bottom figures (Fig. 3.7(d)-(g)). Distributions of the energy depositions are clearly presented visible. The object becomes more similar to a rectangular structure especially in the *x*-view and y-view images. The energy decay from the top to the bottom is easier to observe, which indicates that the laser energy was exposed from the top of the phantom, and decayed due to the energy absorption of the phantom.

3.4 Discussion

3.4.1 Efficacy evaluation of the RED

In previous sections, we introduced the RED and presented its ability of offering the image of the deposited energy instead of the boundaries measured from the conventional method (i.e., the focusing method). In the following, we further quantify the efficacy of the RED with more complex samples in numerical simulations. Four parameters were employed to evaluate the capability of the RED, including the sum of absolute difference (SAD), the sum of relative difference (SRD), the image correlation (IC), and the contrast-to-noise ratio (CNR). They are defined as following:

$$SAD = \sum_{r \in \Omega} \left| a(r) - b(r) \right|, \tag{3.11}$$

$$SRD = \sum_{r \in \Omega} \left| \frac{a(r) - b(r)}{a(r)} \right|, \tag{3.12}$$

$$IC = \frac{\left[\sum_{r \in \Omega} a(r) \cdot b(r) \right]^2}{\sum_{r \in \Omega} a(r)^2 \sum_{r \in \Omega} b(r)^2}, \tag{3.13}$$

$$CNR = \frac{\sum_{r \in \Omega_1} a(r) - \sum_{r \in \Omega_2} a(r)}{Noise} \tag{3.14}$$

where a and b are two images for comparison. Ω denotes the entire imaging region and r is the sampling point inside the image. The SAD is a straightforward evaluation method for the similarity between two images. In addition to the SAD, the SRD estimates the difference not only determined by the high intensity region but also the weak signal region. Therefore, the SRD can be used to enhance the differences caused by the degraded lateral resolution. The third parameter is the image correlation, which measures the correlation coefficient of these two images. The last parameter is the

CNR, which describes the contrast between two regions of interest (ROIs) in an image.

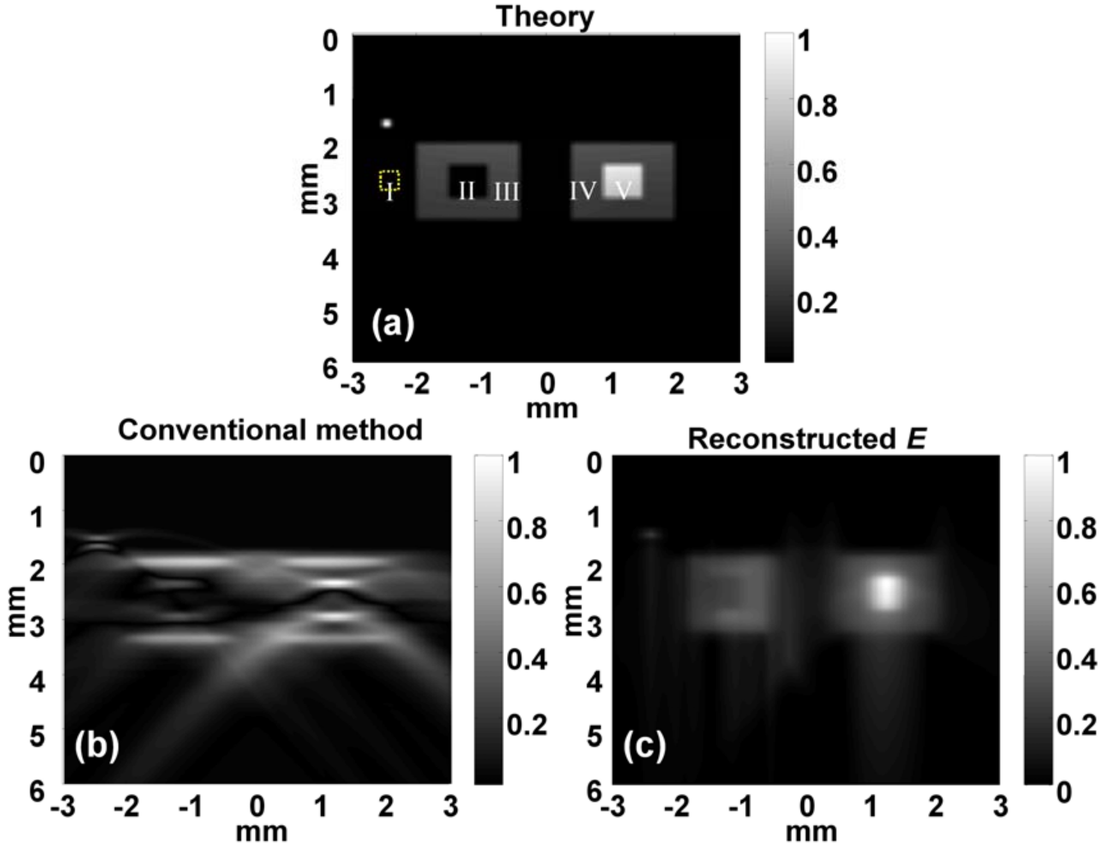

Fig. 3.8 Images of the theoretical energy deposition (a), the conventional method (b), and the reconstructed energy deposition (c). Note that five rectangular ROIs with a size of 0.2×0.2 mm^2 were chosen to measure the CNR.

Here, we extended the application of the RED to achieve the reconstruction of a complex sample. The sample contains two rectangles with a base 1.5 mm long and a height 1 mm wide. Each rectangle has an absorber 6 mm long and 4 mm wide. With various absorption coefficients, the deposited energy exhibits a variety of contrast levels. The results of the conventional method and the RED are shown in Fig. 3.8 (b) and (c), respectively. Again, the image after the RED shows a high agreement with the theoretical energy deposition. This phantom was used to evaluate the efficacy of the RED by using the SAD, SRD, IC, and CNR. Five ROIs that are indicated by Roman numerals were chosen to measure the CNR.

Table 3.1: Measured parameters from Fig. 3.8

Parameters	Theory	Conventional method	Reconstructed *E*
SAD	0	0.052	**0.017**
SRD	0	86.31	**20.26**
IC	1	0.23	**0.7**
CNR (II/I) (dB)	35.51	8.96	**46.98**
CNR (II/III) (dB)	50.11	21.95	**38.80**
CNR (V/I) (dB)	66.45	36.36	**58.59**
CNR (V/IV) (dB)	63.17	23.24	**54.86**

Note that the SAD, SRD, and IC were measured as the comparisons between the RED results and the theoretical energy deposition, and the CNRs were calculated from the ROIs indicated in Fig. 3.8(a).

Table 3.1 lists the results of these parameters. Obviously, the reconstructed energy deposition is about 3 times less difference than the results of the conventional focusing in the SAD and the SRD. The IC was improved by 3 times to 0.7 that indicates that the RED results are much similar to the theoretical profile. In addition to these parameters, the CNR enhancements of the proposed method are obviously remarkable. Due to the principle of photoacoustic propagation, the detected photoacoustic waves mainly dominated on the gradient of the absorption distribution, and hence it is difficult to exhibit the details of absorbed energy by using the conventional focusing technique. On the contrary, the results using the RED reveal a high optical contrast of the sample, as shown in Fig. 3.8(c). In this figure, the contents with a low and high deposited energy at region II and V, respectively, can be observed, and the CNRs have a great improvement in the results of the proposed method as listed in Table 3.1. This further demonstrates the efficacy of the RED.

3.4.2 Tail artifacts

In our previous study, we found that tail-liked artifacts might be brought when we tried to integrate the focused signal in the RED [62]. These artifacts was caused by the unbalance between the total intensity of the positive part and that of the negative part of the signal (i.e., the DC signals), which is frequently occurred especially in the CF weighting results. In the previous report, we used a filtered weighting map to reduce the artifacts. This problem has been solved since we found that it is more reliable if the integration is achieved by de-convoluting the differentiation of the Dirac Delta function. This method has been applied throughout this thesis.

3.5 Concluding remarks

In this research, we developed the RED to obtain the energy deposition as the previous step to reconstruct the optical absorption distribution in backward photoacoustic imaging. This algorithm was developed from the solution of the photoacoustic wave equations in combination with the SAFT-plus-CFW$_b$. Simulations and experiments were conducted to verify efficacy of this algorithm. In the simulations, the photoacoustic signals were generated based on both the diffusion approximation and the solution of the photoacoustic wave equations. In the experiments, a 3D backward mode photoacoustic imaging system was built. A phantom was used to illustrate the validity of the proposed algorithm. The results show that optical energy deposition can be efficiently reconstructed. The efficacy of the RED was further demonstrated by using the SAD, SRD, IC, and CNR. The results indicate that the RED improves the SAD, SRD, and IC by 3 times, and the CNR by 17 dB.

Chapter 4 Quantitative reconstruction of absorption coefficient

In this chapter, we further discuss the possibility in measuring the absorption coefficient by using the energy deposition measured after the RED. An efficient algorithm for quantitative reconstruction of the optical absorption distribution named the iterative recovery of absorption (IRA) is presented. This algorithm was proposed by Cox *et al.* [63, 64]. It associates with light transport model to iteratively calculate the laser fluence and the consequent deposited energy from a predicted absorption distribution. The absorption distribution can be approached by recursively updating the error estimated from the difference between the predicted and the RED results. However, the IRA requires absolute values of both the measured energy deposition and the initial laser fluence to be measured in advance. This is difficult to complete since measuring all the physical parameters involving in the photoacoustic generation is infeasible in practice.

In this study, we introduce a method to fulfill this requirement by using a strong absorber as a reference point and demonstrate that the IRA can also be performed by using an imperfect optical energy deposition result from the RED. The backward mode photoacoustic imaging becomes more quantitative as the image is directly related to the inherent properties of an image object.

4.1 Iterative recovery of absorption coefficient (IRA)

The concept of the IRA is to iteratively update an absorption distribution according to the differences between the calculated and the measured energy depositions. Although the capability of this iterative reconstruction technique has been demonstrated [63, 64], this algorithm can be performed only when the incident laser energy and absolute energy deposition are precisely estimated in advance. However, in photoacoustic imaging, it is difficult to be achieved since detecting all physical parameters involving in photoacoustic generation are not easy to be accomplished, especially in *in vivo* practice. Moreover, imaging with a small angular extent restricts the performance of the reconstructed energy deposition and further affects the results of the IRA.

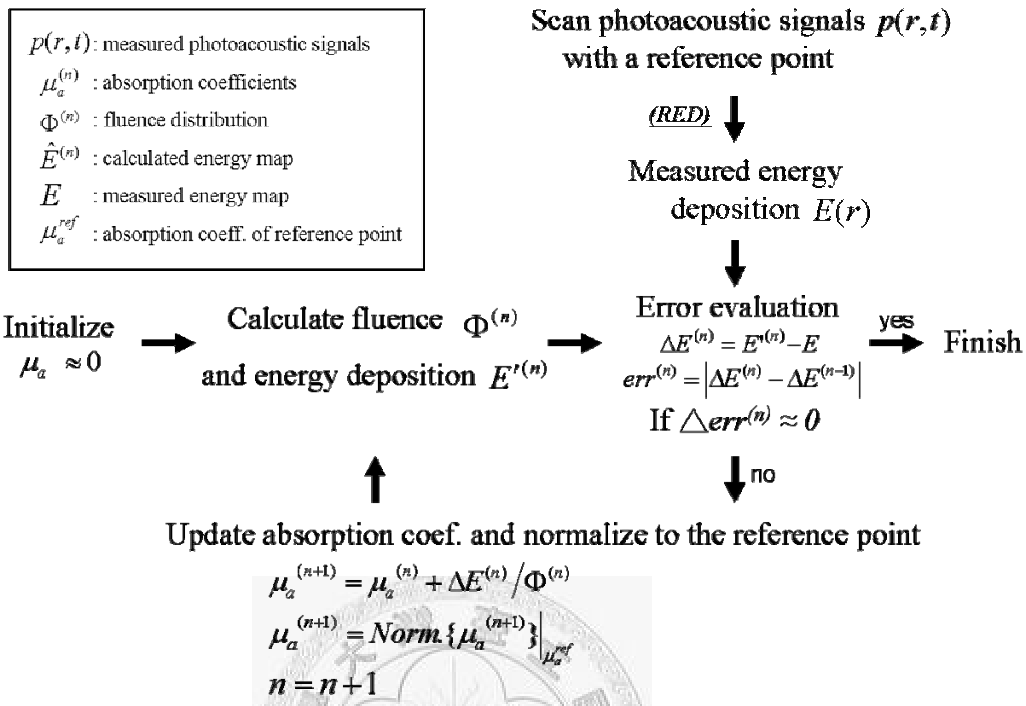

Fig. 4.1 Flowchart of the IRA with the reference point

To overcome this problem, an additional condition was conducted in our reconstruction algorithm. An absorber with a determined absorption coefficient was set as a reference point and was placed above the scanning object. It helped to take all unknown parameters into account and to govern the iteration to convergence. Therefore, the new IRA (see Fig. 4.1) as a modified approach can be implemented by the following steps:

(a) measure the absorbed energy distribution E with a predetermined reference point by using the RED described previously;

(b) set initial absorption distribution $\mu_a^{(0)}$ (a constant small value throughout the image);

(c) calculate the fluence Φ and the energy deposition E' by using the absorption distribution;

(d) update the absorption distribution based on the energy differences $\triangle E'$ and the absorption value of the reference point μ_a^{ref};

(e) continue iterations until the error, $err^{(n)}$, becomes invariant (i.e., $\triangle err^{(n)}$ approaches to zero).

In each iteration, the reference point functions as a criterion for regulating the reconstructed absorption distribution and helps to speculate the absorption distribution μ_a and its corresponding fluence Φ since both of these two unknown parameters directly determine the energy deposition, *E*.

In previous practices, we found that even though the image quality is improved by the SAFT-plus-CFW_b, the reconstructed energy deposition after the RED presents significant sidelobes and the blurred energy deposition seems to exhibit lower effects on the optical scattering. The image can be viewed as the result donated mainly from the absorption. Under this assumption, the fluence calculation in the IRA could be simplified by using the Beer-Lambert law instead of the diffusion approximation as a modified approach. Here, we employed the depth-profiling method proposed by Viator *et al.* [65]. This method considers only the fluence along the axial direction and can be expressed as:

$$\Phi(z) = \Phi_0 \cdot \exp\left[-\sum_{i=0}^{z} \mu_a(i) \cdot z \right] \tag{4.1}$$

where Φ(z) is referred to the fluence at the depth of *z*, and Φ_0 represents the incident optical energy. This equation considers only the absorption of the laser energy. The simplification of using the depth profiling helps to reduce the computational complexity and to lead the IRA to convergence.

4.2 Numerical analysis

Simulations were performed to verify the efficacy of the new IRA. The scanning structures were furnished to be the same as shown in Fig. 3.1. A sample containing with three rectangular absorbers was set to be the object of this simulation, as shown in Fig. 4.2(a). The absorption coefficients of the absorber are 20, 2.5, and 8 cm^{-1} respectively from left to right. The scattering coefficient and the anisotropy factor were set to be a constant of 50 cm^{-1} and 0.9 respectively throughout the imaging region. Sound velocity and the Grüneisen coefficient of water were chosen to be 1500 m/s and the 0.11, respectively and were applied to calculate the energy deposition [66]. By applying the diffusion model, the distributions of the propagated laser fluence and their corresponding absorbed energy were obtained. In Fig. 4.2(b), the energy deposition of each rectangle exhibits energy decay from the top, a fact that the laser irradiates at the same side as the acoustic detection. It is also obvious that the rectangle edges absorb more energy from the non-absorbing surroundings due to the optical scattering, as mentioned in Chapter 3.

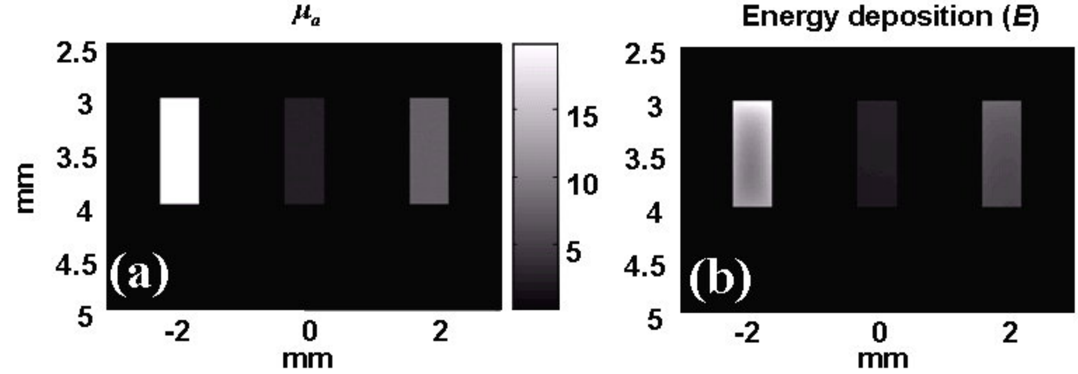

Fig. 4.2 Absorption distribution of the scannng object (a), and its corresponding energy deposition (b).

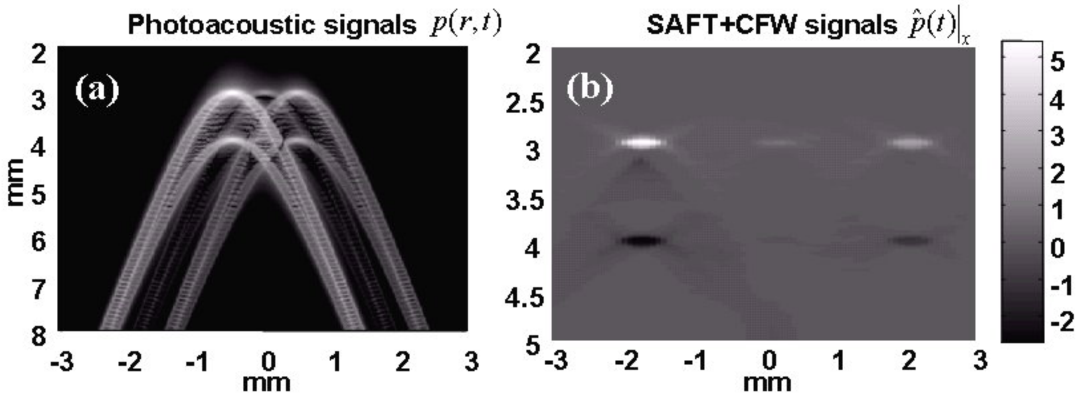

Fig. 4.3 Measured photoacoustic signals (a), and the results after focusing (b)

The resultant energy deposition was then utilized to produce the photoacoustic signals based on Eq. (1.10). The scanning step and the sampling frequency were set to be 0.08 mm and 75-MHz, respectively. The laser temporal profile was set to be a Gaussian distribution with a duration of 25 ns. Suffering from the acoustic diffraction, the signals reveal with lost absorption information on structure and intensity and cannot be distinguished (see Fig. 4.3(a)). These photoacoustic signals were then focused by using the SAFT-plus-CFW_b. Dynamic focusing with a reasonable f-number of unity was performed throughout the image for providing a high imaging quality, as shown in Fig. 4.3(b).

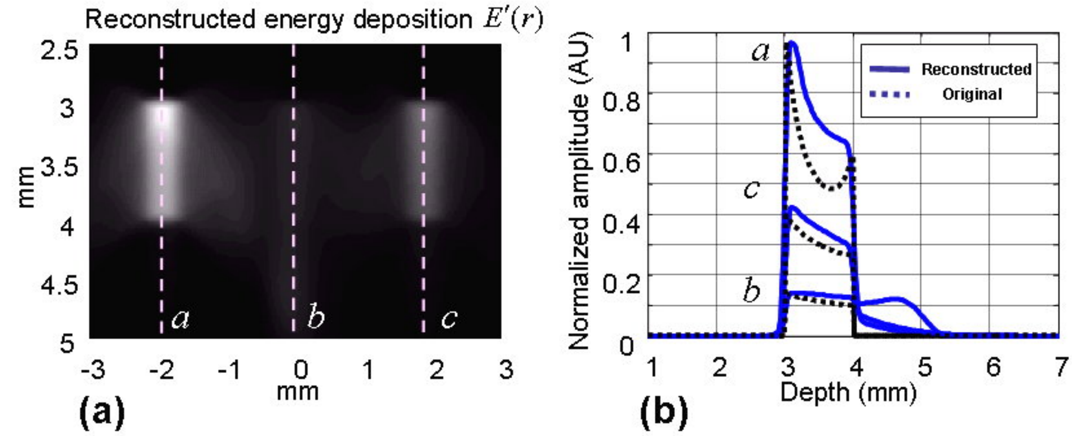

Fig. 4.4 Reconstructed energy deposition (a), and the A-lines at x = -2, 0, and 2 mm (solid) with the corresponding theoretical profiles (dashed) captured from Fig. 4.3(b).

After focusing, these photoacoustic signals were then integrated to result in the energy deposition based on Eq. (3.6) to obtain the reconstructed energy deposition as shown in Fig. 4.4(a). Comparing to the original energy deposition (see Fig. 4.2 (b)), the results suffering from the diffraction present a blurred image. However, the energy decay along the *z*-axis can still be distinguished. Fig. 4.4(b) shows the longitudinal 1D curves at the center of the reconstructed energy deposition in each rectangle. Obviously, these curves are mostly consistent in amplitude. However, all the trends of the exponential decay along the depth present a relatively low absorption than that of the theoretical profile. This reconstruction distortion occurs due to the insufficient focusing since the backward mode images in a small angular extent. Focusing quality in the backward imaging depends on the size of the synthesized aperture (i.e., f-number) as well as the signal frequency. Unfortunately, photoacoustic signals yields a wide range in frequency, and therefore, it is difficult to avoid low frequency distortion since the integration in the RED greatly gains these low frequency signals.

Although the insufficient focusing affects the reconstructed energy deposition, it is possible to achieve the IRA if the reconstructed energy deposition is treated as a result from proportionally low absorption. Therefore, in the proposed algorithm, we chose a lower value of μ_a^{ref} instead of the theoretical absorption coefficient at the reference point in the iteration. Note that even if the μ_a^{ref} is different from the theoretical absorption, determining a reference point in the iteration still helps leading the iteration to convergence. Finally, the results after the IRA were in a linear proportion with the theoretical absorption coefficient, and were normalized according to the absorption of reference point to achieve the IRA.

In this case, we set the left rectangle (i.e., strongest absorbing object) to be the reference point of this sample and performed the IRA with μ_a^{ref} ranging from 0.1 to 2 cm^{-1}. Note that the theoretical value is 20 cm^{-1}. Fig. 4.5 presents the logarithm of the iteration error $\triangle err$ in terms of the μ_a^{reff} and the times of iteration. The iteration converges when we applied a lower μ_a^{ref} than 1.6 cm^{-1}.

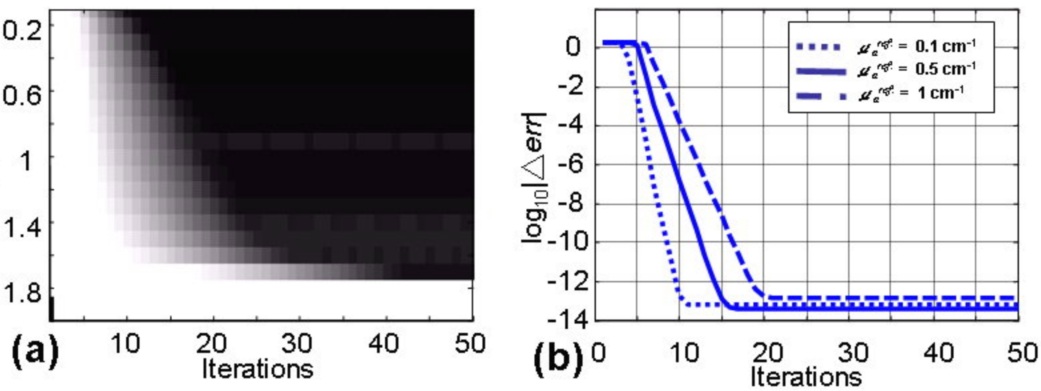

Fig. 4.5 Logarithm of the iteration error $\triangle$err in terms of the iteration times and various μ_a^{ref} ranging from 0.1 to 2 cm-1 (a), and its 1D plot at μ_a^{ref} = 0.1, 0.5, and 1 cm^{-1} corresponding to dotted, solid, and dashed lines (b).

The lowest μ_a^{ref}, presenting a minimum error in these iterations, were utilized to achieve the IRA. Fig. 4.6(a) exhibits the reconstructed absorption distribution. The reconstructed image shows a rectangle with the same size and position as the predefined phantom. The averages of the absorption in these rectangles were performed to be 18.1, 2.4, and 7.3 cm^{-1}, respectively, and the average error of these values is 7.42%. The image presents a wide lateral extend. This is also due to the insufficient focusing in low frequency. Fig. 4.6(b) and (c) shows 1D profiles in the lateral direction at the depth of 3.5 mm and in the axial direction, respectively. Apparently, the reconstructed image is similar to the theoretical profile in optical absorption, position, and geometry.

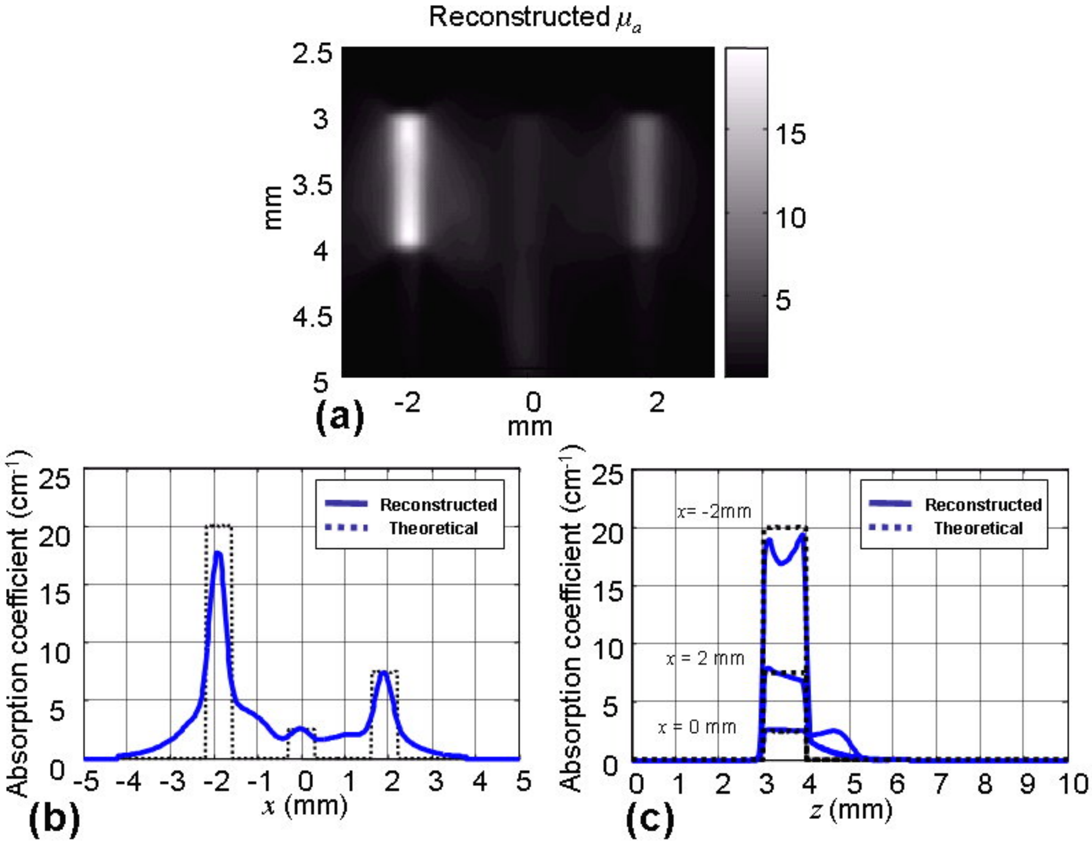

Fig. 4.6 Simulation results of the reconstructed absorption distribution (a), and its A-lines along the horizontal axis at a depth of 3 mm (b), and that along the vertical axis (c). Note that the theoretical and the reconstructed absorptions are shown in dashed and solid lines, respectively.

4.3 Phantom experiment

Phantom experiments were performed by using a built backward mode photoacoustic scanning system. This system consists of a Q-switch Nd:YAG laser, a wideband hydrophone and an acoustic receiving system, and a high precision translation stage. Fig. 4.7 illustrates the schematic diagram of the scanning system. Laser beam from the Nd:YAG laser (LS-2132U, LOTIS TII) operating at 1064 nm infrared light with a pulse duration of 10 ns was coupled onto a linear light guide (LG-L50-6-H-1500-F-1, Taiwan Fiber Optics) with a output energy of 9.8 mJ/cm^2. The fiber arrangement inside the light guide was randomized so that the output along the *x*-axis can be regarded as a homogeneous distribution. A wideband ultrasonic needle hydrophone (MHA9-150, Force technology) with an excellent frequency response ranging from 0.1 to 80 MHz was used to detect the generated photoacoustic signals. A photoacoustic probe was created by incorporating the light guide and the hydrophone, which is fixed at the middle of the light guide. This probe was affixed on a translation stage driven by a high precision ultrasonic motor (NR-8, Nanomotion) and mechanically scanned with a 0.1 mm step size. The scan range was 80 mm in the x direction. The detected photoacoustic signals were amplified by an acoustic amplifier (5073PR, GE Panametrics) and were digitized and stored in a personal computer with a data acquisition card (CompuScope 14200, Gage) at a 200-Msps sampling rate.

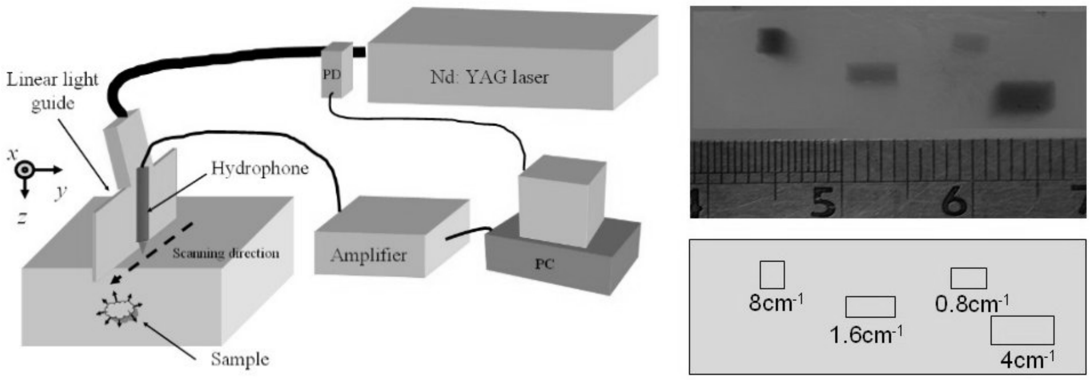

Fig. 4.7 Schematic diagram of the experiment photoacoustic system (left), and the agar phantom containing four rectangular absorbers (right). In this system, laser beam from the Nd:YAG laser was coupled onto a linear light guide with a output energy of 9.8 mJ/cm^2. The fiber arrangement inside the light guide was randomized in order to obtain a homogeneous distribution in the lateral direction. A photoacoustic probe was created by incorporating the light guide and the hydrophone, which is fixed at the middle of the light guide.

A phantom, made from agar (Agarose I, Amresco), containing with four rectangles were used as the scanning object. These rectangles were mixed with graphite power (282863, Sigma-Aldrich) to have absorption coefficients of 0.8, 1.6, 4, and 8 cm^{-1}, respectively. This phantom was immersed in deionized water contained in a water tank to be the object under investigation.

4.4 Results and discussion

The experimental results are shown in Fig. 4.8. Owing to the broad photoacoustic radiation pattern, the measured photoacoustic signals have a wide lateral extend (Fig. 4.8(a)). These signals are suitable to be focused with a large synthesized aperture (i.e., small f-number). Fig. 4.8(b) displays the focused results by using a fixed f-number of unity thought the depth. In the result, only the edges can be exhibited and contents of those rectangles are missing. The results show inadequate information of optical absorption. After the RED, the objects are more similar to a rectangular structure (see Fig. 4.8(c)). Distributions of the energy depositions are clearly presented visible. The energy decay from the top to the bottom is easier to observe. Finally, the resultant energy deposition was utilized to reconstruct the absorption distribution using the IRA in which the strongest absorber was determined as the reference point (Fig. 4.8(d)). The calculated minimum iteration error indicates that the best results can be achieved by setting the absorption of the reference point to 0.35 cm^{-1} in the IRA. However, the results show that a particular absorption area can be reconstructed only in the reference rectangle. The others exhibit a similar profile as the energy deposition. This implies that the reconstructed energy deposition is not in proportion to the reality.

This problem is more obvious when the A-lines of the reconstructed energy deposition and that of the absorption distribution are shown as a comparison (see Fig. 4.9). After the IRA, the results show mostly the same pattern as the reconstructed energy deposition. A possible reason is that the reconstructed energy deposition was distorted, and the exponential decay in these rectangles is not proportional to their corresponding absorptions. This distortion was caused by the interferences of the low frequency signal dispersion from other rectangular absorbers. This defect can also be observed in the simulation data. In which, the reconstructed energy deposition of the absorber in the middle is also interfered by other absorbers and shows a remaining tail under the object as shown in Fig. 4.6(c). In other words, when we attempt to achieve the energy deposition, it is difficult to avoid the low frequency part since the energy deposition generally has a frequency range mostly around the DC. In addition, the focusing quality depends on both the f-number and the signal frequency. It is difficult to achieve a satisfying focusing quality in such a frequency range with a limited-view. This also implies that the assumption of reducing dispersing problem to 1D line in the RED can not be fully satisfied.

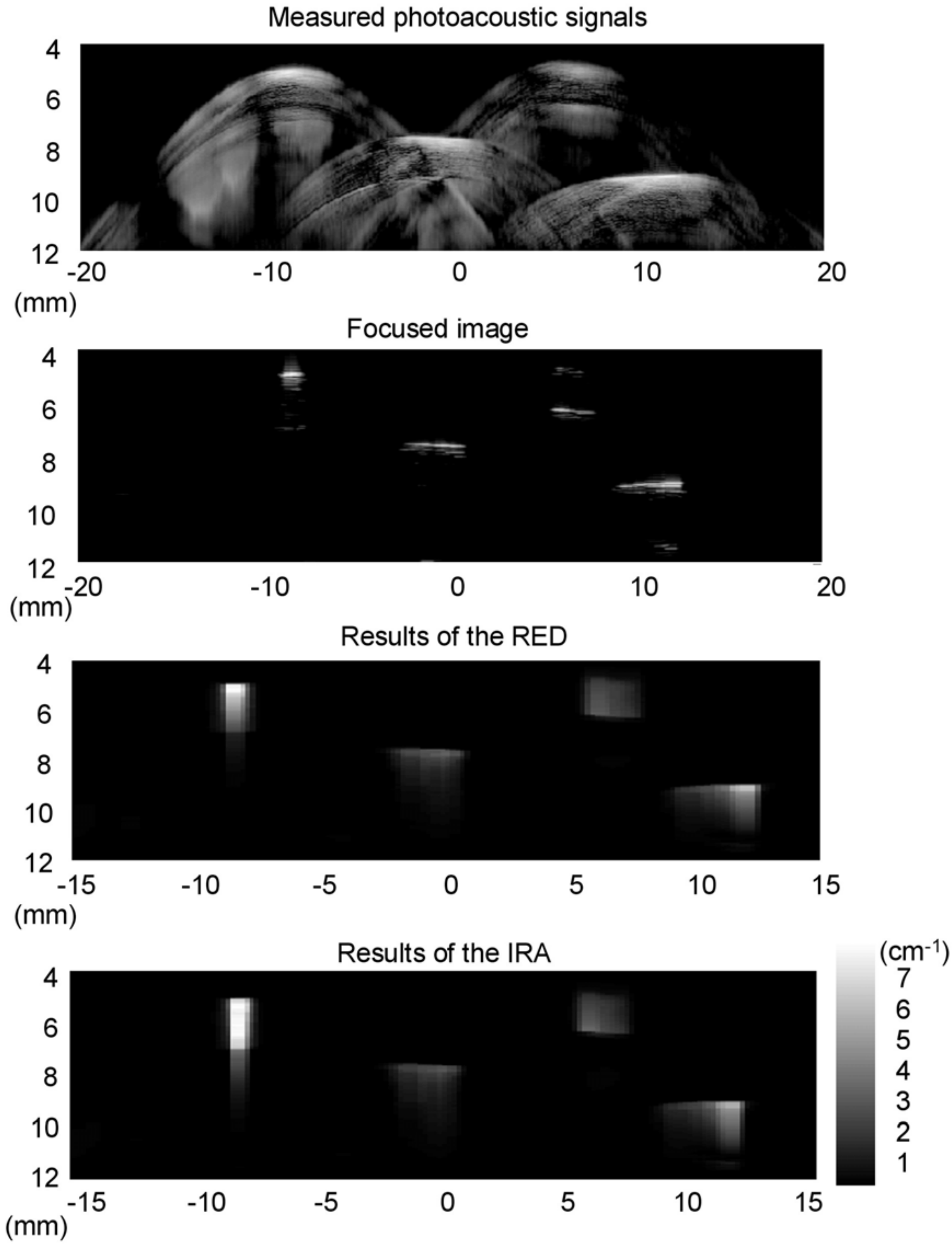

Fig. 4.8 Experimental results include the measured photoacoustic signals (a), the image focused by using SAFT-plus-CFW (b), the reconstructed energy deposition (c), and the final absorption map (d).

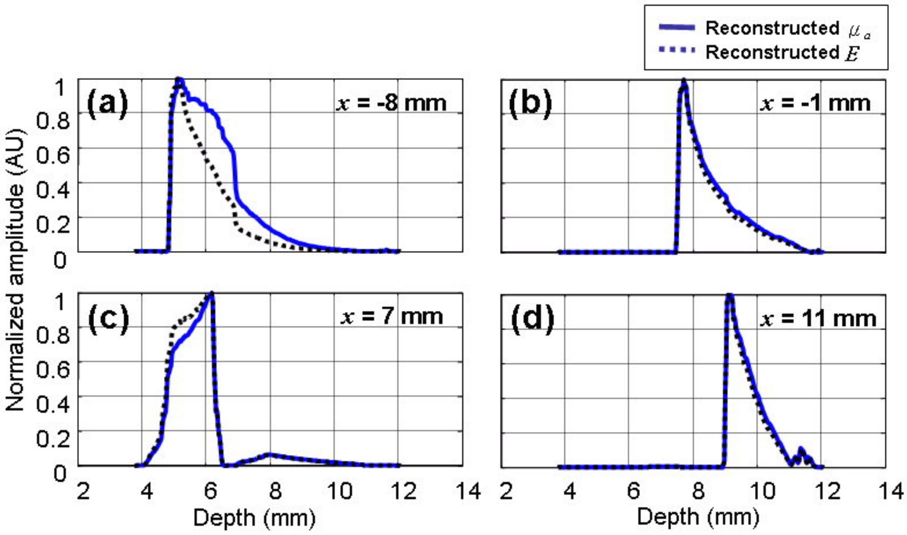

Fig. 4.9 A-lines of the reconstructed energy deposition (dashed) and the absorption distribution (solid) at x = -8(a), -1(b), 7(c), and 11 mm (d). Note that these lateral positions correspond to the absorption of 8, 1.6, 0.8, and 4 cm^{-1}.

Another possible reason is that the photoacoustic signals were not accurately measured. In the experiments, we used a wideband hydrophone to be the photoacoustic detector and calibrated the hydrophone frequency response by using the LIOB. Although the hydrophone provides an excellent bandwidth from 0.1 kHz to 80 MHz as shown in Fig. 4.10 [67], the signals around the DC cannot be accurately acquired. However, when we accomplished the RED by integrating the focused pressure waves, the signals around the DC were extremely gained in order to reveal the details of the energy deposition. Therefore, it is possible that incorrect signals were enhanced and caused the reconstruction error in practice.

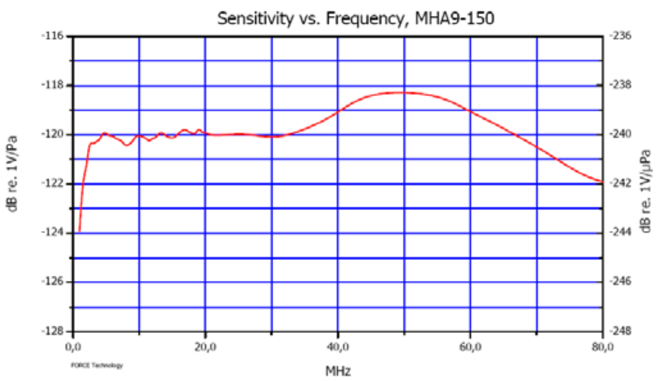

Fig. 4.10 Frequency response of the wideband hydrophone [67].

4.5 Concluding remarks

We developed a reconstruction method for the absorption distribution in backward mode photoacoustic imaging. A new IRA was proposed by using an additive reference point with a determined absorption coefficient. This reference point was used to simplify the problem and to govern the recursive calculation to convergence. We also demonstrated that the proposed algorithm effectively reconstructed the optical absorption distribution in the numerical simulations. The errors in reconstructed optical absorption coefficient are generally within 7.42%. Experiments were also performed by using the agar phantom as the scanning object. This phantom was mixed with graphite powder to have an absorption distribution. The experimental results, however, suffering from the insufficient focusing and the imperfect frequency response of the hydrophone can only present an inadequate absorption distribution.

Chapter 5 Quantitative flow measurement using a high-frame-rate photoacoustic imaging system

In this chapter, two quantitative flow measurement methods that utilize a sequence of photoacoustic images are introduced. These methods are based on the use of gold nanorods as a contrast agent for photoacoustic imaging. The peak optical absorption wavelength of a gold nanorod depends on its aspect ratio, which can be altered by laser irradiation – we established a wash-in flow estimation method of this process. The concentration of nanorods with a particular aspect ratio inside a region of interest is affected by both laser-induced shape changes and replenishment of nanorods at a rate determined by the flow velocity. In this study, the concentration was monitored using a custom-designed, high-frame-rate photoacoustic imaging system. This imaging system consists of fiber bundles for wide area laser irradiation, a laser ultrasonic transducer array, and an ultrasound front-end subsystem that allows acoustic data to be acquired simultaneously from 64 transducer elements. In the following, we introduce the flow estimation methods and the experiments in both the phantom study and the *in vitro* study.

5.1 Introduction

Blood flow in an organ or tissues through capillaries represents an important factor for diagnosing pathological conditions, including heart failure [37], liver cirrhosis [39], and pancreatitis [36], and for evaluating the physiological condition, such as in renal transplants [38]. Moreover, antiangiogenesis therapies for tumors have recently received wide attention in animal models used in preclinical research [68, 69]. Treatment effects can be evaluated by longitudinal observation of tumor angiogenesis, which can be achieved by measuring the flow in the tumor [70, 71]. The flow rate in a considerable small ROI is commonly measured by monitoring the concentrations of exogenous indicators, which is also known as the contrast-specific perfusion measurement method [72-74]. In previous articles, we have successfully developed contrast-specific methods for photoacoustic measurements of flow using gold nanorods as the contrast agent [40-43]. Although these methods have been shown to be effective, they are designed for measuring flows in large vessels, where the ROI is inside the vessel. In this paper, we extend the method to vessels smaller than the photoacoustic sample volume using a high-frame-rate photoacoustic imaging system. One major advantage of such a 2D photoacoustic flow measurement system is that it provides both anatomical and perfusion information.

Contrast-specific flow measurements have been developed using various imaging modalities, such as computed tomography [36, 39, 75], magnetic resonance imaging [76, 77], and ultrasound [78]. Contrast agents are used as flow indicators, with their dilution monitored as a function of time. In general, contrast agents are materials that are injected into the human body to enhance the SNR of blood vessels in the ROI. Although concentration is the parameter of interest, most contrast-specific methods measure the signal intensity, implicitly assuming that the intensity is linearly proportional to the concentration [77, 78]. The measured signal intensity over time is also known as the time–intensity curve (TIC). The flow rate is determined based on the indicator-dilution theory [79, 80], which typically employs a mixing chamber that relates the two TICs obtained at the inflow and outflow of the mixing chamber. The mixing chamber is often modeled as a linear and time-invariant (LTI) system, and therefore the relation between the input and output of the mixing chamber can be described by a transfer function as a wash-out analysis [81]. The transfer function is approximated as an exponential function with a time constant determined by the flow rate. Therefore, given both the input and output TICs, deconvolution can be applied to estimate the transfer function, from which the flow rate can be determined [82]. The applicability of the deconvolution-based method is determined by the validity of the LTI system model and the accuracy of deconvolution.

Wash-in flow estimation methods have been proposed that overcomes the difficulties associated with deconvolution-based methods [42, 78, 83]. This method requires the concentration of the contrast agent to be reduced by "destroying" indicators in the ROI. In ultrasonic imaging, for example, a microbubble-based contrast agent can be destroyed by irradiation with acoustic pulses of sufficient energy [83, 84], with the subsequent temporal changes in the concentration determined by the replenishment rate of the contrast agent (i.e., new microbubbles flowing into the ROI). This replenishment process is related to the local flow rate [42]. Because deconvolution is not required, the wash-in method is generally more stable and accurate.

We have previously developed wash-in flow measurements for photoacoustic imaging using gold nanorods as the photoacoustic contrast agent [40, 42]. Gold nanorods are biomedically compatible materials that offer a strong photoacoustic response in the visible-to-near-infrared region [85]. The wavelength at which a nanorod exhibits peak optical absorption is determined by its aspect ratio (defined as the length of the major axis divided by that of the minor axis). The shape of a nanorod can be altered by laser pulses with sufficient energy, which is known as the nanorod-to-nanosphere shape transition [86]. The laser-induced shape transition of gold nanorods leads to a reduction of the aspect ratio (often being transformed into nanospheres) and causes a downshift of the absorption peak. In practice the nanorods are not destroyed but instead their shapes are changed, which effectively reduces the concentration of the nanorods with the original aspect ratio, and the associated shift in the peak absorption wavelength is monitored. The wash-in flow measurements used in ultrasonic imaging is still applicable.

The ultimate purpose of this study is to extend the previously proposed method from flow estimation from a single ROI to 2D flow measurements. Achieving this requires a 2D photoacoustic imaging system with an adequate frame rate, the design and construction of which is also described in this chapter. The accuracy of flow measurements made by applying this system to flow phantoms is also reported.

5.2 Principles of photoacoustic wash-in flow measurement

According to the indicator-dilution theory, the wash-out analysis models a chamber as a LTI system and indicates that the flow rate can be estimated by solving the transfer function from the inflow and outflow of the indicators. This wash-out analysis method suffers in the accuracy of deconvolution and is difficult to be implemented since the indicator concentration before and after the chamber has to be measured. The wash-in method, on the contrary, evaluates the concentration only in a determined ROI and measures the flow rate by model fitting without using deconvolution. This method, however, requires the response of the flowing indicator to be controlled. For instance, microbubbles (i.e., as the indicators) are destroyed when we apply ultrasound waves with sufficient acoustic energy. Once the microbubble concentration drops, the refill rate can be measured to obtain the flow velocity of the fluid (i.e., the blood).

Recently, gold nanorods were demonstrated to have the same character since laser irradiation with a considerable optical energy induces the shape transition of the gold nanorods. Using gold nanorods as a contrast agent of the photoacoustic imaging to implement the wash-in flow measurement has been reported [40-43], including single-energy and dual-energy methods. In the following two sections, we introduce these two wash-in methods individually.

5.2.1 Single-energy method

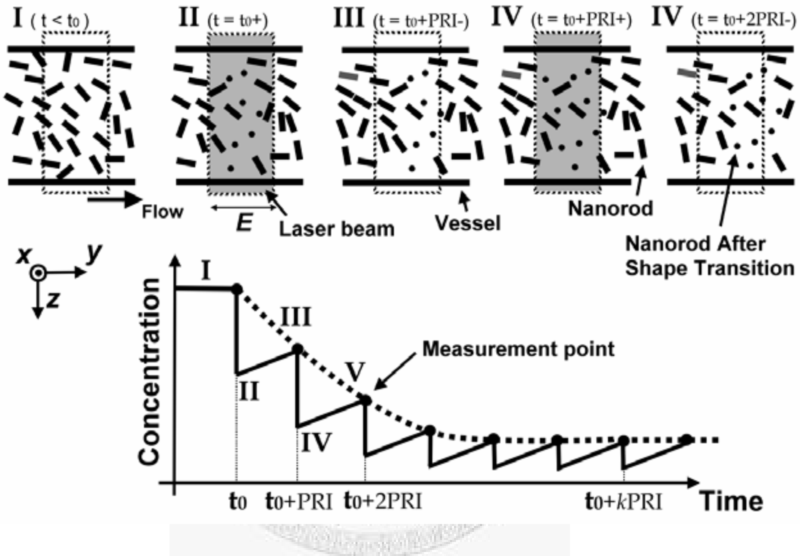

Fig. 5.1 Illustration in the single-energy wash-in process (top) and its corresponding concentration curve (bottom). After infusion, the concentration of gold nanorods reaches an equilibrium (I). The laser-induced shape transitions result in the nanorods inside the laser beam being transformed into nanosphere (or rods with a smaller aspect ratio) after each laser pulse (II and IV). New nanorods flow at a certain rate into the region without laser irradiationed (III and V).

The concept of the single-energy method is to trace and to reduce the concentration of the nanorods in a chosen ROI at the same time. In this method, considerable laser energy is used throughout the evaluation period. This method consists of both the destruction (i.e., depletion) and the replenishment (i.e., refill) of the nanorods. Laser pulses with a sufficiently high energy are used to cause rod-to-sphere shape transitions and also to monitor the reduced concentration of gold nanorods in the ROI. The process is illustrated in more detail in Fig. 5.1. A steady state is first reached before the application of laser pulses ($t<t_0$) after the injection of

the gold nanorods. A laser pulse transforms gold nanorods into nanorods with a smaller aspect ratio (possibly into nanospheres) at $t=t_{0-}$, and the detected photoacoustic-signal intensity is reduced ($t=t_{0+}$). After that, new nanorods (without shape transitions) flow into the ROI at a rate determined by the flow rate ($t_0<t<t_1$), and the concentration of gold nanorods with the original aspect ratio increases in the ROI. Another laser pulse irradiates after a pulse repetition interval (PRI) and causes another period of destruction and the following replenishment of the gold nanorods. After several periods of destruction-replenishment process, the concentration of nanorods in the ROI will reach a steady state if the number of incoming new nanorods approximates that of the destroyed nanorods.

The TIC measured in this period of time can be used to calculate the flow rate by fitting it to a curve derived from the replenishment model. The model used was adapted and modified from our previous work [42]. Assuming that the laser beam is much larger than the diameter of the capillaries inside a flow region and that the beam profile of the ultrasound transducer along the y-axis is $u(y)$, the effective concentration measured by this transducer is

$$n'(t) = \frac{\int n(y;t)u(y)\mathrm{d}y}{\int u(y)\mathrm{d}y} = \int n(y;t)\hat{u}(y)\mathrm{d}y\,, \tag{5.1}$$

where $\hat{u}(y) = u(y) \big/ \int u(y_0)\mathrm{d}y_0$, and $n(y;t)$ denotes the concentration of gold nanorods in the vessel as a function of position (y) and time (t), the initial value of which is n_0. A sequence of laser pulses with a fixed PRI is applied from $t=t_0$. To derive the model for TICs, the interlacing destruction by laser energy and replenishment of flow should be assessed respectively. The short periods between $t=(t_0+k\cdot\mathrm{PRI})^-$ and $t=(t_0+k\cdot\mathrm{PRI})^+$ (i.e., laser pulse duration) are called the destruction phases, where k is the pulse index. The replenishment phases occur between $t=(t_0+k\cdot\mathrm{PRI})^+$ and $t=[t_0+(k+1)\cdot\mathrm{PRI}]^+$ (i.e., a PRI). The superscripts + and - in the subscripts represent “soon after” and “immediately before”, respectively.

In the replenishment phase, predicting $n(y;t)$ for $t>t_0$ based on $n(y;t_0)$ is required to estimate flow parameters, for which the initial condition is $n(y;t_0)=n_0-n_0l(y)$, where $l(y)$ denotes the shape of the laser beam along the y-axis and is typically a low-pass function of y. Assuming that the flow system is linear and shift-invariant gives

$$n(y;t)=\int g\left(y-y_0;t,t_0\right)n\left(y_0;t_0\right)\mathrm{d}y_0=n_0-n_0 g\left(y;t,t_0\right)\otimes l\left(y\right) \tag{5.2}$$

where $\otimes$ denotes convolution (along y), and $g(y\text{-}y_0;t,t_0)$ (i.e., the transfer function) is the $n(y;t)$ corresponding to $n(y;t_0)=\delta(y\text{-}y_0)$, where $\delta(y)$ is the Dirac delta function. From Eqs. (5.1) and (5.2) we can obtain

$$n'(t)=n_0\left\{1-h\left[v(t-t_0)\right]\right\} \tag{5.3}$$

where

$$h\left[v(t-t_0)\right]=\int\left[g(y;t,t_0)\otimes l(y)\right]u'(y)\mathrm{d}y\,. \tag{5.4}$$

According to the random-walk model [87], the density of label (i.e., nanoparticles) along the flow direction x after a bolus injection can be represented as $F(x,\sigma)=(1/\sigma\sqrt{2\pi})e^{-(x-\bar{x})^2/2\sigma^2}$, where σ and $\bar{x}$ denote the random variable and the distance after the injection, respectively. In this case, the bolus injection – which is produced by the rapid laser destruction – is determined at t=t_0, and $\sigma=\sqrt{2D(t-t_0)}$ at the central position of $\bar{x}=v(t-t_0)$. Therefore,

$$g(y-y_0;t,t_0)=\frac{1}{\sqrt{4\pi D\left(t-t_0\right)}}\exp\left\{-\frac{\left[y-y_0-v\left(t-t_0\right)\right]^2}{4D\left(t-t_0\right)}\right\} \tag{5.5}$$

where D is the dispersion coefficient representing the randomness [87, 88]. Assuming that both the laser and the ultrasound beam profile are Gaussian distributed in y (i.e., $u'(y)=\exp\left(-y^2/\sigma_u^2\right)\Big/\sqrt{\pi\sigma_u^2}$ and $l(y)=l_0\exp\left(-y^2/\sigma_l^2\right)\Big/\sqrt{\pi\sigma_l^2}$, where σ_u and σ_l are standard deviations of the ultrasound and the laser beam profile, respectively), Eq. (5.4) can be solved as

$$h\left[v(t-t_0)\right]=\frac{l_0}{\sqrt{\pi\left[4D\left(t-t_0\right)+\sigma_u^2+\sigma_l^2\right]}}\exp\left\{-\frac{\left[v\left(t-t_0\right)^2\right]}{4D\left(t-t_0\right)+\sigma_u^2+\sigma_l^2}\right\}. \tag{5.6}$$

A reasonable approach to curve fit $h[v(t-t_0)]$ is to use

$$\hat{h}(k) = h(0)\exp(-\lambda k) \tag{5.7}$$

where λ is a model parameter, and k is the variable in the fitted curve. It represents the distance after a period of time (t-t_0). Under this condition, Eq. (5.3) can be rewritten as

$$n'(t) \cong n_0\left\{1 - c\exp\left[-\lambda v\left(t-t_0\right)\right]\right\} = n_0\left\{1 - c\exp\left[-\beta\left(t-t_0\right)\right]\right\} \tag{5.8}$$

where c and β are model parameters, and β is proportional to the flow rate, v. This equation describes the concentration change as a function of time in the replenishment phase. Therefore, the effects of the replenishment phases between each laser pulse firing can be estimated according to (8),

$$1 - n'(t-t_0)\big|_{t=\left(t_0+k\cdot\mathrm{PRI}\right)^+} / n_0 \cong c\exp\left[-\beta\left(t-t_0\right)\right]\Big|_{t=\left(t_0+k\cdot\mathrm{PRI}\right)^+}, \tag{5.9}$$

$$1 - n'(t-t_0)\big|_{t=\left[t_0+(k+1)\cdot\mathrm{PRI}\right]^-} / n_0 \cong c\exp\left[-\beta\left(t-t_0\right)\right]\Big|_{t=\left[t_0+(k+1)\cdot\mathrm{PRI}\right]^-}. \tag{5.10}$$

The concentration of gold nanorods in the replenishment phase can be described as:

$$1 - n'(t-t_0)\big|_{t=\left[t_0+(k+1)\cdot\mathrm{PRI}\right]^-} / n_0 \cong \exp(-\beta\cdot\mathrm{PRI})\left[1 - n'(t-t_0)\big|_{t=\left(t_0+k\cdot\mathrm{PRI}\right)^+} / n_0\right]. \tag{5.11}$$

On the other hand, in the destruction phases, it is noticeable that the replenishment during the destruction phase is negligible because the pulse duration is on the order of nanoseconds and is much smaller than the length of the PRI. In these periods destruction mainly dominate the behavior of the concentration of nanorods. The concentration decreases asymptotically to a constant level and can be expressed as:

$$n'(t-t_0)\big|_{t=\left(t_0+k\cdot\mathrm{PRI}\right)^-} \cong \left(n_0 - n_\infty\right)r^k + n_\infty \quad \text{for} \quad k = 0,1,2,\ldots \tag{5.12}$$

where $r < 1$ is the survival rate, which indicates the remained nanorods after one laser pulse. n_∞ is the baseline concentration. And the concentration of the gold nanorods after each laser pulse can be expressed as:

$$n'(t-t_0)\big|_{t=(t_0+k\cdot\mathrm{PRI})^+} \cong r\, n'(t-t_0)\big|_{t=(t_0+k\cdot\mathrm{PRI})^-} . \tag{5.13}$$

Finally, we can obtain the concentration of the nanorods by combining destruction phase (13) with replenishment phase (11):

$$1-n'(t-t_0)\big|_{t=[t_0+(k+1)\cdot\mathrm{PRI}]^-}/n_0 \cong \exp(-\beta\cdot\mathrm{PRI})\left[1-r\,n'(t-t_0)\big|_{t=(t_0+k\cdot\mathrm{PRI})^-}/n_0\right]. \tag{5.14}$$

Let $n''(k)=n'(t-t_0)\big|_{t=(t_0+k\cdot\mathrm{PRI})^-}/n_0$, we can have

$$n''(k+1)=1-\left[1-rn''(k)\right]s \tag{5.15}$$

where $s=\exp(-\beta\cdot\mathrm{PRI})$, and solving (15) with $n''(0)=1$ leads to

$$n''(k)=\left(\frac{1-s}{1-rs}\right)+\left[1-\left(\frac{1-s}{1-rs}\right)\right](rs)^k . \tag{5.16}$$

Equation (5.16) indicates that the concentration of gold nanorods decreases exponentially to a constant value determined by the flow velocity and the laser pulse energy. Let $n''_\infty=\dfrac{1-s}{1-rs}$ and $w=rs$ we can obtain a fitting model for the measured TIC:

$$n''(k)=n''_\infty+(1-n''_\infty)w^k . \tag{5.17}$$

Finally, the mean velocity can be obtained from the value of the fitted parameter:

$$\beta=v\cdot\lambda=-\log\left[1-(1-w)n''_\infty\right]/PRI . \tag{5.18}$$

According to Wei et al. [78], λ is inversely proportional to the width of the detection region (i.e., the width of laser beam $E=1/\lambda$). Therefore, the flow rate can be calculated from the fitted parameter according to

$$v = \beta \cdot E \, . \tag{5.19}$$

The above equations present the model of the nanorods concentration in the single-energy method and the relation between the model and the flow rate. Based on this model, the measured concentration changes in a period of time should be fitted by using Eq. (5.17) to result in fitting parameters, n''_∞ and w. After that, the flow velocity can be estimated according to Eq. (5.18) and (5.19) with a determined laser beam width E.

5.2.2 Dual-energy method

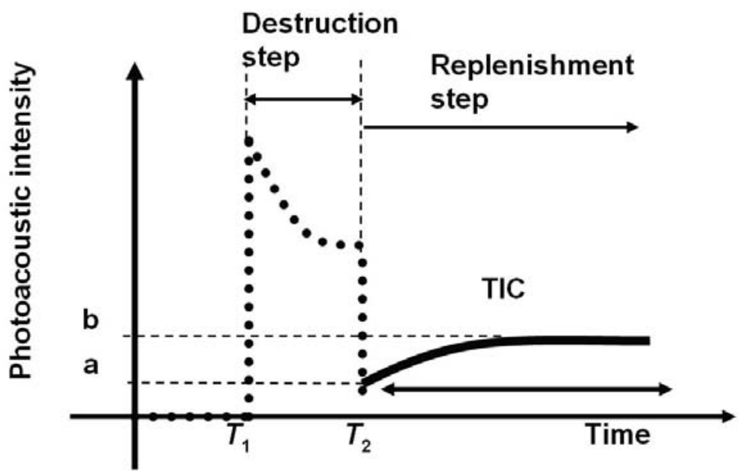

Fig. 5.2 Illustration of the destruction–replenishment flow estimation method. In the destruction phase (from T1 to T2), high-energy laser pulses are used to induce shape transitions of the nanorods, which decreases the intensity of the photoacoustic signals. In the replenishment phase (after T2), laser pulses of lower energy are used to monitor the photoacoustic signals in the same region in which the photoacoustic-signal intensity increased due to the inflow of nanorods.

In addition to the single-energy method, the flow rate estimation can also be achieved by applying two laser energies sequentially. Comparing with the single-energy method, the dual-energy method observes only the concentration in the replenishment period following the destruction step. The concept of the measured photoacoustic intensity (corresponding to the concentration of nanorods) is shown in Fig. 5.2. In the first phase, laser pulses with a sufficiently high energy are used to cause rod-to-sphere shape transitions, which effectively reduce the concentration of gold nanorods in the ROI. In the second phase, the variation in the nanorod concentration as new nanorods flow in the ROI is monitored using laser pulses with an energy that is too low to induce further shape transitions. Fig. 5.2 illustrates the procedure used to measure the photoacoustic TIC. The concentration of nanorods in the ROI will reach a steady state if the nanorods flow at a constant speed and are evenly distributed throughout the circulation system. In the destruction phase (from T_1 to T_2), several consecutive high-energy laser pulses are used to induce shape transitions of the gold nanorods and thereby reduce the intensity of the photoacoustic signal in the ROI. The concentration of gold nanorods decreases to another steady-state value at which the number of incoming new nanorods approximates that of the destroyed nanorods (at $t = T_2$). In the replenishment phase (after T_2), laser pulses of lower energy are used to monitor the photoacoustic signals in the same ROI.

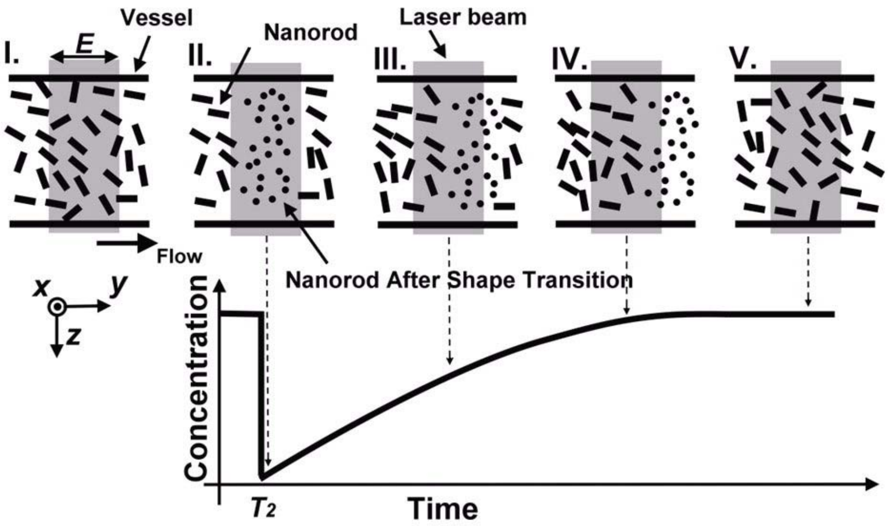

Fig. 5.3 Illustration in the replenishment phase (top) and its corresponding concentration curve (bottom). After infusion, the concentration of gold nanorods reaches an equilibrium (I). The laser-induced shape transitions result in most of the nanorods inside the laser beam being transformed into nanosphere (or rods with a smaller aspect ratio) at t = T2 (II). New nanorods flow at a certain rate into the region irradiated by the laser beam (III and IV), with the nanorod concentration eventually returning to baseline (V).

Five phases of the process are illustrated in more detail in Fig. 5.3. A steady state is first reached before the application of high-energy pulses (Phase I). The high-energy pulses transform gold nanorods into nanorods with a smaller aspect ratio (possibly into nanospheres), and the detected photoacoustic-signal intensity reaches a minimum (Phase II). The high-energy laser pulses are replaced with low-energy pulses, and new nanorods flow into the ROI (without shape transitions) at a rate determined by the perfusion rate (Phases III to IV). After a certain time (depending on the perfusion rate), the concentration of gold nanorods with the original aspect ratio increases back to the original concentration (Phase V).

Because the concentration measured after T_2 presents the replenishment of the nanorods without causing any damage, the fitting model for dual-energy method is considered to take only the replenishment part into account. Therefore, the flow rate is estimated by fitting this TIC based on Eq. (5.8), which represents the increasing concentration as a function of time and flow rate. Assuming that the photoacoustic-signal intensity is proportional to the concentration of gold nanorods, the intensity of the received photoacoustic signal can be derived as

$$I(t) \cong b\left\{1-c\exp\left[-\beta(t-t_0)\right]\right\} \tag{5.20}$$

where b is the photoacoustic-signal intensity in the steady state. According to this equation, the photoacoustic-signal intensity ranges from b-bc to b, and can be rewritten as

$$I(t) \cong a+(b-a)(1-e^{-\beta t}) \tag{5.21}$$

where a=b-bc is the offset intensity that takes into account noise and the photoacoustic signals from stationary tissue. This equation describes the measured photoacoustic-signal intensities resulting from the combined contributions of all nanorods and the stationary tissue in the ROI at each time point in the replenishment phase.

In addition to the TIC, the integrated TIC (ITIC) has been employed to estimate the flow velocity so as to effectively increase the SNR [83]. Assuming that a is equal to zero, the ITIC can be expressed as

$$ITIC(t) = \int_0^t I(\tau)d\tau = \frac{b}{\beta}(e^{-\beta t} - 1) + bt\,. \tag{5.22}$$

Curve fitting using this equation will yield the parameters from the measured ITICs. Consequently, the mean velocity can be obtained from the value of the fitted parameter, β.

5.3 High-frame-rate photoacoustic imaging system

As described in Section 5.2, the implement of wash-in methods requires the photoacoustic signal to be captured with a considerable PRI. A short PRI stands for the ability of observing fast-moving objects. During the replenishment period, absorption changes have to be measured over a short time interval (i.e., requiring a high sampling rate). In the previous works, it has been demonstrated that a sampling rate of 15 Hz allows flow velocities from 0.35 to 2.8 mm/s to be measured in a single sample volume [40].

In this study, we built up a 2D photoacoustic imaging system with a frame rate up to 15 Hz. This system employs an array transducer instead of a single-crystal transducer so as to increase the frame rate by allowing data to be acquired simultaneously from multiple channels. This high-frame-rate photoacoustic imaging system consisted of a fiber laser system, an ultrasonic digital phased array system (DiPhAS) that is often used in research applications, and a custom-design photoacoustic probe, as shown in Fig. 5.4. A Q-switched Nd:YAG laser (LS-2132U, Lotis TII) operating at 1064 nm with a pulse duration of 8 ns was used for laser irradiation. The 5-mm-diameter beam from this laser was split and guided onto two multimode fiber light guides (LG-L30-6-H-1500-F-1, Taiwan Fiber Optics) using a half-reflectance beam splitter (BS1-1064-50, CVI). The output beams from the light guides were then focused by two cylindrical lenses positioned 25 mm from the light-guide surfaces, resulting in two irradiated zones of 30×0.8 mm. Both the light guides and the focusing lenses were mounted on a custom-design holder as part of the photoacoustic probe for confocal alignment. A motorized lens wheel (FW102, Thorlabs) placed between the laser and the beam splitter was used to switch the laser energy.

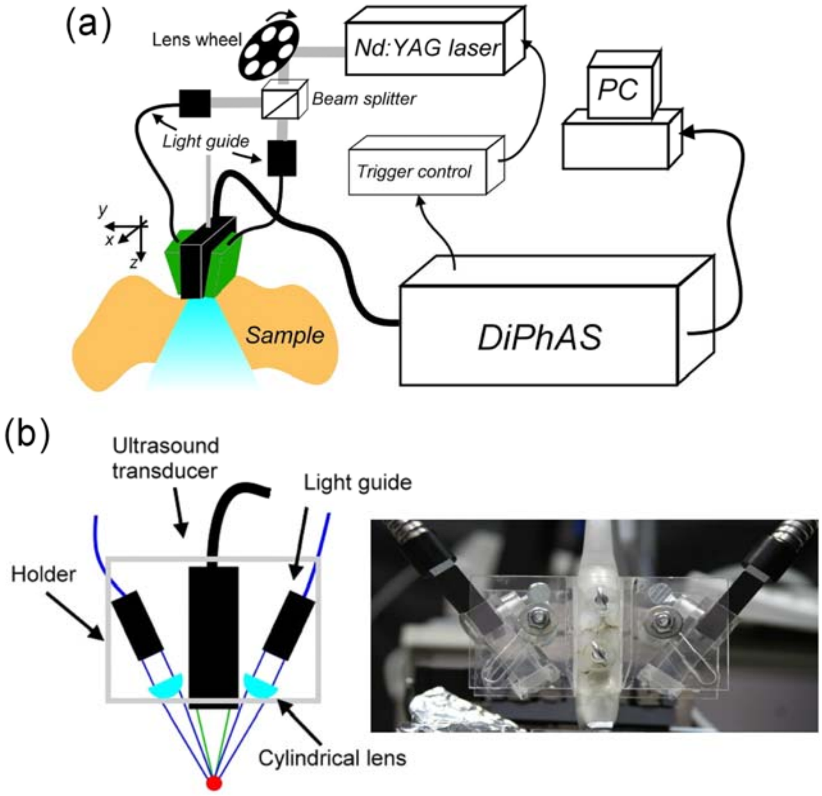

Fig. 5.4 (a) Schematic of the high-frame-rate photoacoustic imaging system that includes a fiber laser system, a DiPhAS, and custom-made photoacoustic probe. (b) Custom-made photoacoustic probe. The output beams from the light guides are focused by two cylindrical lenses positioned 25 mm from the light-guide surfaces. The focused laser beam and the ultrasound detection area are aligned confocally.

Acoustic waves induced in the irradiated volume were detected by a 128-channel ultrasonic linear array (L6, Sound Technology, PA) that was also confocally mounted between the two light guides in the photoacoustic probe, as shown in Fig. 5.4(b). The transducer elements had a pitch of 0.3 mm, a 5-mm elevational width, and a center frequency of 5 MHz with an 82% bandwidth. Reflecting foil (Ho Yan Tape, Taiwan) with a thickness of 9 μm was attached to the surface of the transducer in order to block backscattered laser irradiation from reaching the transducer surface. The DiPhAS was employed to amplify and digitize the detected RF array signals. It contained 64 transmitting and receiving channels and high-speed multiplexers to allow the use of a transducer array with up to 192 channels, although in this study the multiplexers were not used. The RF signals from the 64 transducer elements sent to the receiver were amplified by up to 80 dB and then digitized by analog-to-digital converters with 12-bit precision. The data were sampled at 40 Msamples/s, and the on-board memory allowed 512 data samples per channel to be stored before they were transferred to a personal computer (PC). The DiPhAS allowed array data from 64 channels to be simultaneously acquired and transferred every 4 ms, giving a frame rate of up to 250 Hz. The raw RF data were transferred through a high speed digital I/Q card (PCI-7300A, ADlink, Taiwan) to the PC, and dynamic focusing and image reconstruction were performed off-line. The DiPhAS and laser were synchronized using a programmable logic device (EPM3064A, Altera, CA), with the laser triggered by the DiPhAS. The actual frame rate of the system was limited to 15 Hz due to the maximum PRF of the laser that we used.

In this study, 2D photoacoustic images captured from the same flow region over the replenishment period were used to evaluate the concentration change of gold nanorods. ROIs were chosen to include the flow area of interest, such as capillaries or organs. The mean photoacoustic intensities in these ROIs were calculated at each time step as a data point in the TIC. Therefore, there is a trade-off between the SNR and the size of the ROI (which determines the spatial resolution).

5.4 Phantom study (Dual-energy flow measurement)

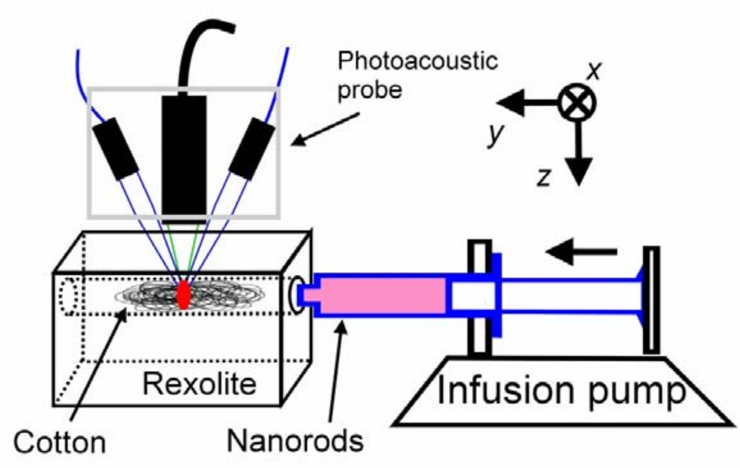

Fig. 5.5 Experimental setup of the perfusion phantom, in which the perfusion rate was controlled by the infusion pump with a syringe. Cotton was placed inside the Rexolite tube to simulate tissue microcirculation.25 The flow velocities ranged from 0.25 to 3 mm/s.

Fig. 5.5 shows a schematic diagram of the flow measurement setup. A perfusion phantom was constructed from a plastic material (Rexolite 1422, San Diego Plastics, CA) that is transparent both optically and acoustically, in which the sound velocity is

2320 m/s. It was machined to a block of size 3.5 × 4.5 × 5.5 cm^3 containing an inner tube with a diameter of 3.5 mm. A small piece of cotton was placed inside this tube so as to randomize the flow velocity, thereby mimicking tissue microcirculation [83]. A volume of 5 ml of gold nanorods with an absorption peak at 985 nm were injected at a concentration of 0.3 nM into the tube with a 10-ml standard syringe. The absorption peak was measured using a spectrophotometer (V-570, Jasco, Japan). The syringe was controlled by an infusion pump (KDS 100, Montreal, Canada) to create mean flow velocities ranging from 0.25 to 3 mm/s. The photoacoustic probe was positioned 6 mm above the tube, and cross-sectional images were captured.

In the experiments, the destruction pulses were first applied for 7 s to allow the concentration of shape-changed nanorods to approach equilibrium inside the irradiated region. The laser energy was then immediately reduced to that for the replenishment mode in order to monitor replenishment of the gold nanorods. The replenishment images were captured for 5 to 20 s depending on the time required to reach the new steady state (i.e., the speed of replenishment). Photoacoustic intensities from within a 3 × 3-mm ROI (40 × 10 pixels in the *z*- and *x*-axes, respectively) were summed at each time point to create TICs.

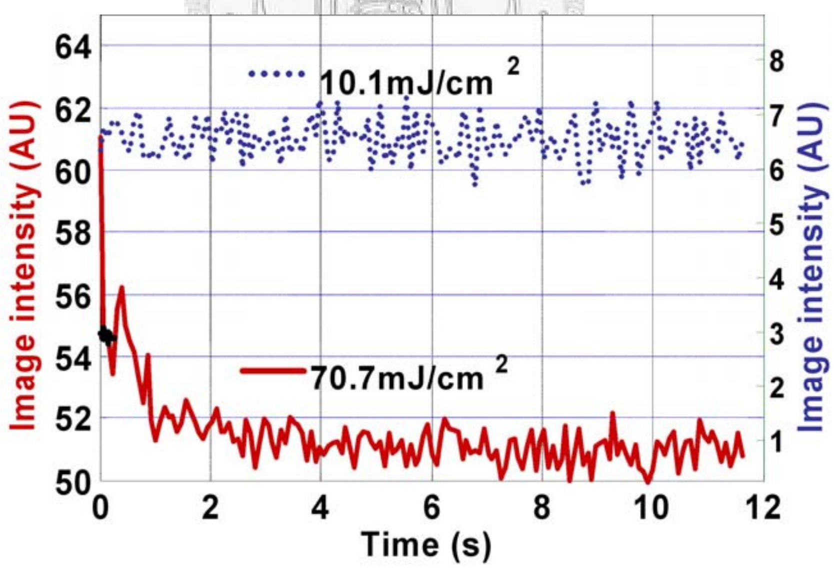

Fig. 5.6 Image intensities measured with the destruction pulses (70.7 mJ/cm2, black line; left y-axis) and the replenishment pulses (10.1 mJ/cm2, gray line; right y-axis). The intensity rapidly decayed in the destruction mode, from 61 to 52 within 2 s, whereas the intensity was relatively constant in the replenishment mode due to the nanorod concentration remain unchanged.

A pilot experiment indicated that applying laser irradiation at energy densities of

70.7 and 10.1 mJ/cm^2 was suitable for the destruction and replenishment modes, respectively. Fig. 5.6 shows that the image intensity decayed rapidly (within 2 s) for an energy of 70.7 mJ/cm^2, whereas laser energy at 10.1 mJ/cm^2 resulted in a relatively constant image intensity. Fig. 5.7(a) shows the visible-to-infrared spectra of the nanorods before and after the applications of the destruction pulses as measured using the spectrophotometer, with the gray rectangle highlighting the large absorbance difference at 1064 nm (the wavelength of the laser irradiation). The linearity of the relation between the concentration of the nanorods and the photoacoustic intensities has been proposed in literature [41] as shown in Fig. 5.7(b).

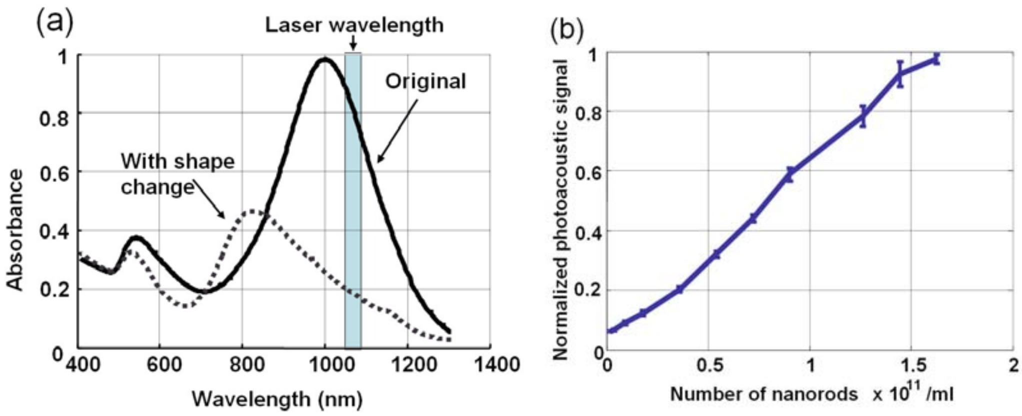

Fig. 5.7 Spectra of nanorods before (solid line) and after (dashed line) the laser-induced shape transition (a). The gray rectangle indicates the wavelength of the laser irradiation (around 1064 nm). And the measured photoacoustic intensity as a function of nanorod concentration for a laser energy of 6.45 mJ/cm^2 (b) [41].

Fig. 5.8 shows cross-sectional images of the perfusion phantom obtained at the flow rate of 1 mm/s from t = 0 to 13.2 s. These images display a depth of 7.5 mm and a width of 11 mm. The difference in sound velocity between Rexolite (2320 m/s) and water (1480 m/s) was also considered in calculating focusing delays, as was refraction at the Rexolite–water interface. Inside the tube, a random pattern is observed with decaying intensity along the depth direction, which is attributable to absorption of the laser energy by the inserted cotton.

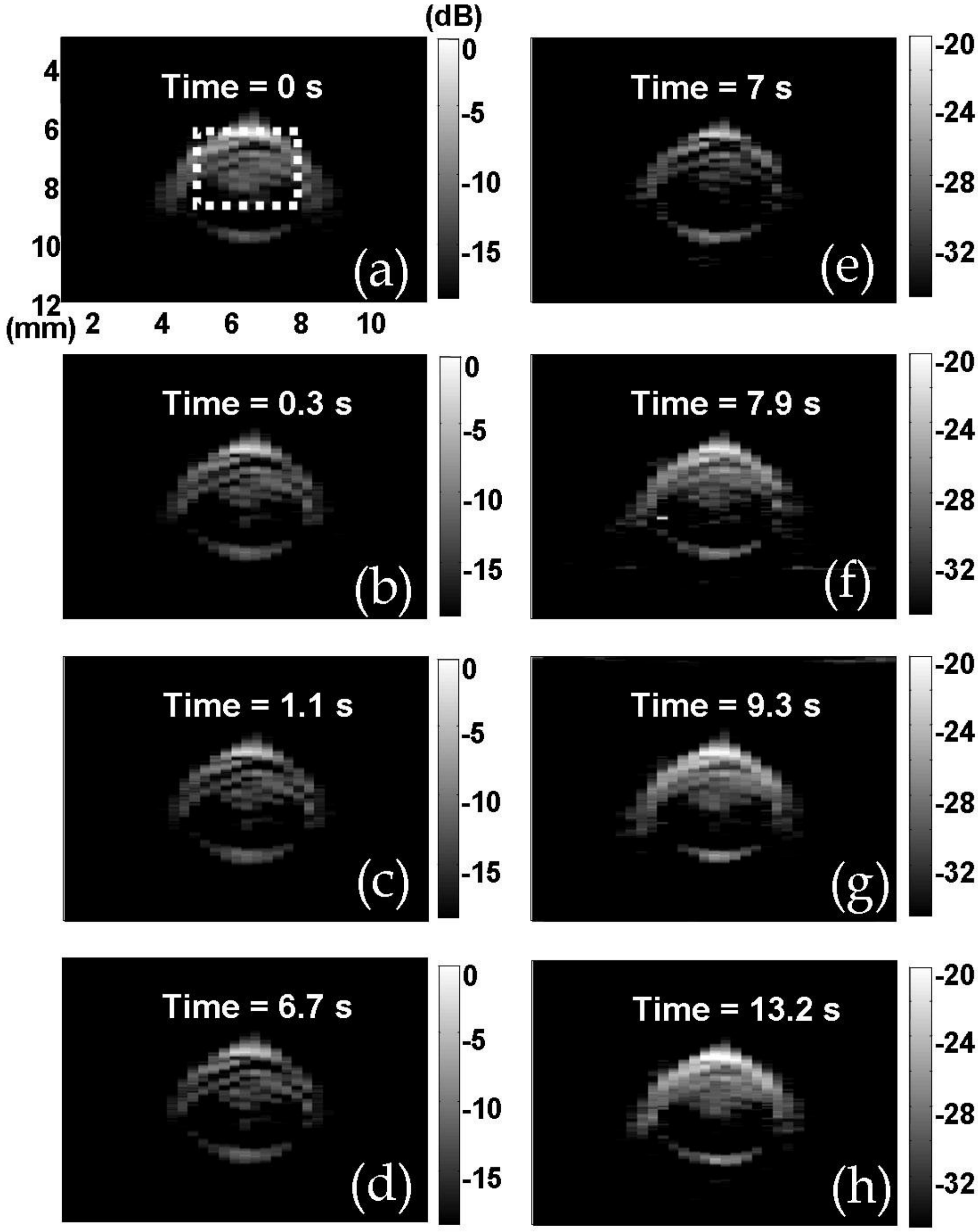

Fig. 5.8 Images captured at different times at a flow rate of 1 mm/s during the destruction (a–d) and replenishment (e–h) phases. The displayed dynamic range is 20 dB (from –20 to 0 dB) and 15 dB (from –35 to –20 dB) in the destruction and replenishment phases, respectively.

The laser energy was initially set at 70.7 mJ/cm^2 (i.e., at t = 0 s). Images captured during the destruction phase (t = 0–7 s) are shown in Fig. 5.8(a)–(d), displayed with a dynamic range of 20 dB (from –20 to 0 dB). It is clear that the image intensity decreases with time, indicating that the gold nanorods inside the tube underwent shape changes due to the strong incident laser energy that reduced the optical absorption at the laser wavelength. A steady state was reached after continuous laser irradiation at the same energy level for 7 s, at which point the number of nanorods that underwent shape transition was roughly the same as the number of new nanorods flowing into the ROI. The laser energy was then reduced to the replenishment mode (10.1 mJ/cm^2) at t = 7 s, and Fig. 5.8(e)–(h) show the images captured at t = 7, 7.9, 9.3, and 13.2 s, respectively, displayed with a dynamic range of 15 dB (from –35 to –20 dB). A smaller dynamic range was used to increase the image brightness. The lower laser energy resulted in no shape transition of the gold nanorods, and hence the new nanorods flowing into the ROI increased the image intensity. A square region with a size of 3 × 3 mm was selected as the ROI, as indicated by the dashed box in Fig. 5.8(a). The mean image intensities within the ROI were summed to create the TIC, as shown in Fig. 5.9, in which the three phases of destruction, replenishment, and plateau are clearly evident. In the replenishment phase, the concentration of new nanorods increased exponentially with time, reaching a steady state after t = 13 s. Fig. 5.10 shows the normalized TICs measured at flow rates of 0.5, 1, 1.5, and 3 mm/s, which clearly indicates that the replenishment rate of the nanorods increases with the flow rate, as described by Eq. (5.18).

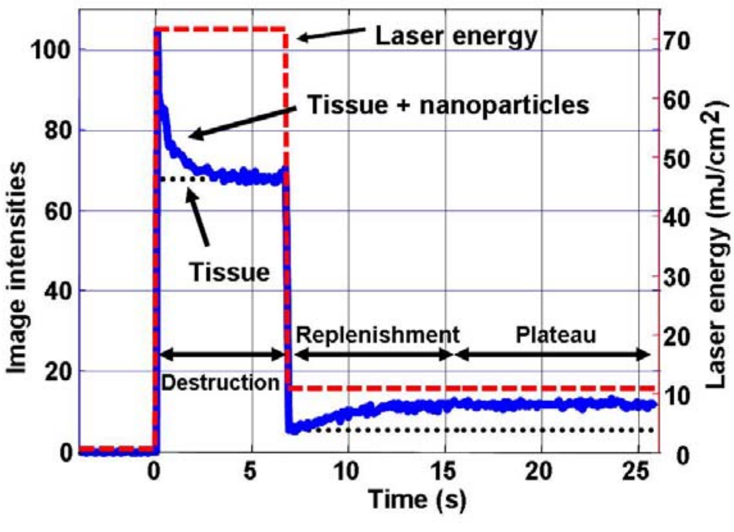

Fig. 5.9 Measured TIC from Fig. 5.8 in the destruction (t = 0–7 s) and replenishment (t = 7–26 s) phases (solid line; left y-axis), the inferred tissue intensity (dotted line), and the laser energy (dashed line; right y-axis). The laser energy was reduced at t = 7 s. A plateau phase occurred at t = 16–26 s, indicating a steady-state concentration of nanorods.

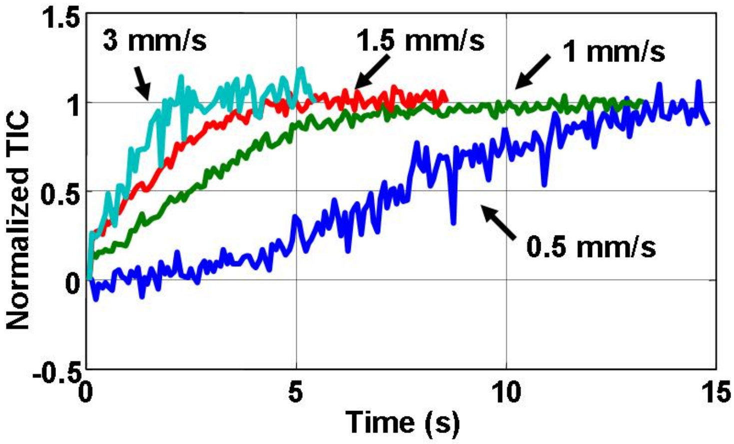

Fig. 5.10 Normalized TICs at flow rates of 0.5, 1, 1.5, and 3 mm/s.

The ITICs were then calculated by numerically integrating the TICs followed by fitting, both of which were performed using MATLAB (The MathWorks, MA). The TICs were measured six times in each case, from which mean and standard deviation (STD) values were calculated. In Eq. (5.19), flow rate v is proportional to the product of fitting parameter β (i.e., rate constant) and the width of irradiated volume, E. Fig. 5.11 shows the mean perfusion rate calculated for irradiated zones with widths ranging from 1 to 5 mm. The results calculated with a large E (i.e., a broad irradiated zone along the y-axis) are overestimations, whereas a small E results in underestimations of the flow velocity. It is clear from the figure that using $E = 3$ mm gives the best agreement with the theoretical flow rate. The width of the irradiated volume is consistent with the light-guide output width, as measured manually with a ruler.

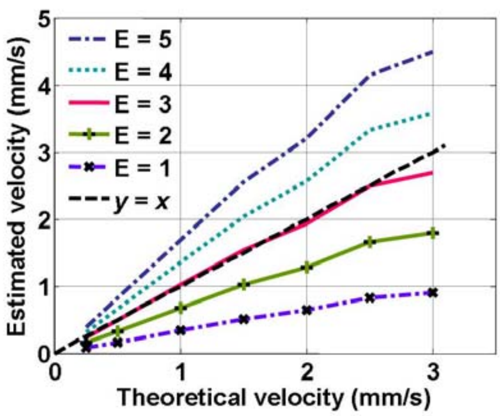

Fig. 5.11 Estimation results of the flow rate for E values from 1 to 5 mm.

A comparison between the experimental results using *E*=3 mm and the actual flow velocities is shown in Fig. 5.12. Because the ROI covers nearly the entire cross-section of the tube, the measured results can be viewed as the mean flow velocity inside the sample volume, which are in good agreement with the actual flow velocities. The linear regression curve between the measured velocities (y) and the actual velocities (x) is described by $y = 1.07x + 0.06$, which also indicates the high accuracy of this technique. The correlation coefficient between the measured flow velocities and their linear regression fit was 0.95. Fig. 5.12 also shows that the STDs increase with the mean values, with Fig. 5.13 plotting the normalized STD-to-mean ratios (the average value is 21.9%). This relationship may be attributable to the precision of the stepping motor inside the infusion pump – which controls the flow velocity of the perfusion phantom – not being sufficient for the low-velocity experiments, resulting in measurement errors.

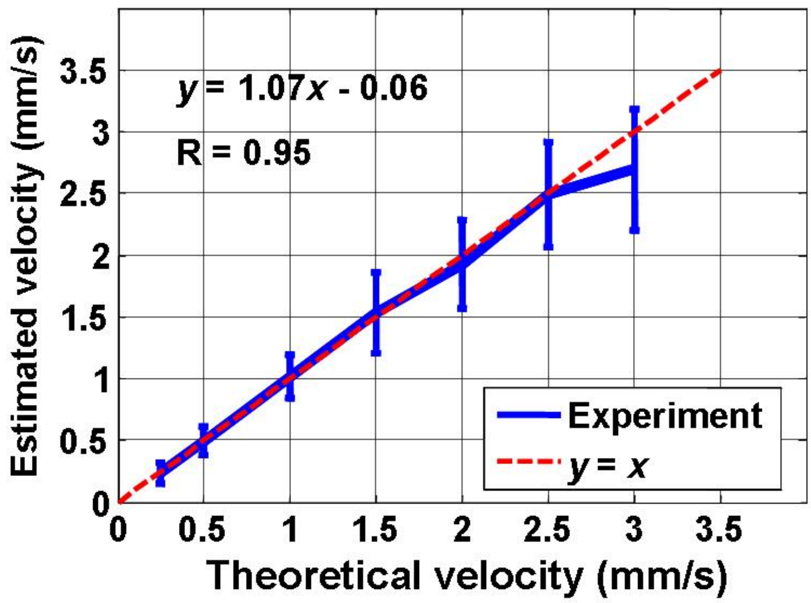

Fig. 5.12 Perfusion estimation results (solid line) and the ideal curve (dashed line) for an irradiated zone with a width of 3 mm.

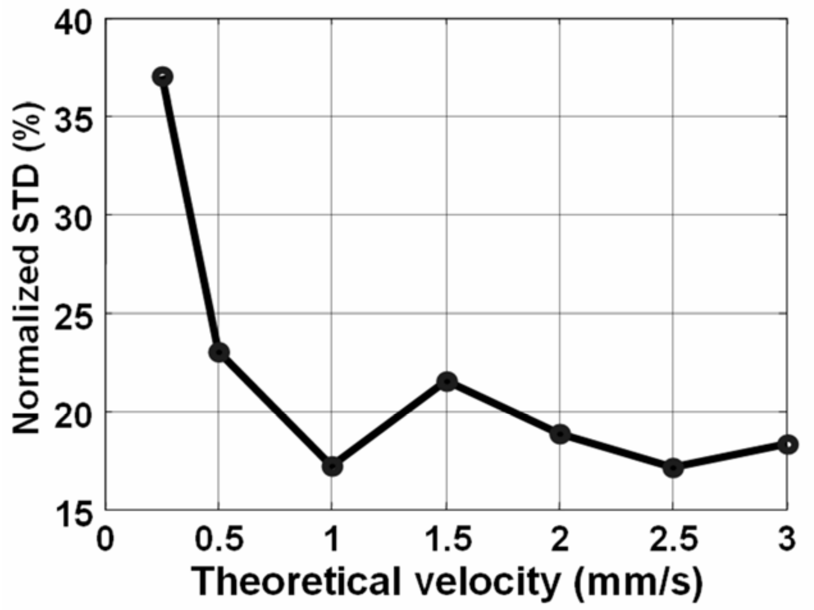

Fig. 5.13 Normalized STD versus the flow velocity. The normalized STD is less than 25% except for the lowest velocity, and its average value is 21.9%.

5.5 *In vitro* study (Single-energy flow measurement)

Besides the phantom study, we also perform experiments in measuring the realistic blood flow inside a biological tissue. Fig. 5.14 shows a schematic diagram of the flow measurement setup. A sample was made of chicken breast tissue. In which, a polyethylene tubing (Intramedic™ 427411, BD, USA) with a inner diameter of 580 μm was embedded at a depth of 2 mm. A volume of 1 ml of human blood and 55 μl of gold nanorods with an absorption peak at 985 nm at a concentration of 3.6 nM were mixed and injected into the tubing with a 1-ml standard syringe. The syringe was controlled by the infusion pump to create mean flow velocities ranging from 0.125 to 2 mm/s. The theoretical flow velocity is the mean value of the entire flow region. It was calculated from the pumping rate of the infusion pump with the cross-sectional area size of flow region (i.e., the tubing). Before these experiments, the pumping rate has been tested by measuring the weight of the pumped water. The photoacoustic probe was positioned 13 mm above the tube, and cross-sectional images were captured. TICs were achieved by summing the photoacoustic intensities from within a 0.6 × 1.2-mm ROI (8 × 4 pixels in the *z*- and *x*-axes, respectively) at each time point.

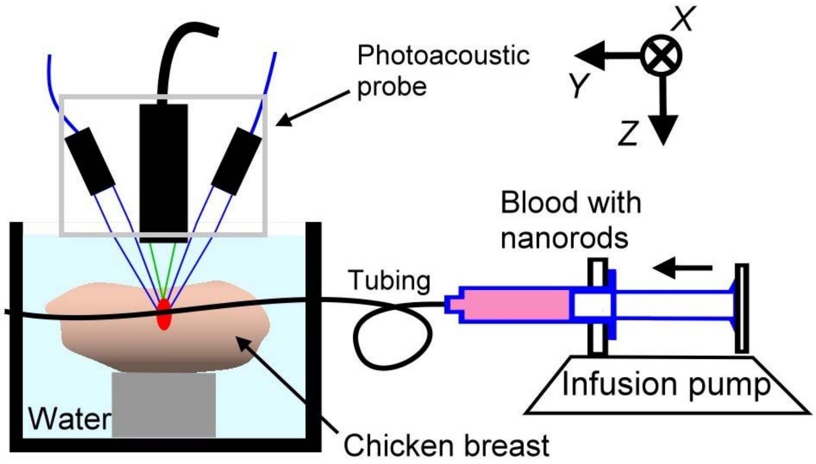

Fig. 5.14 Experimental setup of the perfusion phantom, in which the perfusion rate was controlled by the infusion pump with a syringe. The tubing was placed inside the chicken breast tissue to simulate tissue microcirculation. The flow velocities ranged from 0.125 to 2 mm/s.

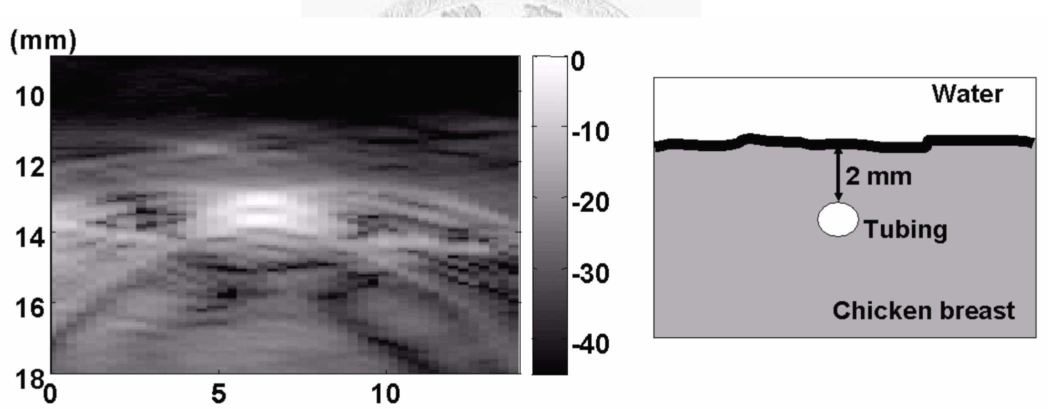

Fig. 5.15 Chicken breast image. The tubing with a inner diameter of 580 μm was immersed at a depth of 2mm from the tissue surface. The displayed dynamic range is 45 dB.

Fig. 5.15 shows focused cross-sectional images of the perfusion phantom. In this figure, the position of the chicken breast tissue and also the tubing show consistent with their location. The tubing is at a depth of 2 mm from the chicken breast surface, a fact that the laser energy irradiates the tubing after propagating through light scattering and absorbing biological tissue. In this case, the destruction of the gold nanorods from the outer of the tissue sample becomes difficult since the laser intensity decays along the propagation depth due to the light attenuation. Images captured during the measurement (t = 0–16.5 s) are shown in Fig. 5.16(a)–(c), displayed with a dynamic range of -10 dB. These images display a depth of 2.5 mm and a width of 5 mm and were normalized by subtracting the background image captured without gold nanorods. Therefore, these images show only the photoacoustic signals from the nanorods. The laser energy was set at 82.4 mJ/cm^2 (i.e., at t = 0 s). It is clear that the image intensity decreases with time, indicating that the gold nanorods inside the tube underwent shape changes due to the strong incident laser energy that reduced the optical absorption at the laser wavelength. A steady state was reached after continuous laser irradiation at the same energy level for 16 s, at which point the number of nanorods that underwent shape transition was roughly the same as the number of new nanorods flowing into the ROI. A square region with a size of 0.6 × 1.2 mm was selected as the ROI, as indicated by the dashed box in Fig. 5.16(a). The mean image intensities within the ROI were summed to create the TIC. Fig. 5.17 shows the normalized TICs measured at flow rates of 0.125, 0.25, 1, and 2 mm/s, which clearly indicates that the replenishment rate of the nanorods increases with the flow rate, as described by Eq. (5.17).

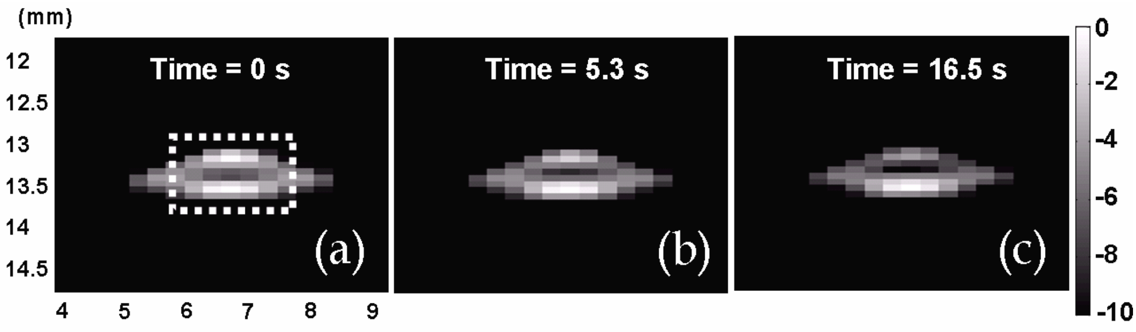

Fig. 5.16 Images captured at different times at a flow rate of 0.125 mm/s. The displayed dynamic range is 10 dB. Note that these images were normalized by subtracting the background image captured without gold nanorods.

The TICs were then calculated by fitting, which were performed using MATLAB. The TICs were measured five times in each case, from which mean and standard deviation (STD) values were calculated. In Eq. (5.19), flow rate v is proportional to the product of fitting parameter β (i.e., rate constant) and the width of irradiated volume, E. Fig. 5.19 shows the mean perfusion rate calculated for irradiated zones with widths ranging from 0.2 to 1.0 mm. The results calculated with a large E (i.e., a broad irradiated zone along the y-axis) are overestimations, whereas a small E results in underestimations of the flow velocity. It is clear from the figure that using E = 0.5 mm gives the best agreement with the theoretical flow rate. However, the width of the irradiated volume of this system is 0.8 mm (which was measured by using knife-edge method).

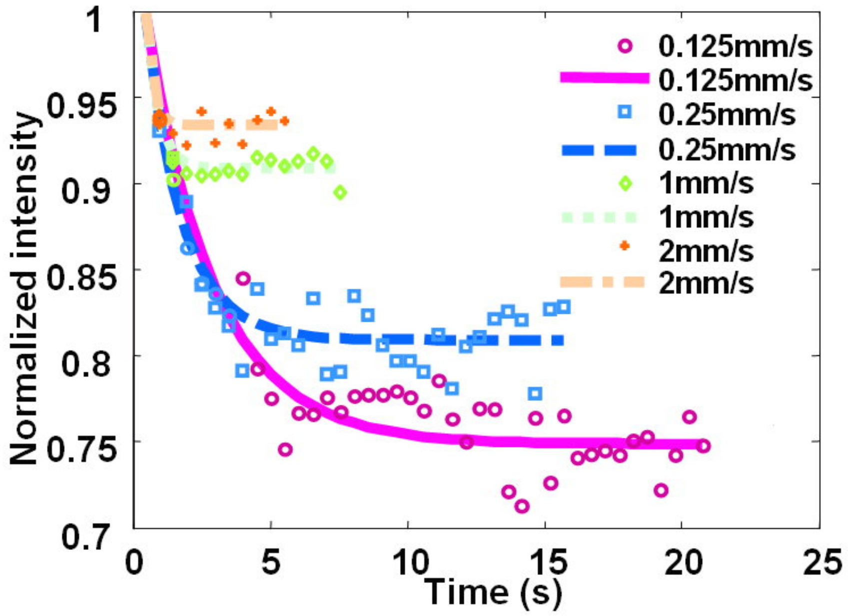

Fig. 5.17 Normalized TICs (markers) and their corresponding fitted curves (lines) at flow rates of 0.125, 0.25, 1, and 2 mm/s respectively.

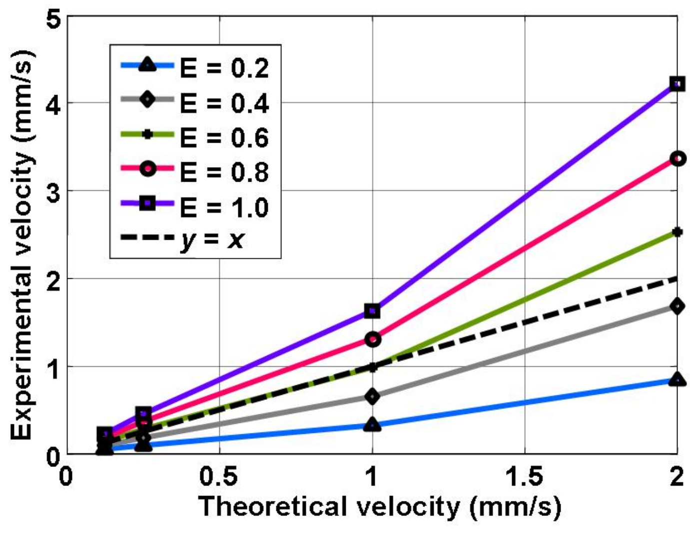

Fig. 5.18 Estimation results of the flow rate for E values from 0.2 to 1 mm.

A comparison between the experimental results using E = 0.8 mm and the actual flow velocities is shown in Fig. 5.19. Because the ROI covers nearly the entire cross-section of the tube, the measured results can be viewed as the mean flow velocity inside the sample volume. It is obvious that most of the flow velocities are overestimated. The linear regression curve between the measured velocities (y) and the actual velocities (x) is described by $y = 1.68x - 0.12$, which indicates that the measured flow velocity is higher than the actual one. The correlation coefficient between the measured flow velocities and their linear regression fit was 0.83. Fig. 5.19 also shows that the STDs increase with the mean values, with Fig. 5.20 plotting the normalized STD-to-mean ratios (the average value is 31.3%). This relationship may be attributable to the SNR of TICs. In high flow velocities, replenishment become more effective, which means that the steady-state (in which the number of incoming new nanorods approximates to that of the destroyed nanorods) is easier to approach as shown in Fig. 5.17. Therefore, fitting such low contrast curves without sufficient SNR leads to measurement errors. This problem can be solved if a larger ROI is chosen to increase the SNR.

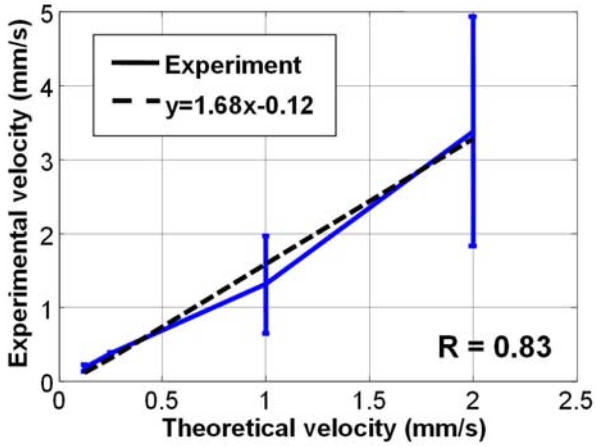

Fig. 5.19 Flow estimation results (solid line) and the ideal curve (dashed line) for an irradiated zone with a width of 0.8 mm.

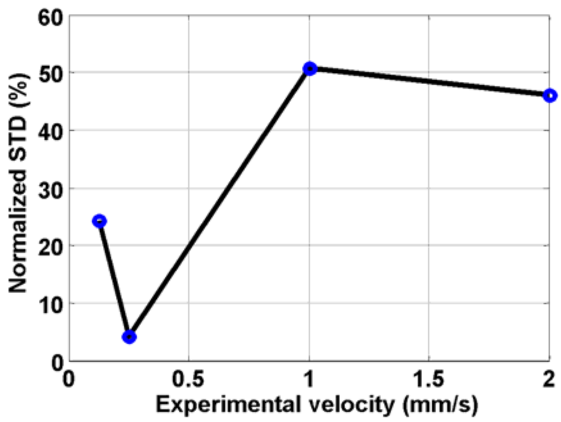

Fig. 5.20 Normalized STD versus the flow velocity. The average value is 31.3%.

5.6 Discussion

The rate constant is defined as the ratio of the flow velocity to the width of the irradiated zone, and represents the replenishment rate inside the irradiated volume (see Fig. 5.1 and Fig. 5.3). A large rate constant means that the concentration of new nanoparticles inside the irradiated zone rapidly reaches a steady state. Therefore, either increasing the flow velocity or decreasing the width of the irradiated zone increases the rate constant. Based on this principle, the flow velocity can be determined from the width of the irradiated zone and the sampling rate. In order to investigate the relation between the rate constant, β, and the sampling rate, simulations of both the single-energy and the dual-energy methods were performed.

In the single-energy mode, TICs were calculated for various rate constants ranging from 0.2/s to 10/s using Eq. (5.17). The simulated TICs were sampled at rates ranging from 1–50 samples/s. These TICs were curve fitted for rate-constant estimation (as the last step in flow estimation). Comparisons between the measured rate constants with the predetermined values are presented in Fig. 5.21(a). In this figure, most of the ratios are more than unity, meaning that the measured rate constant is 10% to 20% higher than the determined one. This could be a possible reason of the overestimations as shown in Fig. 5.19. On the other hand, it is also noticeable that the resulting ratios are less than unity when the sampling rate is insufficient, meaning that the measured flow rate is lower than the determined one. This may be due to a high flow velocity in an irradiated zone resulting in a large rate constant and thus a short replenishment period. With an irradiated zone of constant width and a fixed frame rate, underestimation is worse when the flow velocity is higher (i.e., higher β). In Fig. 5.21(a), the system frame rate of 15 Hz is indicated by the vertical dashed line. The flow velocity corresponding to rate constants of 0.2/s, 1/s, and 5/s are 0.16, 0.8, and 4 mm/s, respectively (assuming an irradiation width of 0.8 mm).

On the other hand, dual-energy TICs were also calculated for various rate constants ranging from 0.2/s to 10/s using Eq. (5.20). The simulated TICs were sampled at rates ranging from 5–100 samples/s and then were used to produce ITICs. These ITICs were curve fitted for rate-constant estimation (as the last step in flow estimation). Comparisons between the measured rate constants with the predetermined values are presented in Fig. 5.21(b). In this figure, all the resulting ratios are less than unity, meaning that the measured rate constant is always lower than the determined one (i.e., underestimation). With an irradiated zone of constant width and a fixed frame rate, underestimation is worse when the flow velocity is higher, which also explains the underestimation at 3 mm/s shown in Fig. 5.12. The flow velocity corresponding to rate constants of 0.2/s, 0.5/s, and 1/s are 0.6, 1.5, and 3 mm/s, respectively (assuming an irradiation width of 3 mm). The simulation results are also consistent with the measurement results shown in Fig. 5.11.

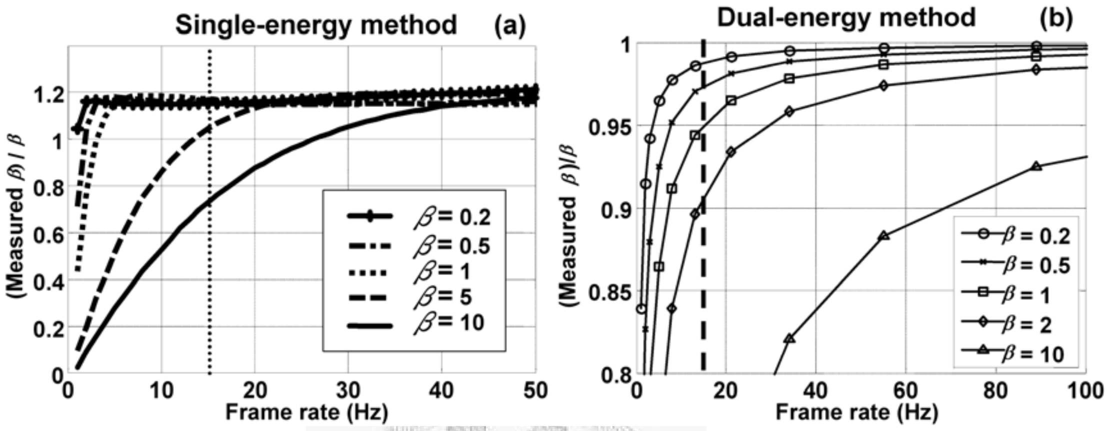

Fig. 5.21 Ratio of the measured β to the predetermined β from numerical simulations in single-energy (a) and dual-energy (b) methods. The frame rate of the current system (i.e., 15 Hz) is indicated by the vertical dashed line.

Fig. 5.12 indicates that the flow velocity is underestimated at 3 mm/s. This may be due to a high flow velocity in an irradiated zone resulting in a large rate constant, β (according to Eq. (12)), and thus a short replenishment period. Undersampling with a low frame rate produces measurement errors in ITIC fitting. A large rate constant means that the concentration of new nanoparticles inside the irradiated zone rapidly reaches a steady state (i.e., with the nanorods homogeneously distributed as in the original state). Therefore, either increasing the flow velocity or decreasing the width of the irradiated zone increases the rate constant. Based on this principle, the flow velocity can be determined from the width of the irradiated zone and the sampling rate.

5.7 Concluding remarks

We have experimentally demonstrated the feasibility of nanorod-based flow measurement based on a high-frame-rate photoacoustic imaging system, which currently has a frame rate up to 15 Hz. The linearity between the nanorod concentration and photoacoustic intensities has been verified. The results of the perfusion experiments show that flow velocities ranging from 0.125 to 2 mm/s can be measured, with an average normalized STD of 31.3%. The measurable flow rate of this method is limited by the PRF of the laser system. The feasibility of *in vivo* studies has also been discussed. In order to apply this flow measurement method to preclinical research involving small-animal models, one future direction is to build a photoacoustic imaging system equipped with a transducer array operating at a higher frequency (to improve the imaging spatial resolution) and a laser with a higher PRF (to provide a high frame rate).

Chapter 6 Discussion

6.1 The reconstruction algorithm

6.1.1 Lateral resolution and CNR

Although the benefit of the reconstruction algorithm for improving the contrast of the absorption distribution was demonstrated in Chapter 4, these images suffered from the degraded lateral resolution due to the integration in the reconstruction algorithm. Since the contrast and the spatial resolution are two important parameters that represent the imaging quality, it is necessary to evaluate the difference of these parameters from the conventional focusing method and the reconstruction algorithm. In order to quantify these two parameters, simulations for three squares with an area of 0.8×0.8, 1.2×1.2, and 1.6×1.6 mm^2 were accomplished individually, in which the simulation status was set to be the same as that in Section 4.2.

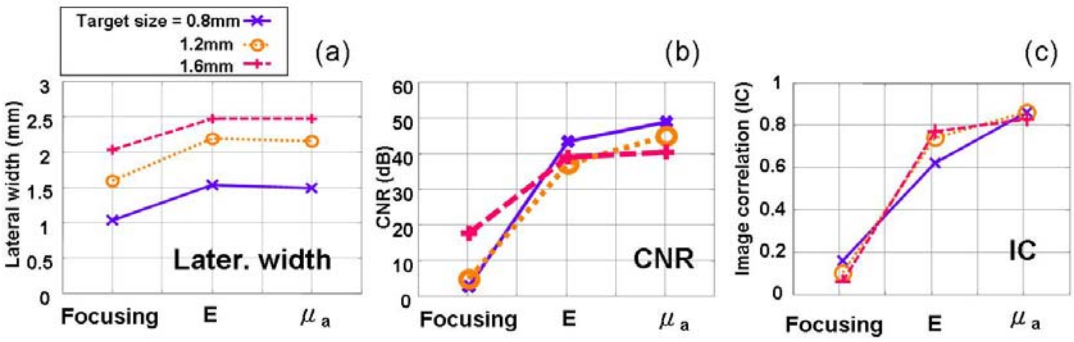

Fig. 6.1 The lateral resolution, CNR, and IC evaluated from the images of the conventional focusing, the RED, and the IRA by using three square phantoms with a size of 0.8×0.8 (solid), 1.2×1.2 (dotted), 1.6×1.6 mm^2 (dashed).

Fig. 6.1 shows the measured parameters including the lateral width, the CNR, and the IC. In Fig. 6.1(a), all the lateral widths of these squares were larger than the theoretical widths especially the results after the RED and the IRA, a fact that the reconstruction algorithm resulted in a degraded lateral resolution. The Fig. 6.1(b) shows that the RED improved the CNRs by 20dB over the conventional method, and these CNRs were further improved by the IRA. Also, a similar improvement of the ICs can be observed in Fig. 6.1(c). Averages of these parameters were calculated as shown in Table 6.1. Note that the lateral resolution was evaluated to be the ratio of the measured lateral width to the theoretical width since the focusing quality is dependant on the frequency of the photoacoustic signals that are determined by the distribution of the energy deposition. In this table, the effects of the reconstruction algorithm to the lateral resolution and the contrast enhancement are clearly depicted. The average lateral resolution degrades 58 % as compared with theoretical width of the phantom, meaning that an absorber with a lateral width of 1 mm could be revealed to a 1.58 mm width after the reconstruction. However, with a lost lateral resolution, the reconstruction algorithm provides a great improvement of the absorption contrast. It improved the CNR by 5 times and the IC by 7.8 times over the conventional method. This table presents the trade-off of the contrast improvement and the degraded lateral resolution after using the reconstruction algorithm.

Table 6.2: The average values of the lateral-to-theoretical width, the IC, and the CNR from Fig. 6.1.

Ave. parameters	**Focusing**	**Recons. *E***	**Recons. μ_a**
Lateral / theoretical width	1.18	1.61	**1.58**
IC	0.11	0.71	**0.85**
CNR (dB)	9.05	40.57	**45.46**

Note that the lateral resolution was evaluated to be the ratio of the measured lateral width to the theoretical width.

6.1.2 Influence of the optical scattering

In Chapter 4, we presented the efficacy of the reconstruction algorithm with a constant scattering coefficient throughout the simulation region. However, in most biological applications, the scattering coefficient also depends on the tissue and investigating the influence of the scattering on the reconstruction algorithm is of importance. Here, we adopted the absorption sample used in Section 3.4.1 and performed the proposed reconstruction algorithm to evaluate the influence caused due to numerous kinds of scattering coefficient in the numerical simulation, in which all the reconstruction conditions were set to be the same as those in Section 4.2.

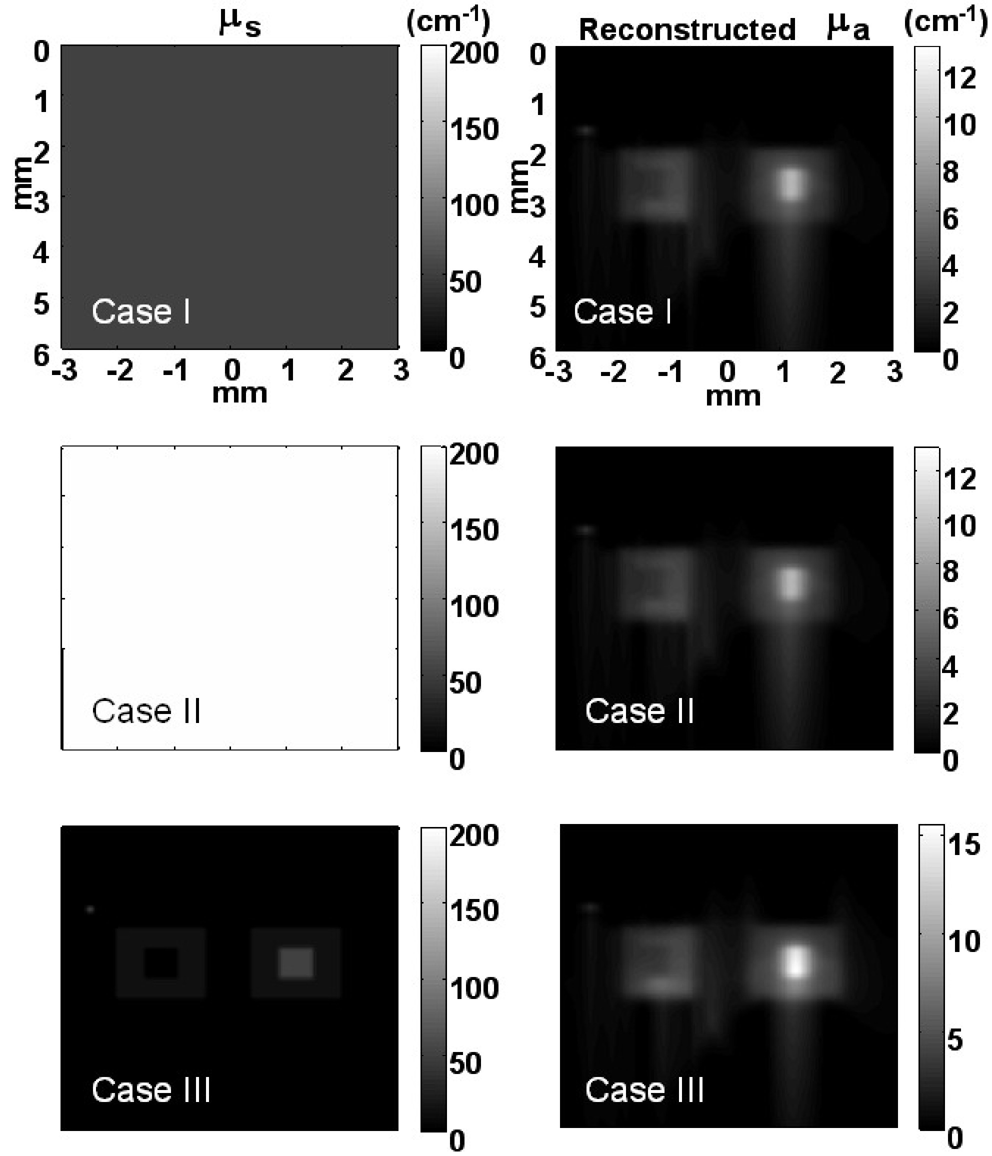

Fig. 6.2 Different cases of predetermined scattering distributions (left) and the corresponding reconstructed absorption distributions (right) in the numerical simulation. In case I and II, the scattering coefficients were set to be a constant value of 50 and 200 cm^{-1}. In case III and IV, the scattering coefficients were set to be in direct and inverse proportion to the absorption distribution. In case V and VI, the scattering coefficients were set to be two arbitrary distributions. Note that all the predetermined scattering distributions and the resultant absorption distributions are shown in a unit of cm^{-1}.

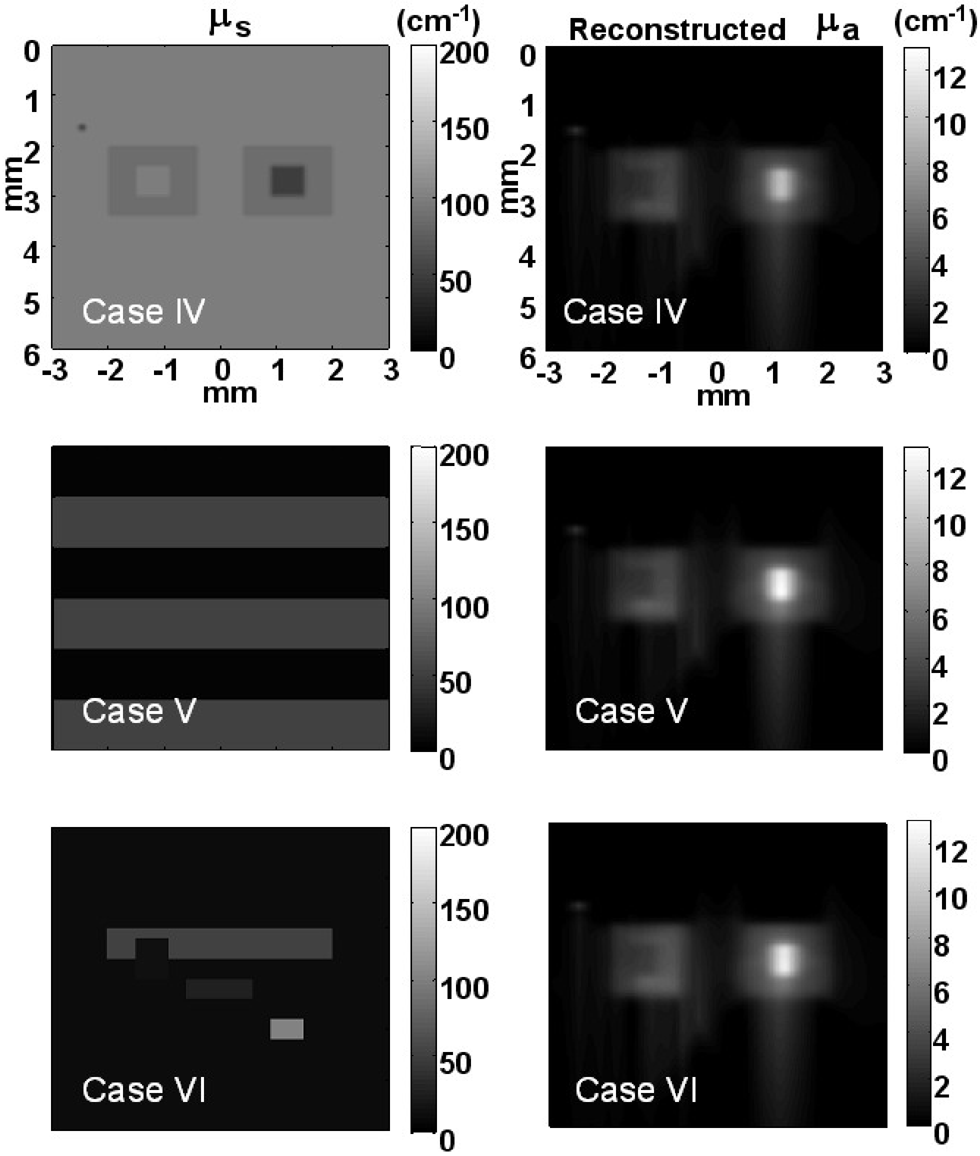

Fig. 6.3 (continued)

Fig. 6.2 shows the reconstructed absorption distributions with 6 cases of scattering distributions. In case I and II, the scattering coefficients were set to be a constant value of 50 and 200 cm^{-1}. Case III and IV were set to be in direct and inverse proportion to the absorption distribution, respectively. In case V and VI, the scattering coefficients were arbitrary distributed. In this figure, images of the resultant absorption distributions reveal less effect on the scattering coefficient, meaning that the reconstruction algorithm is insensitive to the scattering coefficient. Because the strong sidelobes blurred the resultant energy deposition in the RED, the resolution of the reconstructed energy deposition was degraded and the influence of the scattering coefficient became insignificant. It implies that the results cannot reveal the detail of the laser fluence, which was characterized by the scattering coefficient.

In addition, the proposed IRA was applied without considering the scattering effect since we adopted the depth-profiling method (i.e., the Beer's law) to measure the laser fluence instead of the diffusion approximation and the scattering effect was neglected in the calculation of the laser fluence. This implies that the proposed algorithm cannot present the exact absorption coefficient since both the absorption and the scattering involve the generation of photoacoustic signals in reality.

6.1.3 Influence of the SNR

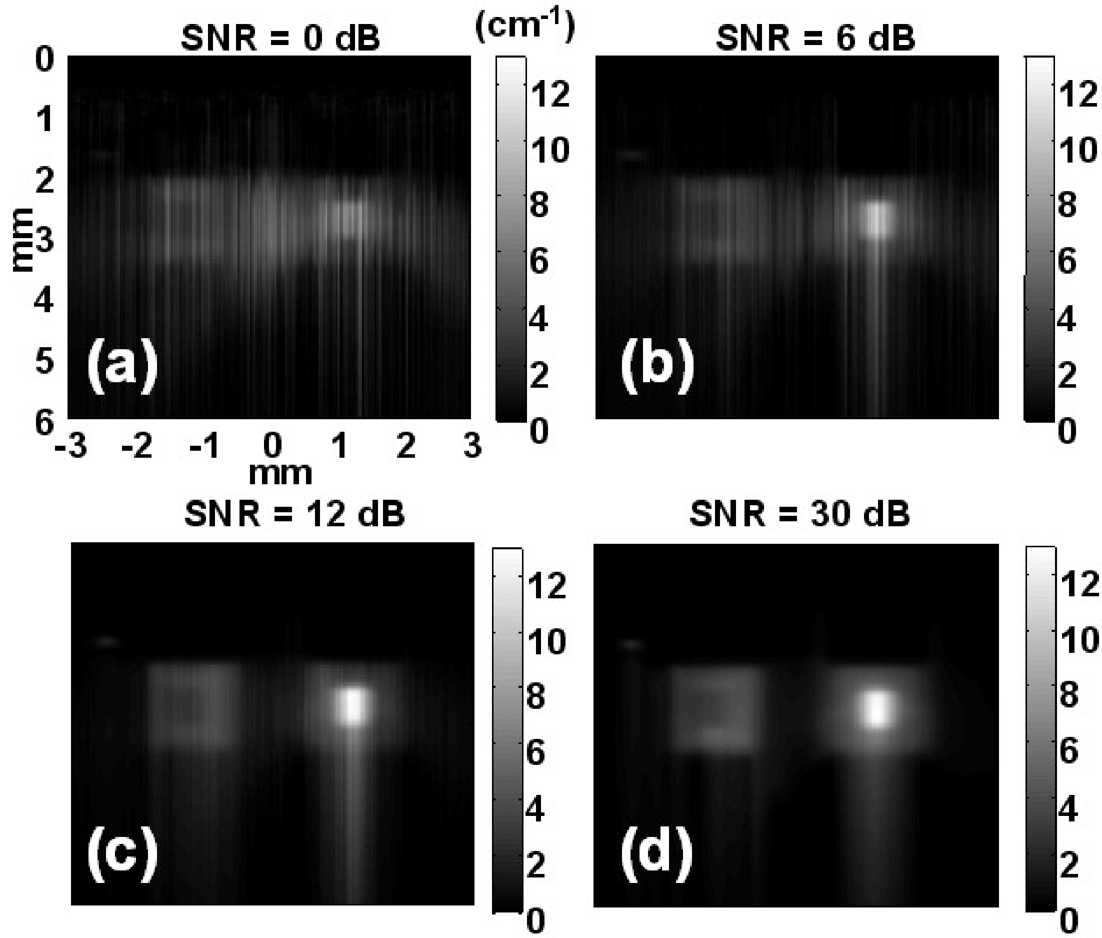

Fig. 6.4 Reconstructed absorption distributions by using the photoacoustic signals with a SNR of 0 dB (a), 6 dB (b), 12 dB (c), and 30 dB (d).

In this section, we further discuss the influence of the SNR on the propose algorithm. Fig. 6.4 shows the reconstructed absorption distributions that were performed using the same simulation method as described in the previous section. These absorption images were measured by using the photoacoustic signals with a SNR of 0, 6, 12, and 30 dB as shown in Fig. 6.4 (a), (b), (c), and (d), respectively. Apparently, the images with a low SNR present the absorption distribution with strip-liked artifacts in axial direction. These artifacts were produced due to the integration of the random-distributed spikes in the RED. In addition to the artifacts, the image resolution was also reduced in those images with a low SNR. In Section 2.3.2, we discussed the interference of the noise to the CF and numerically demonstrated that the CF value is proportion to the SNR. A low SNR reduces the CF value and hence the efficacy of the CF to suppress the sidelobes is limited. Therefore, the imaging resolution shown in Fig. 6.4(a) was degraded.

6.1.4 Reconstruction of a realistic tissue sample (a simulation case)

In Chapter 4, the ability of the proposed reconstruction algorithm has been demonstrated to reconstruct samples with rectangular structures. However, in realistic practice, complex samples have to be faced since the ultimate goal of the proposed algorithm is to distinguish the biological tissue. In the following, the capability of the proposed reconstruction algorithm in a skin sample is presented. This sample was captured from a picture of skin frozen section [89] and calibrated to have a realistic absorption distribution by referring to the corresponding absorption coefficient of the skin tissue, including the stratum corneum (at the depth of 0.7 mm), the epidermis (0.7~1 mm), and the dermis (>1 mm), as shown in Fig. 6.5(a). This sample was then calculated to result in the energy deposition and the following photoacoustic signals by applying the same simulation procedure as described in Chapter 4. Note that in order to fit the small scale of this realistic tissue structure, a virtual transducer with an excellent bandwidth of 300-MHz was adopted in this simulation so that the photoacoustic signals of the sample could be measured accurately.

The results using the conventional focusing method, the RED, and the IRA are presented in Fig. 6.5(b)-(d). The focusing method again presents only the gradient of the absorption distribution. The image shows the intensity not at the position of the absorber. For instance, the epidermis at the depth of 0.9 mm is revealed as two straight lines rather than a stratum with a thickness of three hundred micron as shown in Fig. 6.5(a). On the contrary, the resultant energy deposition after the RED shows a profile with mostly a same position and shape as the theoretical absorption distribution (see Fig. 6.5(c)). Here, an additive reference point was placed at a depth of 0.2 mm and a lateral position of 2 mm above the sample. It was used to complete the final step of the proposed reconstruction method (i.e., the IRA) to obtain the absorption distribution, as shown in Fig. 6.5(d). In this figure, the image exhibits more intensity at the depth of epidermis, meaning that the absorbed energy above the epidermis (i.e., the stratum corneum) can be recovered and the absorption coefficient can be approximately obtained.

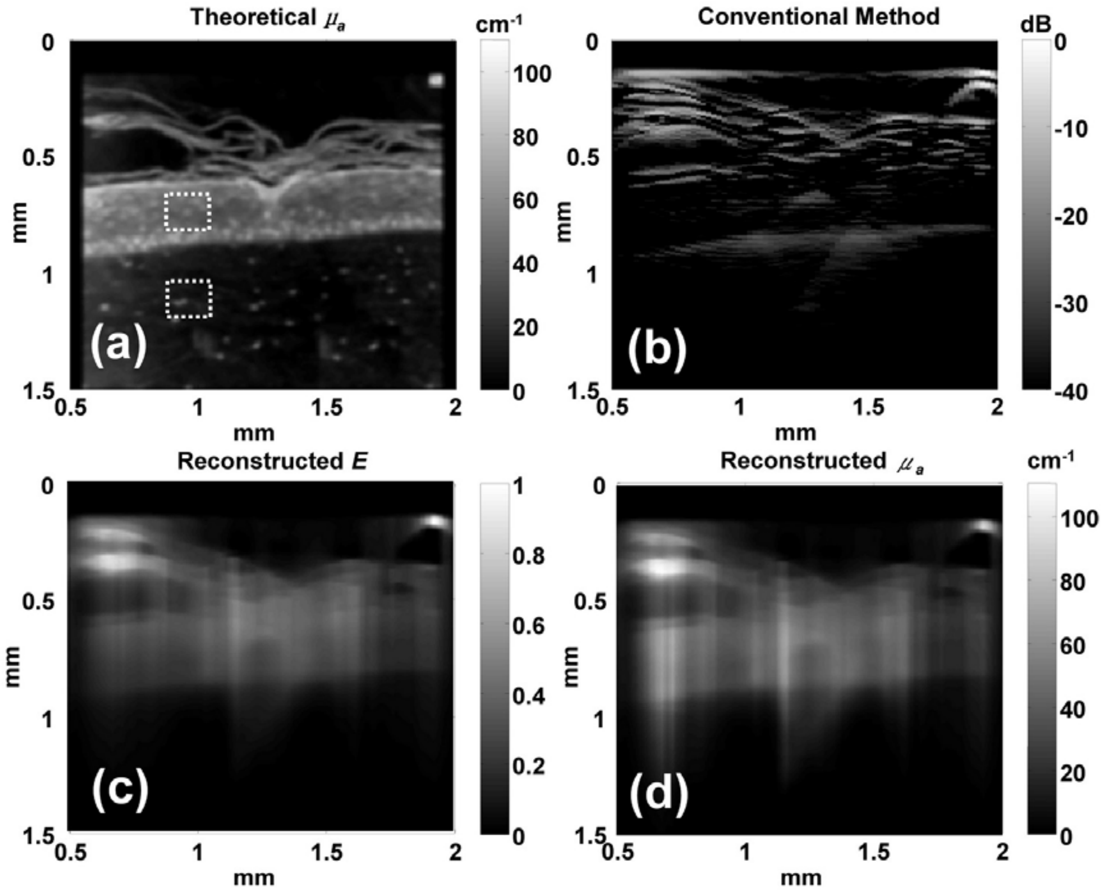

Fig. 6.5 Images of the theoretical absorption coefficient (a), the conventional focusing (b), the reconstructed energy deposition (c), and the reconstructed absorption coefficient. Note that the scale of the frozen section is in a range of several hundred microns. The additive reference point was placed at the depth of 0.2 mm and the lateral position of 2 mm of the image with an absorption coefficient of 80 cm^{-1}.

In order to evaluate the efficacy of these results, the SAD, SRD, IC, and CNR were calculated and listed in Table 6.3. These parameters were measured as a comparison between the reconstruction results and the theoretical absorption distribution. Note that the CNR were evaluated from two ROIs with a size of 0.1 × 0.1

mm^2 in the epidermis and the dermis regions that are indicated by two rectangles in Fig. 6.5(a). As shown this table, the reconstructed absorption coefficient improved the SAD by 2 times, the IC by 10 times and the CNR by 29 dB over the conventional focusing method. The image correlation was also noticeably improved. This demonstrates that the proposed algorithm shows the image more similar to the theoretical distribution as compared to the conventional focusing method. The SRDs of the proposed method, however, is higher than that of the focusing method. A possible reason is that the reconstruction results were blurred due to the degraded lateral resolution caused by the significant enhancement of the low frequency signals in the reconstruction algorithm.

Table 6.3: The SAD, SRD, IC, and CNR values measured from Fig. 6.5

Parameters	**Theory**	**Focusing**	**Recons. *E***	**Recons. μ_a**
SAD	0	0.15	**0.10**	**0.08**
SRD	0	2.73	**14.67**	**11.54**
IC	1	0.07	**0.66**	**0.71**
CNR (dB)	31	14	**48**	**43**

Note that the SAD, SRD, and IC were measured as a comparison between the image and the theoretical absorption image and the CNRs were evaluated from the differences between the epidermis and the dermis region (indicated by the rectangles at a depth of 0.9 and 1.1 mm, respectively).

6.2 The wash-in flow estimation method

6.2.1 Feasibility of *in vivo* flow assessment

The results presented in the Chapter 5 show that the wash-in flow-estimation methods can be implemented utilizing images captured by a high-frame-rate photoacoustic imaging system. However, two issues need to be addressed before making *in vivo* measurements. First, our experiments were conducted with a measured laser beam width. However, the width of the irradiated zone in the tissue is difficult to evaluate when the laser pulse propagates through a strongly scattering medium, and an incorrect width leads to measurement errors, as shown in Fig. 5.11 and Fig. 5.18. Therefore, the difference between the assumed and actual width is a critical problem in this method if absolute measurements are required. Nonetheless, relative measurements can be made even in the presence errors in E. Second, the measurable range of the perfusion rate is determined by both the frame rate (i.e., sampling rate) and the width of the irradiated zone in the ROI. There is therefore a trade-off between the elevational resolution (i.e., the resolution along the axis perpendicular to the cross-sectional image) and the measurable perfusion rate. On the other hand, actual flow rates ranging from 0.5 to 10 mm/s in capillaries smaller than 200 μm have been verified using an intravital microscopy [83]. Therefore, such applications of this method require a system with a broad sampling range.

In addition, we tried to implement the dual-energy method in *in vitro* experiments. However, the lower laser energy propagated through turbid biological tissues cannot provide sufficient SNR for the replenishment measurement. Therefore, in strong scattering and absorbing tissue, it is much easier to achieve the flow estimation method in single-energy than that in dual-energy.

6.2.2 Feasibility of using the reconstructed absorption in the flow estimation

The wash-in time-intensity flow measurement is based on monitoring the concentration of gold nanorods inside the fluid via the photoacoustic image acquisition. The concentration of gold nanorods directly reflects the optical absorption coefficient, μ_a, which mainly contributes the intensity of the photoacoustic signals. In Chapter 5, the linear array transducer with a center frequency of 5 MHz and an 82% bandwidth was used to capture photoacoustic images. However, it is difficult to perform the reconstruction algorithm with such a transducer since a wideband photoacoustic acquirement is needed in the reconstruction algorithm. Another noticeable problem is that the significant sidelobes and the tail-artifacts in the reconstruction results have to be considered in measuring the flow. It is possible that these reconstruction errors yield the benefit of obtaining the absorption coefficient for the flow assessment.

Chapter 7 Conclusions and future works

In this thesis, we proposed an efficient algorithm to quantitatively reconstruct the optical absorption coefficient for the backward mode photoacoustic imaging. Three sequential steps of the proposed reconstruction algorithm including the adaptive-weighted focusing, the RED, and the IRA were introduced. The efficacy of these steps was demonstrated in both the numerical simulations and the experiments. In Chapter 2, the results by using the adaptive-weighted focusing show that the lateral resolution was improved by 2 times and the SNR was increased 4-12 dB as compared with the conventional method. The influence of the SNR to the CF value was also discussed. In Chapter 3, the results after the RED (i.e., the second step of the reconstruction algorithm) show images with mostly the same shape and position of the optical absorber. The capability of the RED was also demonstrated to improve the SAD, the SRD, and the IC by 3 times and the CNR by 17 dB over the conventional method. The final step of the proposed reconstruction algorithm (i.e., the IRA) was introduced in Chapter 4. In the simulation, a comparison between the reconstructed and the theoretical absorption distribution was measured with an average error of 7.42 %. Phantom experiments, however, show that an inadequate energy deposition was obtained due to the significant sidelobes and imperfect frequency response of the hydrophone. The influences of both the scattering and the SNR on the reconstruction algorithm were also discussed. The trade-off between the contrast improvement and the resolution degradation by using the reconstruction algorithm were discussed in Chapter 6. In the results, the average lateral resolution degrades 58 % as compared with theoretical width of the square phantom. However, the reconstruction algorithm improved the CNR by 5 times and the IC by 7.8 times over the conventional method. Although, the backward mode photoacoustic imaging has suffered from the small angular extent during the data acquisition, the feasibility of the reconstruction algorithm in visualizing both the energy deposition and the further absorption coefficient was demonstrated.

On the other hand, we also performed the flow assessment, including the single- and dual-energy wash-in methods, by using the high-frame-rate backward mode photoacoustic imaging system in Chapter 5. In the dual-energy mode, the flow velocities ranging from 0.25 to 3 mm/s were accurately measured with a transparent plastic phantom. An average normalized STD of 21.9% was performed. The single-energy mode was performed in *in vitro* experiments. In the result, the flow velocities ranging from 0.125 to 2 mm/s were measured with an average normalized STD of 31.3%. The measurable range of the flow velocity in both the single- and dual-energy wash-in flow measurement was discussed.

Future works of this study is to improve the focusing quality. According to the reconstruction results shown in the thesis, the insufficient focusing due to the small angular extent in backward mode photoacoustic imaging causes the sidelobes and hence affects the capability of the reconstruction. Therefore, a focus-improved image assists the proposed algorithm to obtain the absorption coefficient more accurately. A high-speed wideband photoacoustic array system is another future direction of this study. Using such a wideband system, the flow assessment by using the reconstructed absorption coefficient becomes achievable. On the other hand, using an imaging system with a higher frame rate enlarges the measurable range of the flow velocity as discussed in Chapter 5. Under this condition, using the wash-in flow estimation method in *in vivo* experiments becomes more feasible and reliable.

References

[1] A. G. Bell, "Production of sound by radiant energy," *Manufacturer and builder,* vol. 13, pp. 156-158, 1881.

[2] R. M. White, "Generation of Elastic Waves by Transient Surface Heating," *Journal of Applied Physics,* vol. 34, pp. 3559, 1963.

[3] R. M. White, "Elastic Wave Generation by Electron Bombardment or Electromagnetic Wave Absorption," *Journal of Applied Physics,* vol. 34, pp. 2123, 1963.

[4] V. E. Gusev and A. A. Karabutov, *Laser optoacoustics*. New York: American Institute of Physics, 1993.

[5] W. Zhang and Q. X. Yu, "IR thermal-emitter based photoacoustic spectrometer for gas detection," *Spectroscopy and Spectral Analysis,* vol. 27, pp. 614-618, Mar 2007.

[6] A. Elia, C. Di Franco, P. M. Lugara, and G. Scamarcio, "Photoacoustic spectroscopy with quantum cascade lasers for trace gas detection," *Sensors,* vol. 6, pp. 1411-1419, Oct 2006.

[7] J. Kandulla, H. Elsner, R. Birngruber, and R. Brinkmann, "Noninvasive optoacoustic online retinal temperature determination during continuous-wave laser irradiation," *Journal of Biomedical Optics,* vol. 11, pp. -, Jul-Aug 2006.

[8] S. K. Herbert, K. Y. Biel, and T. C. Vogelmann, "A photoacoustic method for rapid assessment of temperature effects on photosynthesis," *Photosynthesis Research,* vol. 87, pp. 287-294, Mar 2006.

[9] I. V. Larina, K. V. Larin, and R. O. Esenaliev, "Real-time optoacoustic monitoring of temperature in tissues," *Journal of Physics D-Applied Physics,* vol. 38, pp. 2633-2639, Aug 7 2005.

[10] R. G. M. Kolkman, W. Steenbergen, and T. G. van Leeuwen, "Reflection mode photoacoustic measurement of speed of sound," *Optics Express,* vol. 15, pp. 3291-3300, Mar 19 2007.

[11] F. Hernandez, J. Morales, M. Navarrete, and M. Villagran-Muniz, "Determination of velocity profiles in pipes by a pulsed photoacoustic method," *Journal De Physique Iv,* vol. 125, pp. 339-341, Jun 2005.

[12] A. Blouin, D. Levesque, C. Neron, D. Drolet, and J. P. Monchalin, "Improved resolution and signal-to-noise ratio in laser-ultrasonics by SAFT processing," *Optics Express,* vol. 2, pp. 531-539, Jun 22 1998.

[13] D. Levesque, A. Blouin, C. Neron, and J. P. Monchalin, "Performance of laser-ultrasonic F-SAFT imaging," *Ultrasonics,* vol. 40, pp. 1057-1063, Dec 2002.

[14] V. Ntziachristos, J. Ripoll, L. H. V. Wang, and R. Weissleder, "Looking and listening to light: the evolution of whole-body photonic imaging," *Nature Biotechnology,* vol. 23, pp. 313-320, Mar 2005.

[15] X. D. Wang, Y. J. Pang, G. Ku, X. Y. Xie, G. Stoica, and L. H. V. Wang, "Noninvasive laser-induced photoacoustic tomography for structural and functional in vivo imaging of the brain," *Nature Biotechnology,* vol. 21, pp. 803-806, Jul 2003.

[16] H. F. Zhang, K. Maslov, G. Stoica, and L. H. V. Wang, "Functional photoacoustic microscopy for high-resolution and noninvasive in vivo imaging," *Nature Biotechnology,* vol. 24, pp. 848-851, Jul 2006.

[17] R. O. Esenaliev, A. A. Karabutov, and A. A. Oraevsky, "Sensitivity of laser opto-acoustic imaging in detection of small deeply embedded tumors," *Ieee Journal of Selected Topics in Quantum Electronics,* vol. 5, pp. 981-988, Jul-Aug 1999.

[18] A. A. Karabutov, N. B. Podymova, and V. S. Letokhov, "Time-resolved laser optoacoustic tomography of inhomogeneous media," *Applied Physics B-Lasers and Optics,* vol. 63, pp. 545-563, Dec 1996.

[19] V. V. Tuchin, *Tissue optics*. Washington: SPIE Press, 2000.

[20] W. F. Cheong, S. A. Prahl, and A. J. Welch, "A Review of the Optical-Properties

of Biological Tissues," *Ieee Journal of Quantum Electronics,* vol. 26, pp. 2166-2185, Dec 1990.

[21] S. Manohar, A. Kharine, J. C. G. van Hespen, W. Steenbergen, and T. G. van Leeuwen, "Photoacoustic mammography laboratory prototype: imaging of breast tissue phantoms," *Journal of Biomedical Optics,* vol. 9, pp. 1172-1181, Nov-Dec 2004.

[22] P. C. Li, C. W. Wei, C. K. Liao, C. D. Chen, K. C. Pao, C. R. C. Wang, Y. N. Wu, and D. B. Shieh, "Multiple targeting in photoacoustic imaging using bioconjugated gold nanorods," in *in BiOS, Proc. SPIE*, San Jose, 2006.

[23] L. H. V. Wang, "Ultrasound-mediated biophotonic imaging: A review of acousto-optical tomography and photo-acoustic tomography," *Disease Markers,* vol. 19, pp. 123-138, 2003.

[24] A. J. Welch and M. J. C. van Gemert, *Optical-termal response of laser-irradiated tissue*. New York: Plenum Press, 1995.

[25] E. Okada, M. Schweiger, S. R. Arridge, M. Firbank, and D. T. Delpy, "Experimental validation of Monte Carlo and finite-element methods for the estimation of the optical path length in inhomogeneous tissue," *Applied Optics,* vol. 35, pp. 3362-3371, Jul 1 1996.

[26] M. Walker, *Mathematical methods of physics*. Menlo Park: Benjamin/Cummings, 1970.

[27] B. Choi, E. D. Jansen, and A. J. Welch, "Acoustic-based measurements of material absorption coefficients: Relationship between laser pulse duration and stress confinement time," *Journal of Applied Physics,* vol. 94, pp. 7826-7831, Dec 15 2003.

[28] G. Paltauf and H. SchmidtKloiber, "Measurement of laser-induced acoustic waves with a calibrated optical transducer," *Journal of Applied Physics,* vol. 82, pp. 1525-1531, Aug 15 1997.

[29] X. D. Wang, G. Ku, M. A. Wegiel, D. J. Bornhop, G. Stoica, and L. H. V. Wang, "Noninvasive photoacoustic angiography of animal brains in vivo with near-infrared light and an optical contrast agent," *Optics Letters,* vol. 29, pp. 730-732, Apr 1 2004.

[30] R. A. Kruger, P. Y. Liu, Y. R. Fang, and C. R. Appledorn, "Photoacoustic Ultrasound (Paus) - Reconstruction Tomography," *Medical Physics,* vol. 22, pp. 1605-1609, Oct 1995.

[31] A. A. Karabutov, E. V. Savateeva, N. B. Podymova, and A. A. Oraevsky, "Backward mode detection of laser-induced wide-band ultrasonic transients with optoacoustic transducer," *Journal of Applied Physics,* vol. 87, pp. 2003-2014, Feb 15 2000.

[32] R. A. Kruger, K. M. Stantz, and J. W. L. Kiser, "Thermoacoustic CT of the breast," in *in Biomedical optoacoustic IV, Proc. SPIE*, San Jose, 2002, pp. 521-525.

[33] X. D. Wang, Y. J. Pang, G. Ku, G. Stoica, and L. H. V. Wang, "Three-dimensional laser-induced photoacoustic tomography of mouse brain with the skin and skull intact," *Optics Letters,* vol. 28, pp. 1739-1741, Oct 1 2003.

[34] K. W. Hollman, K. W. Rigby, and M. O'Donnell, "Coherent factor of speckle from a multi-row probe," in *in Proceedings of IEEE Conference on Ultrasonics* New York, 1999, pp. 1257-1260.

[35] M. L. Li, W. J. Guan, and P. C. Li, "Improved synthetic aperture focusing technique with applications in high-frequency ultrasound imaging," *Ieee Transactions on Ultrasonics Ferroelectrics and Frequency Control,* vol. 51, pp. 63-70, Jan 2004.

[36] P. E. Bize, A. Platon, C. D. Becker, and P. A. Poletti, "Perfusion measurement in acute pancreatitis using dynamic perfusion MDCT," *American Journal of Roentgenology,* vol. 186, pp. 114-118, Jan 2006.

[37] C. J. Hogan, M. L. Hess, K. R. Ward, and C. Gennings, "The utility of microvascular perfusion assessment in heart failure: A pilot study," *Journal of Cardiac Failure,* vol. 11, pp. 713-719, Dec 2005.

[38] T. Scholbach, E. Girelli, and J. Scholbach, "Tissue pulsatility index: A never parameter to evaluate renal transplant perfusion," *Transplantation,* vol. 81, pp. 751-755, Mar 15 2006.

[39] C. Weidekamm, M. Cejna, L. Kramer, M. Peck-Radosavljevic, and T. R. Bader, "Effects of TIPS on liver perfusion measured by dynamic CT," *American Journal of*

Roentgenology, vol. 184, pp. 505-510, Feb 2005.

[40] P. C. Li, S. W. Huang, C. W. Wei, Y. C. Chiou, C. D. Chen, and C. R. C. Wang, "Photoacoustic flow measurements by use of laser-induced shape transitions of gold nanorods," *Optics Letters,* vol. 30, pp. 3341-3343, Dec 15 2005.

[41] C. W. Wei, C. K. Liao, H. C. Tseng, Y. P. Lin, C. C. Chen, and P. C. Li, "Photoacoustic flow measurements with gold nanoparticles," *Ieee Transactions on Ultrasonics Ferroelectrics and Frequency Control,* vol. 53, pp. 1955-1959, Oct 2006.

[42] P. C. Li, S. W. Huang, C. W. Wei, and C. R. C. Wang, "Destruction-mode optoacoustic flow measurements with gold nanorods," in *in Proceedings of IEEE Conference on Ultrasonics* Rotterdam, 2005.

[43] P. C. Li, C. W. Wei, C. K. Liao, H. C. Tseng, Y. P. Lin, and C. C. Chen, "Time-intensity based optoacoustic flow measurements with gold nanoparticles," in *in BiOS, Proc. SPIE*, San Jose, 2005, pp. 63-72.

[44] C. G. A. Hoelen and F. F. M. de Mul, "Image reconstruction for photoacoustic scanning of tissue structures," *Applied Optics,* vol. 39, pp. 5872-5883, Nov 1 2000.

[45] C. G. A. Hoelen, F. F. M. de Mul, R. Pongers, and A. Dekker, "Three-dimensional photoacoustic imaging of blood vessels in tissue," *Optics Letters,* vol. 23, pp. 648-650, Apr 15 1998.

[46] C. K. Liao, M. L. Li, and P. C. Li, "Optoacoustic imaging with synthetic aperture focusing and coherence weighting," *Optics Letters,* vol. 29, pp. 2506-2508, Nov 1 2004.

[47] S. Boonsang, J. Zainal, and R. J. Dewhurst, "Synthetic aperture focusing techniques in time and frequency domains for photoacoustic imaging," *Insight,* vol. 46, pp. 196-199, Apr 2004.

[48] G. Manes, P. Tortoli, F. Andreuccetti, G. Avitabile, and C. Atzeni, "Synchronous Dynamic Focusing for Ultrasound Imaging," *Ieee Transactions on Ultrasonics Ferroelectrics and Frequency Control,* vol. 35, pp. 14-21, Jan 1988.

[49] "Significance of wavelength range for effective hair photo-epilation," in

Application Notes 3, 2004.

[50] S. Manohar, A. Kharine, J. C. G. van Hespan, W. Steenbergen, F. F. M. de Mul, and T. G. van Leeuwen, "Photoacoustic imaging of inhomogeneities embedded in breast tissue phantoms," in *in Biomedical optoacoustic IV, Proc. SPIE* San Jose, 2003, pp. 64-75.

[51] J. J. Niederhauser, M. Jaeger, and M. Frenz, "Comparison of laser-induced and classical ultrasound," in *in Biomedical optoacoustic IV, Proc. SPIE*, San Jose, 2003, pp. 118-123.

[52] D. Z. Feng, Y. Xu, G. Ku, and L. V. Wang, "Microwave-induced thermoacoustic tomography: Reconstruction by synthetic aperture," *Medical Physics,* vol. 28, pp. 2427-2431, Dec 2001.

[53] R. G. M. Kolkman, E. Hondebrink, W. Steenbergen, T. G. van Leeuwen, and F. F. M. de Mul, "Photoacoustic imaging of blood vessels with a double-ring sensor featuring a narrow angular aperture," *Journal of Biomedical Optics,* vol. 9, pp. 1327-1335, Nov-Dec 2004.

[54] M. H. Xu, Y. Xu, and L. H. V. Wang, "Time-domain reconstruction-algorithms and numerical simulations for thermoacoustic tomography in various geometries," *Ieee Transactions on Biomedical Engineering,* vol. 50, pp. 1086-1099, Sep 2003.

[55] Y. Xu, D. Z. Feng, and L. H. V. Wang, "Exact frequency-domain reconstruction for thermoacoustic tomography - I: Planar geometry," *Ieee Transactions on Medical Imaging,* vol. 21, pp. 823-828, Jul 2002.

[56] K. P. Kostli, M. Frenz, H. P. Weber, G. Paltauf, and H. Schmidt-Kloiber, "Optoacoustic tomography: time-gated measurement of pressure distributions and image reconstruction," *Applied Optics,* vol. 40, pp. 3800-3809, Aug 1 2001.

[57] G. Paltauf and H. Schmidt-Kloiber, "Pulsed optoacoustic characterization of layered media," *Journal of Applied Physics,* vol. 88, pp. 1624-1631, Aug 1 2000.

[58] S. R. Arridge, H. Dehghani, M. Schweiger, and E. Okada, "The finite element model for the propagation of light in scattering media: A direct method for domains with nonscattering regions," *Medical Physics,* vol. 27, pp. 252-264, Jan 2000.

[59] M. Schweiger and S. R. Arridge, "The finite-element method for the propagation of light in scattering media: Frequency domain case," *Medical Physics,* vol. 24, pp. 895-902, Jun 1997.

[60] M. Schweiger, S. R. Arridge, M. Hiraoka, and D. T. Delpy, "The Finite-Element Method for the Propagation of Light in Scattering Media - Boundary and Source Conditions," *Medical Physics,* vol. 22, pp. 1779-1792, Nov 1995.

[61] K. W. Hollman, S. Y. Emelianov, G. J. Spooner, R. T. Juhasz, and M. O'Donnell, "Mapping high frequency ultrasonic fields with femtosecond laser generated cavitation," in *in Proceedings of IEEE Conference on Ultrasonics* Atlanta, 2001, pp. 1461-1464.

[62] C. K. Liao and P. C. Li, "Reconstruction of optical energy deposition for backward optoacoustic imaging," *Optical and Quantum Electronics,* vol. 37, pp. 1339-1351, Dec 2005.

[63] B. T. Cox, S. R. Arridge, K. P. Kostli, and P. C. Beard, "Quantitative photoacoustic imaging: fitting a model of light transport to the initial pressure distribution," in *in BiOS, Proc. SPIE*, San Jose, 2005, pp. 49-55.

[64] B. T. Cox, S. R. Arridge, K. P. Kostli, and P. C. Beard, "Two-dimensional quantitative photoacoustic image reconstruction of absorption distributions in scattering media by use of a simple iterative method," *Applied Optics,* vol. 45, pp. 1866-1875, Mar 10 2006.

[65] J. A. Viator, S. L. Jacques, and S. A. Prahl, "Depth profiling of absorbing soft materials using photoacoustic methods," *Ieee Journal of Selected Topics in Quantum Electronics,* vol. 5, pp. 989-996, Jul-Aug 1999.

[66] G. Paltauf and P. E. Dyer, "Photomechanical processes and effects in ablation," *Chemical Reviews,* vol. 103, pp. 487-518, Feb 2003.

[67] Force, "High Frequency PVDF Needle-Type Miniature Ultrasonic Hydrophones." vol. 2007 Brøndby, Denmark, 2007.

[68] T. Aikawa, J. Gunn, S. M. Spong, S. J. Klaus, and M. Korc, "Connective tissue growth factor-specific antibody attenuates tumor growth, metastasis, and angiogenesis

in an orthotopic mouse model of pancreatic cancer," *Molecular Cancer Therapeutics,* vol. 5, pp. 1108-1116, May 2006.

[69] P. Schulz, A. Scholz, A. Rexin, P. Hauff, M. Schirner, B. Wiedenmann, K. Detjen, and S. Rosewicz, "Reconstitution of p16INK4a in an orthotopic pancreatic mouse model inhibits tumor growth and angiogenesis," *Gastroenterology,* vol. 130, pp. A35-A35, Apr 2006.

[70] N. S. Akella, D. B. Twieg, T. Mikkelsen, F. H. Hochberg, S. Grossman, G. A. Cloud, and L. B. Nabors, "Assessment of brain tumor angiogenesis inhibitors using perfusion magnetic resonance imaging: Quality and analysis results of a phase I trial," *Journal of Magnetic Resonance Imaging,* vol. 20, pp. 913-922, Dec 2004.

[71] M. Dadiani, E. Furman-Haran, and H. Degani, "The application of NMR in tumor angiogenesis research," *Progress in Nuclear Magnetic Resonance Spectroscopy,* vol. 49, pp. 27-44, Aug 15 2006.

[72] T. Holscher, T. Postert, S. Meves, T. Thies, H. Ermert, U. Bogdahn, and W. Wilkening, "Assessment of brain perfusion with echo contrast specific imaging modes and Optison (TM)," *Academic Radiology,* vol. 9, pp. S386-S388, Aug 2002.

[73] T. Holscher, W. Wilkening, B. Draganski, S. H. Meves, J. Eyding, H. Voit, U. Bogdahn, H. Przuntek, and T. Postert, "Transcranial ultrasound brain perfusion assessment with a contrast agent-specific imaging mode - Results of a two-center trial," *Stroke,* vol. 36, pp. 2283-2285, Oct 2005.

[74] C. Pohl, K. Tiemann, T. Schlosser, and H. Becher, "Stimulated acoustic emission detected by transcranial color Doppler ultrasound - A contrast-specific phenomenon useful for the detection of cerebral tissue perfusion," *Stroke,* vol. 31, pp. 1661-1666, Jul 2000.

[75] G. J. Hunter, H. M. Silvennoinen, L. M. Hamberg, W. J. Koroshetz, F. S. Buonanno, L. H. Schwamm, G. A. Rordorf, and R. G. Gonzalez, "Whole-brain CT perfusion measurement of perfused cerebral blood volume in acute ischemic stroke: Probability curve for regional infarction," *Radiology,* vol. 227, pp. 725-730, Jun 2003.

[76] L. Bentzen, M. R. Horsman, P. Daugaard, and R. J. Maxwell, "Non-invasive tumour blood perfusion measurement by H-2 magnetic resonance," *Nmr in*

Biomedicine, vol. 13, pp. 429-437, Dec 2000.

[77] E. Johansson, L. E. Olsson, S. Mansson, J. S. Petersson, K. Golman, F. Stahlberg, and R. Wirestam, "Perfusion assessment with bolus differentiation: A technique applicable to hyperpolarized tracers," *Magnetic Resonance in Medicine,* vol. 52, pp. 1043-1051, Nov 2004.

[78] K. Wei, A. R. Jayaweera, S. Firoozan, A. Linka, D. M. Skyba, and S. Kaul, "Quantification of myocardial blood flow with ultrasound-induced destruction of microbubbles administered as a constant venous infusion," *Circulation,* vol. 97, pp. 473-483, Feb 10 1998.

[79] X. C. Chen, K. Q. Schwarz, D. Phillips, S. D. Steinmetz, and R. Schlief, "A mathematical model for the assessment of hemodynamic parameters using quantitative contrast echocardiography," *Ieee Transactions on Biomedical Engineering,* vol. 45, pp. 754-765, Jun 1998.

[80] L. Claassen, G. Seidel, and C. Algermissen, "Quantification of flow rates using harmonic grey-scale imaging and an ultrasound contrast agent: an in vitro and in vivo study," *Ultrasound in Medicine and Biology,* vol. 27, pp. 83-88, Jan 2001.

[81] N. L. Eigler, J. M. Pfaff, A. Zeiher, J. S. Whiting, and J. S. Forrester, "Digital Angiographic Impulse-Response Analysis of Regional Myocardial Perfusion - Linearity, Reproducibility, Accuracy, and Comparison with Conventional Indicator Dilution Curve Parameters in Phantom and Canine Models," *Circulation Research,* vol. 64, pp. 853-866, May 1989.

[82] C. K. Yeh, S. W. Wang, and P. C. Li, "Feasibility study of time-intensity-based blood flow measurements using deconvolution," *Ultrasonic Imaging,* vol. 23, pp. 90-105, Apr 2001.

[83] C. K. Yeh, K. W. Ferrara, and D. E. Kruse, "High-resolution functional vascular assessment with ultrasound," *Ieee Transactions on Medical Imaging,* vol. 23, pp. 1263-1275, Oct 2004.

[84] K. Wei, D. M. Skyba, C. Firschke, A. R. Jayaweera, J. R. Lindner, and S. Kaul, "Interactions between microbubbles and ultrasound: In vitro and in vivo observations," *Journal of the American College of Cardiology,* vol. 29, pp. 1081-1088,

Apr 1997.

[85] Y. Y. Yu, S. S. Chang, C. L. Lee, and C. R. C. Wang, "Gold nanorods: Electrochemical synthesis and optical properties," *Journal of Physical Chemistry B,* vol. 101, pp. 6661-6664, Aug 21 1997.

[86] S. S. Chang, C. W. Shih, C. D. Chen, W. C. Lai, and C. R. C. Wang, "The shape transition of gold nanorods," *Langmuir,* vol. 15, pp. 701-709, Feb 2 1999.

[87] C. W. Sheppard, *Basic principles of the tracer method*. New York: Wiley, 1962.

[88] T. R. Harris and E. V. Newman, "An Analysis of Mathematical Models of Circulatory Indicator-Dilution Curves," *Journal of Applied Physiology,* vol. 28, pp. 840, 1970.

[89] MatTek, "The EpiDermFT™ Skin Model." vol. 2007 Ashland, MA, 2007.

Publication list

Journal papers:

1. **Chao-Kang Liao,** Meng-Lin Li, and Pai-Chi Li, “Optoacoustic imaging with synthetic aperture focusing and coherence weighting, ” Optics Letters, Vol. 29 pp.2506-2508 2004.

2. **Chao-Kang Liao,** Sheng-Wen Huang, Chen-Wei Wei, and Pai-Chi Li, ”Nanorod-based perfusion estimation using a high-frame-rate photoacoustic imaging system,” Journal of biomedical optics 2007 (accepted).

3. **Chao-Kang Liao** and Pai-Chi Li, ”Reconstruction of optical energy deposition for backward optoacoustic imaging,” Optical and quantum electronics, Vol. 39 pp.1339-1351 2005.

4. Deng-Huei Huang, **Chao-Kang Liao**, Chen-Wei Wei, and Pai-Chi Li, “Simulations of optoacoustic wave propagation in light-absorbing media using a finite-difference time-domain method”, Journal of the acoustical society of america, Vol. 117, pp.2795-2801, 2005

5. Chen-Wei Wei, **Chao-Kang Liao,** Hsiao-Chien Tseng, Yen-Ping Lin, Chia-Chun Chen, Pai-Chi Li, “Photoacoustic flow measurements with gold nanoparticles,” IEEE Transactions on ultrasonics ferroelectrics and frequency control, Vol. 53 pp.1955-1959 2006.

6. Pai-Chi Li, Chen-Wei Wei, **Chao-Kang Liao**, Cheng-Dah Chen, Kuei-Chen Pao, Churng-Ren Chris Wang, Ya-Na Wu, and Dar-Bin Shieh, “Photoacoustic imaging of multiple targets using gold nanorods”, IEEE Transactions on Ultrasonics, Ferroelectrics and Frequency Control (accepted).

Conference papers:

1. **Chao-Kang Liao** and Pai-Chi Li, “Quantitative reconstruction of optical absorption coefficient in backward mode photoacoustic imaging,” Oral presentation 2007 SPIE International Symposium on Biomedical Optics (BiOS) **6437**, San Jose, California, USA, January, 2007.

2. **Chao-Kang Liao**, Sheng-Wen Huang, Chen-Wei Wei, and Pai-Chi Li, "A high frame rate photoacoustic imaging system and its applications to perfusion measurements," Oral presentation, 2006 SPIE International Symposium on Biomedical Optics (BiOS) **6086**, San Jose, California, USA, January, 2006.

3. **Chao-Kang Liao** and Pai-Chi Li, "Optoacoustic imaging with improved synthetic focusing," Oral presentation, 2005 SPIE International Symposium on Biomedical Optics (BiOS) **5697**, San Jose, California, USA, January, 2005.

4. **Chao-Kang Liao,** Chen-Wei Wei, and Pai-Chi Li, "Gold nanorods based perfusion measurement: A phantom study using a high frame rate photoacoustic imaging system," *Symposium of Annual Conference of the Biomedical Engineering Society*, Taipei, Taiwan, R.O.C., Dec. 2006.

5. **Chao-Kang Liao** and Pai-Chi Li, "Reconstruction of optical absorption distribution for backward optoacoustic imaging," *Symposium of Annual Conference of the Biomedical Engineering Society*, Taoyuan, Taiwan, R.O.C., Dec. 2005

6. **Chao-Kang Liao** and Pai-Chi Li, "Reconstruction of optical absorption distribution for backward optoacoustic imaging," *Symposium of Annual Conference of the Biomedical Engineering Society*, Tainan, Taiwan, R.O.C., Dec. 2004

7. **Chao-Kang Liao,** Chen-Wei Wei, Deng-Huei Huang, Meng-Lin Li, and Pai-Chi Li, "Improved backward opto-acoustic imaging using synthetic aperture focusing technique," *Symposium of Annual Conference of the Biomedical Engineering Society*, Taipei, Taiwan, R.O.C., December 12-13, 2003.

8. Deng-Huei Huang, **Chao-Kang Liao,** Chen-Wei Wei, and Pai-Chi Li, "Simulation of optoacoustic wave propagation in light absorbing media," Symposium of Annual Conference of the Biomedical Engineering Society, Taipei, Taiwan, R.O.C., December 12-13, 2003.

9. Chen-Wei Wei, **Chao-Kang Liao**, Cheng-Dah Chen, Kuei-Chen Pao, Churng-Ren Chris Wang, Ya-Na Wu, Dar-Bin Shieh, and P.-C. Li, "Photoacoustic Molecular Imaging Using Bioconjugated Gold Nanorods with Multiple Targeting," *Symposium of Annual Conference of the Biomedical*

Engineering Society, Taipei, Taiwan, R.O.C., Dec. 2006

10. Chen-Wei Wei, **Chao-Kang Liao**, and Pai-Chi Li, "Gold Nanorods Based Perfusion Measurement: A Phantom Study Using A High Frame Rate Photoacoustic Imaging System**,"** *Symposium of Annual Conference of the Biomedical Engineering Society*, Taipei, Taiwan, R.O.C, Dec. 2006.

11. Pai-Chi Li, Chen-Wei Wei, **Chao-Kang Liao**, Cheng-Dah Chen, Kuei-Chen Pao, Churng-Ren Chris Wang, Ya-Na Wu, and Dar-Bin Shieh, "Multiple targeting in photoacoustic imaging using bioconjugated gold nanorods," Oral presentation 2006 SPIE International Symposium on Biomedical Optics (BiOS) **6086**, San Jose, California, USA, January, 2006.

12. Pai-Chi Li, Chen-Wei Wei, and **Chao-Kang Liao,** "Time-intensity based optoacoustic flow measurements with gold nanoparticles, "Oral presentation, 2005 SPIE International Symposium on Biomedical Optics (BiOS) **5697**, San Jose, California, USA, January, 2005.